Comparison of the top-down and bottom-up approach to fabricate axial nanowire-based Silicon/Germanium heterostructures

Dissertation

zur Erlangung des akademischen Grades
doctor rerum naturalium (Dr. rer. nat.)

vorgelegt der

Naturwissenschaftlichen Fakultät II
(Bereich Physik)
der Martin-Luther-Universität Halle-Wittenberg

von Herrn Andreas Wolfsteller
geboren am 24. August 1981 in Dessau

Eingereicht am: Halle (Saale), 22. Oktober 2009
Verteidigt am: Halle (Saale), 08. März 2010

GutachterInnen:

1. PD Dr. Hartmut S. Leipner, Martin-Luther-Universität Halle-Wittenberg
2. Prof. Dr. Anna Fontcuberta i Morral, École Polytechnique de Fédérale de Lausanne
3. Prof. Dr. Margit Zacharias, Albert-Ludwigs-Universität Freiburg

Table of Contents

Abstract

Axial nanowire-based Silicon/Germanium (Si/Ge) heterostructures are interesting research objects because of the possibility to fabricate and investigate quantum well and quantum dot (QD) structures. Furthermore, they are expected to be building blocks for future devices, e. g. field-effect transistors (FETs), sensors and optoelectronic devices. They have also become interesting as the basic components of thermoelectric elements which are intended to operate at lower temperatures than conventional bulk Si/Ge materials. However, there are still a lot of tasks that have to be accomplished. This includes the exact control of the nanowire (NW) positions for future contacting as well as the positioning of the Ge layers, and also the challenge to produce sharp Si/Ge interfaces and high element concentrations within the Si and Ge part of the NWs.

A variety of different approaches has been developed to fabricate Si NWs and Si/Ge NW heterostructures. They can be divided into two basic categories: 'bottom-up' approaches and 'top-down' approaches. The most common example of the former one is the vapour-liquid-solid (VLS) mechanism, which allows the growth of NWs via a liquid catalyst droplet attached to the surface of the Si substrate. Prominent examples of top-down approaches are combinations of conventional layer growth with etching techniques like, for instance, metal-assisted wet chemical etching or reactive ion etching (RIE).

This work compares bottom-up and top-down approaches concerning the structural properties of the fabricated NWs, focussing firstly on the control of the NW position, dimensions, orientation and morphology, secondly on the positioning of the Ge layers, the achievable Ge concentrations and the abruptness of the Si/Ge interfaces, and thirdly on crystal defects, i. e. inclusions of catalyst atoms and misfit dislocations, which might be generated during the fabrication process. Because it offers a precise growth control under highly reproducible conditions, molecular beam epitaxy (MBE) has been chosen as a representative deposition technique for both the bottom-up NW growth and the fabrication of the Si/Ge heterostructures as part of the top-down approach. In the latter case, the NWs were produced by electron beam lithography (EBL) and RIE.

Based on the results of this investigation, the selected approaches will in the end also be compared concerning their scientific potential, e. g. for the investigation of quantum confinement effects, and their application potential as building blocks for devices.

1 Introduction and Survey

1.1 Silicon Nanowires and Axial Silicon/Germanium Nanowire Heterostructures

Silicon (Si) nanowires (NWs) as they are treated in this thesis are free-standing single crystalline structures with a diameter $\boldsymbol{d}$ between only several nanometers and a maximum of a few hundred nanometers (but typically below 200 nm), and a length $\boldsymbol{l}$ of again a few hundred nanometers up to several micrometers. Their length is usually larger than the diameter ($\boldsymbol{l} > \boldsymbol{d}$) (Scheme 1a). However, the aim in both industry and science is to reduce the diameter of the NWs further and further, thus increasing the *aspect ratio* $\boldsymbol{l} \cdot \boldsymbol{d}^{-1}$ of the NWs. The intended cross sectional area is often circular and is therefore also regarded as circular for all following theoretical calculations and assumptions. If the NWs have a preferred orientation, e. g. perpendicular to the substrate surface, and to distinguish them from in-plane NWs, they are often also referred to as nanowhiskers.

The simplest axial silicon/germanium (Si/Ge) NW heterostructure one can imagine is a germanium (Ge) NW part with thickness $\boldsymbol{h}$ connected to a Si NW (Scheme 1b). Both parts have approximately the same diameter. There is only one interface. However, it might also be necessary to incorporate several Ge-rich $Si_{1-X}Ge_X$ layers with a nominal thickness $\boldsymbol{h}$ and a certain Ge content $\boldsymbol{X}$ ($0 \leq \boldsymbol{X} \leq 1$) into the Si NW (Scheme 1c). The number of interfaces then increases to $2 \cdot \boldsymbol{n}$ with $\boldsymbol{n}$ being the number of Ge layers.

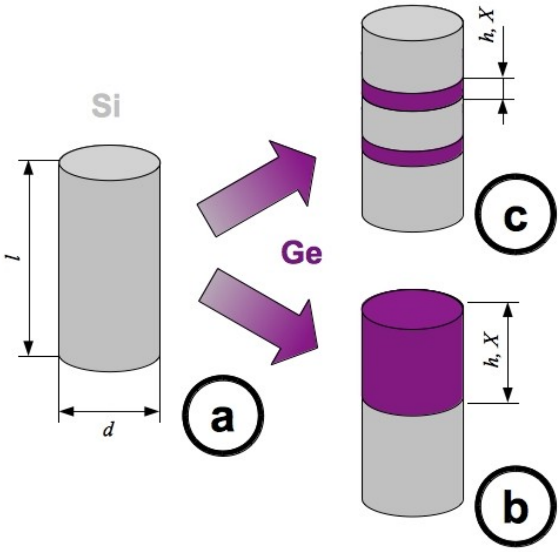

Scheme 1: From silicon nanowires to axial nanowire-based silicon/germanium heterostructures.

1.2 Research Interests and Potential Applications

Quantum Confinement Effects

In bulk semiconductor crystals, the influence of the crystal surface and any surface states can often be neglected. Furthermore, the electrons are spatially *unconfined* and conduction bands are treated as continuous. For nanostructures, however, the surface area to volume ratio $\boldsymbol{A \cdot V^{-1}}$ becomes significant. The influence of the surface has to be taken into account for calculations as well as for measurements. In addition, quantum confinement effects might change the electrical and optical properties of materials compared to their respective bulk values. If the dimensions of nanostructures are below the *Exciton Bohr Radius* $\boldsymbol{a_B}$, the energy bands become *discrete*. The radius $\boldsymbol{a_B}$ is the distance between the two components of an exciton state: an electron in the conduction band which is still bound by the *Coulomb force* to the hole it leaves behind in the valence band (*Wannier exciton*). The bulk values of the Exciton Bohr Radius in Si and Ge [1] are shown in Table 1.

There are several types of *quantum structures*: A *quantum well* confines the electron in only one dimension. In a *quantum wire*, the electron is already confined in two dimensions. Finally, a *quantum dot* (QD) creates a confinement in all three spatial dimensions. The Exciton Bohr Radius usually varies between 2 and 10 nm, depending on the semiconductor material. It is defined as

$$a_B = \frac{4 \cdot \pi \cdot \epsilon \cdot \epsilon_0 \cdot \hbar^2}{m_r \cdot e^2} , \tag{1}$$

where $\boldsymbol{\varepsilon}$ is the dielectric constant of the crystal, $\boldsymbol{\varepsilon_0}$ the electric constant, $\boldsymbol{\hbar}$ the reduced Planck constant and $\boldsymbol{e}$ the elementary charge. In (1) $\boldsymbol{m_r}$ is the reduced mass of the electron-hole pair which can be obtained by

$$\frac{1}{m_r} = \frac{1}{m_e^{eff}} + \frac{1}{m_h^{eff}} , \tag{2}$$

where m_e^{eff} is the effective mass of the electron and m_h^{eff} the effective mass of the corresponding hole in the valence band.

Element	***Name***	***Exciton Bohr Radius***	***Atomic Number***	***Atomic Mass***	***Electron Mobility****	***Energy Gap****
Si	Silicon	4.9 nm	14	28,0855 u	1450 cm^2 / Vs	ΔE = 1.1 eV
Ge	Germanium	24.3 nm	32	72,61 u	3900 cm^2 / Vs	ΔE = 0.67 eV

*Table 1: Selected properties of Si and Ge, part I. * at* $\boldsymbol{T} \approx 300$ *K.*

For a Si quantum wire the NW radius has to be smaller than $\boldsymbol{a_B}$. However, the diameters of present Si NWs are mostly still above 20 nm. Due to the rather large Exciton Bohr Radius of Ge the integration of thin Ge layers into Si NWs offers an alternative option to create quantum well or QD structures. The latter is possible if the radius of the host Si NW is below about 17 nm (Scheme 2b). However, $\boldsymbol{a_B}$ decreases with increasing Si concentration in the Ge part of the NW.

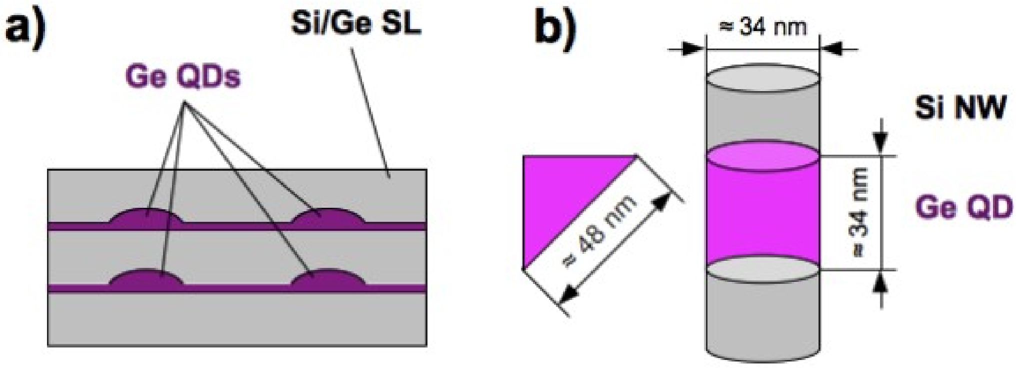

Scheme 2: a) Formation of Ge quantum dots by strain-induced island formation during the growth of a Si/Ge superlattice. b) Germanium quantum dots (X = 1) can also be obtained by Si/Ge nanowire growth if the radius of the host silicon nanowire is below about 17 nm.

Optoelectronic Devices

Quantum confinement effects have also been the reason for a growing interest in the optical properties of Si NWs and Si/Ge heterostructure NWs during the past years. While bulk Si has an indirect band gap of ≈ 1.1 eV (Table 1), Si NWs can possess direct energy gaps [2-6]. Furthermore, strong luminescent properties in the visible light range were reported [7]. Again, due to the difference in $\boldsymbol{a_B}$, it is easier to produce Ge quantum structures. By embedding optically active Ge QDs into a Si matrix, light emission at room temperature was achieved by Zakharov *et al.* [8]. The stacks of QDs were created by a self-assembling process based on the well known island formation of Ge on a Si substrate, which occurs due to the strain induced into the growing Si/Ge superlattice by the lattice mismatch (Scheme 2a).

Changing the QD host from a Si/Ge superlattice to a regular array of Si NWs would allow a better growth control, e. g. the exact positioning of the individual QD stacks on the wafer. By contacting the NWs individually, each NW could act as a single optoelectronic device.

Device Engineering

The possibility to fabricate quantum structures is only one of many reasons for the growing interest in the fabrication of Si/Ge heterostructure NWs. They are also considered as building blocks for many other future devices, like sensors and field-effect transistors (FETs) [9-14]. In the latter case, NWs offer an approach to reduce the gate length in transistor-based microelectronics even further. For example, in the current state-of-the-art "45 nanometer technology" for industrial fabrication processes of top-gate FETs, the gate length is still 35 nm. In contrast, by using vertical surround-gate Si NW FETs with 20 nm diameter, the gate length can be reduced to approx. 9 nm. Due to their higher electron mobility compared to Si NWs [15-17], Ge NWs are especially considered for such NW FET devices.

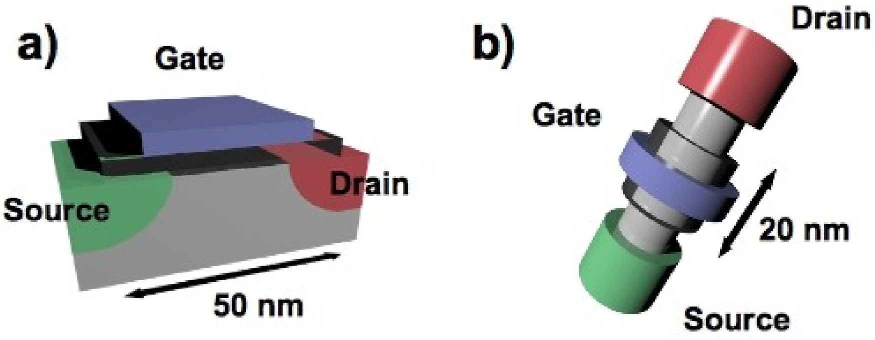

Scheme 3: Comparison of a conventional planar FET (a) and a nanowire-based vertical surround-gate FET (b)

The growth of Ge NWs on a Si NW buffer structure would allow the implementation of Ge NWs into conventional Si nano/microelectronics. Because the NW can expand also in the radial direction, at least to a certain degree, the growth of Ge NWs with high Ge concentrations and a sharp interface is possible if the NW radius is below the critical radius for dislocation formation [18], as discussed later in more detail. Furthermore, the Si/Ge heterostructure could work as a buffer structure itself for the implementation of InGaAs or GaAs nanostructures on Si substrates.

Another special feature of the Ge-Si system, which adds to the high industrial potential, is the unlimited miscibility of its components. This allows the tuning of the band gap of a device between 0.67 eV for pure Ge to 1.1 eV for pure Si.

Thermoelectric Devices

Axial Si/Ge heterostructures (Si NWs containing several Ge layers) are also considered as components of thermoelectric devices [14,19-23]. Based on the *Seebeck effect*, such devices directly convert an applied temperature difference $\Delta T = T_2 - T_1$ ($T_2 > T_1$) into a voltage, thus generating a current in a closed circuit. The thermoelectric figure of merit Z is often used to compare the conversion efficiency of devices made of different materials. By multiplying Z with the average temperature $T = 0.5 \cdot (T_1 + T_2)$ the dimensionless figure of merit ZT is obtained. It is defined as

$$ZT = \frac{\kappa_{El}}{\kappa_{Th}} \cdot S^2 \cdot T\,, \tag{3}$$

where κ_{El} is the electrical conductivity, S is the *Seebeck coefficient* and κ_{Th} the thermal conductivity. Both electrons and phonons contribute to the thermal conductivity. However, to increase ZT, a reduction of the thermal conduction by electrons is not desirable, because at the same time the electrical conduction would also decrease, negating the effort. Therefore, the focus lies on the reduction of the thermal conduction contribution by phonons.

Conventional two-dimensional Si/Ge superlattice heterostructures already show promising thermoelectric properties due to phonon scattering at the interfaces [24-28]. Phonon scattering at NW surfaces can reduce the thermal conductivity of Si NWs compared to bulk values by more than two orders of magnitude for NWs with diameters of 22-115 nm [29]. By combining both kinds of structures into axial nanowire-based Si/Ge superlattice heterostructures, it is expected that ZT can be improved even further [19].

Open Questions

First Si/Ge NW prototype devices have already been build for measurements and demonstrations [20,30-33]. In most of these cases the NWs were cut from their growth substrate, suspended in a solution, transferred to another substrate, where, finally, contacts were produced by lithographic methods. Although the results were useful for purposes of technology demonstration, this 'pick-and-place approach' can not be transferred to industrial large-scale manufacturing. Thus the exact control of the NW position for future individual contacting directly on the growth substrate itself is one of several tasks that must be accomplished to allow for a successful implementation of NW structures in nano/microelectronic devices. Other tasks include the positioning of the Ge layers and the challenge to produce sharp Si/Ge interfaces and high element concentrations within the Si and Ge parts of the NWs to finally observe the desired quantum confinement effects.

1.3 Fabrication Methods

The methods to fabricate Si NWs and/or Si/Ge heterostructure NWs can be divided into two basic categories: 'bottom-up' approaches and 'top-down' approaches. The former ones are often based on the vapour-liquid-solid (VLS) mechanism, which allows the growth of NWs via a catalyst, e. g. a gold (Au) droplet attached to the surface of the Si substrate. The top-down approaches are frequently based on etching techniques, e. g. metal-assisted wet chemical etching or reactive ion etching (RIE).

Bottom-Up Approaches

The growth of Si NWs was already reported in 1964 by Wagner and Ellis [34-36], who also proposed the vapour-liquid-solid (VLS) mechanism. Detailed examinations were carried out in 1975 by Givargizov [37,38]. With the development of modern electron microscopes, the NWs became even more interesting research objects, with their diameter constantly decreasing.

In the VLS model, the Si NW grows from a metal-silicon eutectic alloy droplet on a Si surface. Often, a precursor gas, e. g. SiH_4 or $SiCl_4$, is used as the Si source. This deposition technique is referred to as chemical vapour deposition (CVD). For the growth of NWs, the precursor gas is cracked at the surface of the catalyst droplet, with the Si atoms transferred into the droplet (vapour-liquid transition). Finally, a supersaturation of silicon occurs in the droplet, and the Si precipitates at the droplet/wafer interface (liquid-solid transition), thus forming the NW. This process continues until the gas flow is eventually interrupted.

The VLS mechanism was also successfully transferred to the growth of Ge NWs [39-46]. Although Au is by far the most prominent metal catalyst [39-42], Ge NW growth has been reported using Ni [44,45] or Cu [43] as the catalyst, while Si NWs were also grown by Al [47], Cu [36,48-50], Pd [50], Pt [36,51], Ni [50], Ag [36,50] or even Ti [52,53]. Kodambaka *et al.* [46] and Kang *et al.* [43] have also shown that Ge NWs can be synthesised by a solid catalyst particle, albeit at a slower growth rate. This mechanism is called the vapour-solid-solid (VSS) mechanism. The large-scale industrial application of Ge NW growth by CVD, however, is limited by the high toxicity of the preferred precursor gas, germane (GeH_4).

The fabrication of Si NWs by physical vapour deposition (PVD) methods was also reported, including laser ablation (PLD) [54] and molecular beam epitaxy (MBE) [55-60]. These methods use a particle beam produced by sputtering or thermal evaporation for crystal growth instead of precursor gases. The Au-Si eutectic droplets also act as seeds for the NW growth, however, they do not act as catalysts to crack precursor molecules, since the material is already provided in the form of single atoms.

Instead, a gradient in the chemical potential leads to a net flux of Si monomers towards the droplet interface. The total flux $\boldsymbol{I}$ of Si atoms can be written as $\boldsymbol{I} = \boldsymbol{I_1} + \boldsymbol{I_2}$. $\boldsymbol{I_1}$ represents the monomers absorbed by the droplet through direct impingement, $\boldsymbol{I_2}$ represents the net flux which is generated by the surface diffusion as mentioned before. Thus the difference in the length of the NWs compared to the overgrown epilayer $\Delta \boldsymbol{l} = \boldsymbol{l_{NW}} - \boldsymbol{l_{epi}}$ is fully determined by the net flux $\boldsymbol{I_2}$ (Scheme 4).

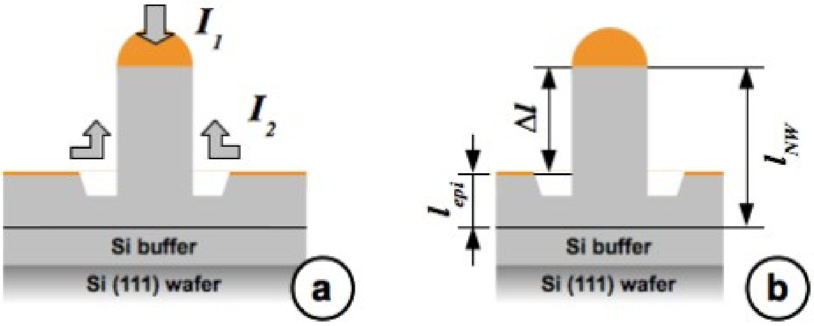

Scheme 4: a) Surface diffusion and direct impingement add to the total flux of atoms contributing to the nanowire growth. b) The visible length $\Delta \boldsymbol{l}$ *is directly determined by the flux* $\boldsymbol{I_2}$.

The fabrication of axial $Si/Si_{1-X}Ge_X$ heterostructure NWs has also been demonstrated for CVD [61-64], MBE [58,59] and a combination of Si NW growth by CVD and Ge ablation by PLD [64]. However, the Ge concentrations were low, and non-abrupt interfaces were observed, with a width, for instance, in the order of 40 nm for 200 nm diameter NWs. The diameter dependence of the interfacial abruptness was studied in detail by Clark *et al.* for VLS CVD grown NWs [63].

Top-Down Approaches

These approaches to fabricate Si/Ge NW heterostructures usually consist of three individual steps. First, the Si/Ge heterostructure is grown by conventional deposition techniques like CVD or MBE. Second, a mask is placed on top of the sample, and, finally, the NWs are etched into the substrate by wet chemical etching or dry etching processes.

Recently, several groups fabricated large-area Si NW arrays by metal-assisted wet chemical etching [65-72], using either self-alignment mechanisms [65] or mask fabrication by colloidal lithography [66-72]. In the latter case, polymer spheres are placed on the substrate utilising a natural self-assembling process to form a close-packed hexagonally arranged monolayer. By plasma etching, the diameter of the spheres can be reduced down to a minimum of 50 nm.

Afterwards, a metal thin film (like Ag, Au or Pt) is deposited onto the modified polymer sphere mask. The etching process itself is based on a local oxidation and dissolution of the Si in a HF/H_2O_2 solution with the metal acting as a catalyst [70-72]. A high area density of about 10^{10} NWs/cm^2 can be obtained. The SEM micrographs in Figure 1 show Si NWs with a diameter of 1.8 µm (panel 1) and 480 nm (panel 2) which were fabricated over large (wafer-size) areas [73].

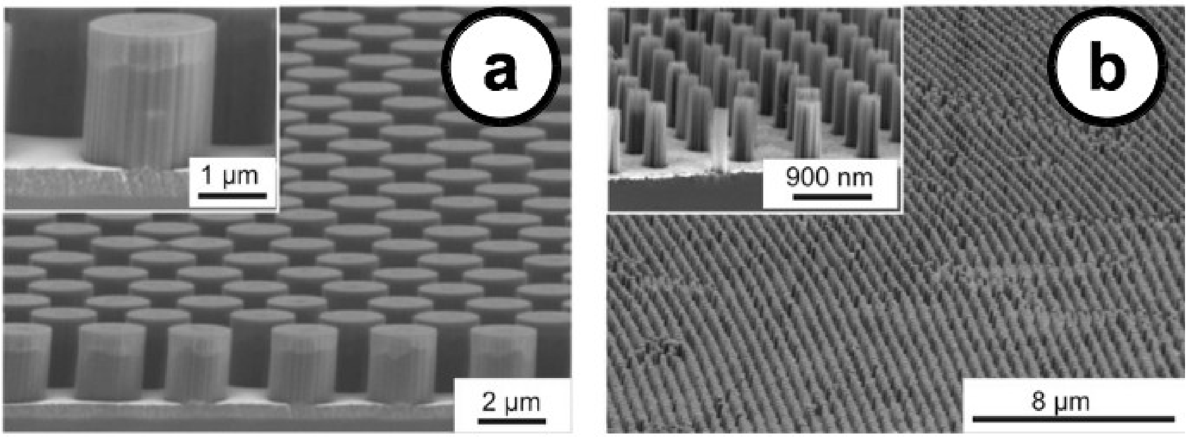

Figure 1: Cross-section SEM micrographs of Si nanowires fabricated by metal-assisted wet chemical etching. Extended arrays of well-ordered, vertically aligned Si nanowires with controllable diameters can be generated. Si nanowires with diameters of 1.8 µm (a) and 480 nm (b). [73]

Combining metal-assisted wet chemical etching with colloidal lithography and plasma etching is an inexpensive and fast approach to fabricate large arrays of NWs with homogenous lengths and diameters. It was successfully adopted for the etching of Si/Ge structures [74], but the Ge concentration was below 25 at.-%. Furthermore, since the minimum diameter is limited to 50 nm, this method is also not applicable for the investigation of quantum size effects.

The combination of deposition techniques with mask fabrication by electron beam lithography and a reactive ion etching process is another possible top-down approach for the fabrication of Si/Ge NW heterostructures. Here, the arrangement of the NWs is not limited to a hexagonal lattice. Instead, the NWs can theoretically be placed individually. Furthermore, no metal is involved in any step, which excludes the contamination of the NWs already from the beginning. However, the fabrication of Si/Ge NW heterostructures by MBE/EBL/RIE has up to now not been reported in literature.

1.4 Research Subject

Motivated by the outstanding tasks mentioned above, this work compares bottom-up and top-down approaches concerning the structural properties of the fabricated NW heterostructures. Because it offers a precise growth control under highly reproducible conditions, MBE was chosen as a representative deposition technique for both the bottom-up NW growth and the fabrication of the Si/Ge heterostructures as part of the top-down approach. In the latter case, Si/Ge superlattice structures were deposited by MBE, followed by an EBL and RIE step to produce the NW structures. In case of the bottom-up approach, both the integration of thin Ge layers into Si NWs and the continuous growth of Ge on Si NWs was studied.

The focus of the investigation was firstly on the control of the NW position and dimensions, as well as the orientation and morphology, secondly on the positioning of the Ge layers, the achievable Ge concentrations and the abruptness of the Si/Ge interfaces, and thirdly on crystal defects that might occur during the fabrication of the nanostructures, i. e. the inclusion of metal atoms as point defects and the generation of misfit dislocations. Furthermore, the comparison of an approach based on conventional crystal growth (layer growth) with another one based on one-dimensional crystal growth (NW growth) allows the investigation of heteroepitaxial growth under different circumstances. Between the two approaches, there should be remarkable differences concerning strain accumulation, strain relaxation and the formation of misfit dislocations.

All of the resulting nanostructures were investigated by transmission electron microscopy (TEM), high-resolution scanning electron microscopy (SEM) and energy dispersive X-ray diffraction (EDX). While SEM was used to analyse the morphology of the NWs and to determine their cross-sectional shape, diameter and the NW density, the inner structure was investigated by TEM. The elemental composition was confirmed by EDX and the Ge concentration was measured by TEM bright field imaging.

2 Crystal Growth and Crystal Defects

2.1 Crystal Growth by Molecular Beam Epitaxy

Molecular beam epitaxy (MBE) is a PVD method for epitaxial growth of single crystalline materials on a substrate. It was invented by J. R. Arthur and Alfred Y. Cho at Bell Telephone Laboratories in the late 1960s [75,76]. Today, it is widely used for thin film deposition in semiconductor technology. As mentioned above, in PVD methods the growth material is not supplied as a precursor gas but a solid target. This target is heated until material at its surface sublimates. The vaporized material then condenses on the substrate. Since the deposition is done in ultra-high vacuum (UHV), the evaporated atoms generally do not interact neither with each other nor with atoms of the background gases until they reach the substrate surface.

In MBE, the number of controllable parameters during growth is rather limited. The substrate temperature is one of the most crucial parameters because it influences both the crystalline quality and the growth rate of layers and the Si NWs [60]. In epitaxial growth, the impinging adatoms do not stay at their place of impact, but move across the surface until they reach an energetically favourable position. This surface diffusion can be described as a random walk process with a hopping rate $\boldsymbol{\Gamma}$ defined by

$$\Gamma = \nu_S \exp\left(-\frac{E_A}{k_B \cdot T}\right) . \tag{4}$$

In (4) $\boldsymbol{\nu_S}$ is the attempt frequency and $\boldsymbol{E_A}$ is the activation energy required to move an atom from one position to another. This energy can, for instance, be provided by a certain thermal energy $\boldsymbol{k_B \cdot T}$, where $\boldsymbol{k_B}$ is Boltzmann's constant and $\boldsymbol{T}$ the absolute temperature. Thus the probability of surface diffusion increases with increasing temperature. As a result the crystalline quality of the growing film or NW is improved. But at the same time the desorption rate $\boldsymbol{R_D}$ also increases exponentially with $\boldsymbol{T}$:

$$R_D \sim \exp\left(-\frac{E_B}{k_B \cdot T}\right) , \tag{5}$$

where $\boldsymbol{E_B}$ is the binding energy. Therefore, the temperature can not be increased to much since otherwise the growth rate would drop to zero. An optimum temperature for deposition must be found, which depends on the material, the crystal structure of the substrate and its crystalline orientation.

Besides the substrate temperature, the flux rate of the particle beams and thus (at a fixed temperature) the growth rates and the composition can be adjusted, while the thickness is determined by the deposition time.

However, many other aspects might influence the outcome of an experiment, including the ballistic energy of the deposited material, the wafer orientation, its doping type and concentration, and also the wafer miscut. Often a miscut of a few per cent is favoured over a precisely cut wafer because the edges of the terraces on the wafer surface act as nucleation points for crystal growth.

The greatest advantage of MBE is its precise growth control due to slow growth rates and the deposition in an UHV environment. However, the slow growth rates may also be considered as a disadvantage. Often, the growth is monitored *in situ* by reflection high energy electron diffraction (RHEED), allowing the investigation of epitaxial orientation, the growth mode (2D layer-by-layer (Frank-van-der-Merwe), 3D island formation (Volmer-Weber), or a mixture (Stransky-Krastanov)), and, especially for layer-by-layer growth, the direct count of the number of atomic layers deposited by observation of the characteristic oscillation of the reflected beam [77].

Technical Details

The VLS NW growth and the Si/Ge superlattice heterostructure deposition was performed in a Riber SIVA 45 MBE machine (Figure 2). It consists of three chambers: a loading chamber, a buffer chamber and the deposition chamber. Each chamber can be evacuated separately by turbomolecular pumps. Additionally, the deposition chamber is equipped with a Ti sublimation pump and cooling traps which are filled with liquid nitrogen. Thus the background pressure can be reduced below 10^{-8} Pa.

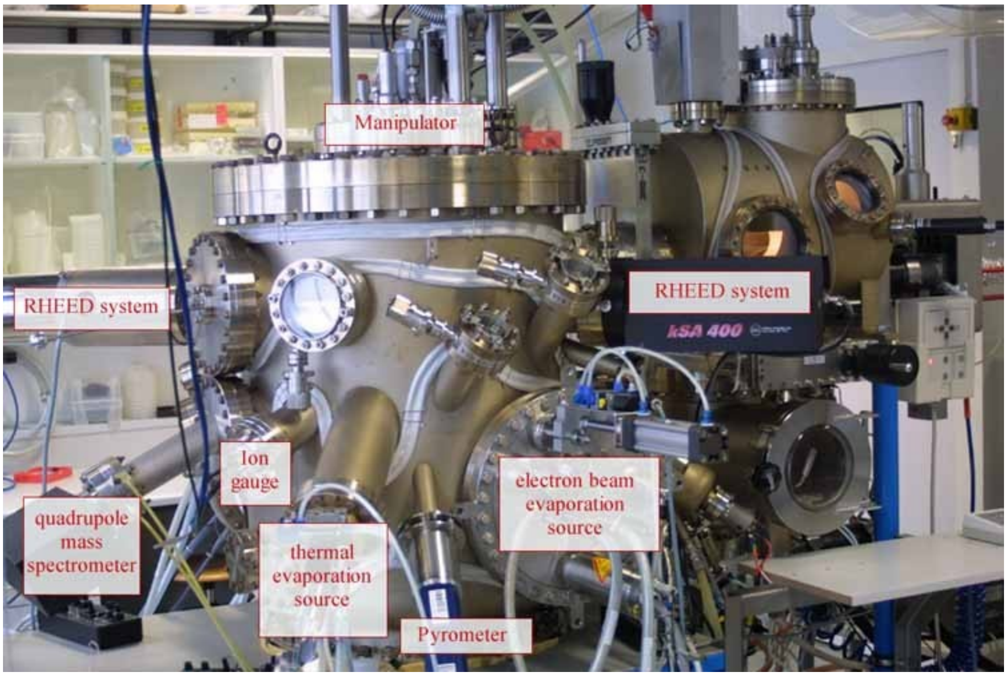

Figure 2: This image shows the Riber SIVA 45 MBE machine and some essential components.

For the deposition of Au, Si and Ge the machine is equipped with three 10 kV electron beam evaporation sources. In an e-beam evaporator, the deposition material is heated locally at its surface by an electron bombardment until it eventually evaporates into the vacuum and later condenses onto the substrate. The deposition rate can be adjusted by the electron flux, but it also depends on the substrate temperature. Conventional effusion cells provide the possibility of p-type doping with boron (B) and n-type doping with antimony (Sb) during growth.

Phosphorous (P) doped 5” Si (111) wafers were used as substrates for the NW growth experiments. The superlattice structures for the top-down approach were grown on either Si (111) or Si (100) substrates. Prior to the experiments the wafers were cleaned by the conventional RCA I and RCA II procedure as described in literature [78,79]. After cleaning, up to six wafers were loaded into the MBE machine and stored inside the buffer chamber.

For an experiment, the selected wafer was transferred into the deposition chamber and placed below a heater. Next, the native oxide layer which is left after the RCA process to protect the wafer surface was removed during an annealing step (870 °C for 20 min). Afterwards the temperature was lowered to the desired growth temperature and the experiment could be started.

The temperature was measured by a thermocouple (type C) placed between heater and substrate ($\boldsymbol{\vartheta_H}$) and regulated by the adjustment of the current applied to the heater. However, because of the distance between substrate and heater, the temperature of the substrate ($\boldsymbol{\vartheta_S}$) is significantly lower. Furthermore, it can not be measured directly during an experiment. Therefore, for each wafer type a separate temperature calibration was performed before a growth period (2-3 months). A thermocouple was welded into a wafer and $\boldsymbol{\vartheta_S}$ was measured as a function of $\boldsymbol{\vartheta_H}$. These calibration curves were then applied to adjust the temperatures during the subsequent experiments.

While the thickness of the growing Au film was directly measured *in situ* by an oscillating quartz crystal, the calibration of the growth rates for Si and Ge was also done before a growth period by correlation of particle fluxes measured by a quadrupole mass spectrometer to the thickness of the corresponding film obtained by *ex situ* TEM measurements. During an experiment the particle fluxes were measured by the same quadrupole mass spectrometer and automatically adjusted by regulation of the electron flux of the electron beam evaporation sources. Also, the substrate was rotated during deposition to ensure homogeneous growth.

2.2 Heteroepitaxy and Formation of Dislocations

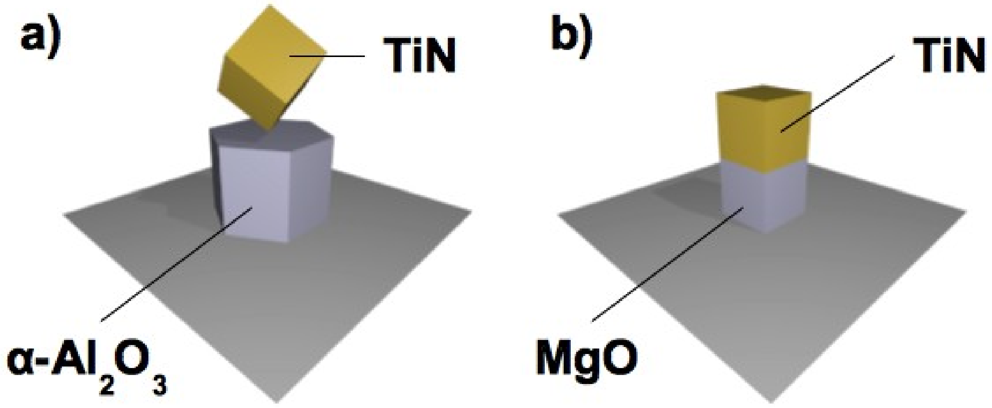

Scheme 5: Visualization of heteroepitaxial growth: a) TiN (cubic lattice) grown on c-plane sapphire (hexagonal structure); b) TiN (cubic lattice) grown on MgO (cubic lattice)

<u>*Heteroepitaxy*</u>

If a single crystalline film is grown on a substrate of the same single crystalline material, the deposition process is called *homoepitaxial growth*. In contrast, in case of *heteroepitaxial growth*, the deposited single crystalline material differs from the single crystalline substrate material. Besides the difference in the elemental composition, this might also refer to the lattice type and lattice parameters. Heteroepitaxy can be demonstrated quite nicely, for instance, by the deposition of TiN on different substrates (Scheme 5). If TiN is grown on a c-plane sapphire crystal, which is composed of a-Al_2O_3, almost all parameters are different. The crystal structure of sapphire is hexagonal with the hexagon lying in the c-plane. On the other hand, TiN crystallizes in a simple cubic system. If TiN is epitaxially grown on c-plane sapphire, the TiN lattice adapts and grows with the <111> direction oriented parallel to the c-axis of the sapphire crystal (Scheme 5a), resulting in a lattice mismatch of +9,2 per cent [80,81]. In contrast, if TiN is grown on a (100) MgO substrate, which is also a simple cubic lattice, the lattices fit quit nicely, resulting in a cube-on-cube epitaxy (Scheme 5b) with a lattice mismatch of only one per cent [82,83].

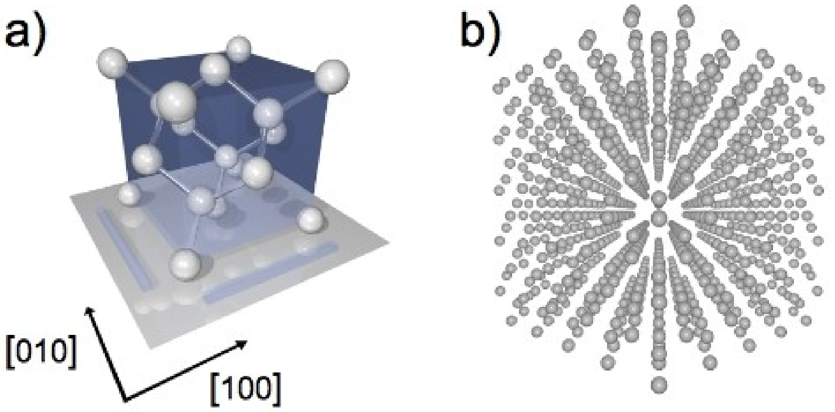

Scheme 6: The diamond cubic crystal structure: a) The volume within the blue box (including the intersections with the spheres on the corners and at the middle of the side walls) represents the unit cell of the diamond cubic structure. b) The right scheme shows a projection of the crystal lattice in <110> direction.

Heteroepitaxial Growth of Ge on Si

In the case of Si and Ge, both elements crystallize in a *diamond cubic crystal structure* (Scheme 6). A diamond lattice can be described as two face-centred cubic lattices displaced by ¼ of the body diagonal (Scheme 6a). Each atom is connected to four other atoms via hybridized sp^3-sp^3-σ-bonds. The angle between the bonds is 109.5°, thus the atoms form tetrahedrons.

Despite the identical lattice structure, the epitaxial growth of defect-free single crystalline Ge on Si is difficult. The reason is the difference in the lattice parameter, resulting in a lattice mismatch of approx. +4 per cent for Ge compared to Si. The lattice mismatch $\boldsymbol{f}$, after Frank and van der Merwe [84], is defined as

$$f = \frac{a_e - a_s}{a_s}\ , \tag{6}$$

with $\boldsymbol{a_e}$ being a lattice parameter of the epitaxial layer perpendicular to the growth direction and $\boldsymbol{a_s}$ the corresponding lattice parameter of the substrate. The lattice parameters for Si and Ge are given in Table 2. However, the lattice constant is not a constant at all. It depends on the pressure $\boldsymbol{p}$ and the temperature $\boldsymbol{T}$. Furthermore, the linear thermal expansion coefficient, $\boldsymbol{\alpha}$, of Ge is three times higher than the linear thermal expansion coefficient of Si. Therefore also the lattice mismatch $\boldsymbol{f}$ depends on the growth temperature, although the variations might be very small.

Element	***Bond Length****	***Lattice Constant****	***Linear Thermal Expansion Coefficient****
Si	$l_B = 0.235$ nm	a = 0.5431 nm	$\boldsymbol{\alpha} = 2.595 \cdot 10^{-6}\ \mathrm{K}^{-1}$
Ge	$l_B = 0.245$ nm	a = 0.5679 nm	$\boldsymbol{\alpha} = 6 \cdot 10^{-6}\ \mathrm{K}^{-1}$

*Table 2: Selected properties of Si and Ge, part II. * at **T** ≈ 300 K.*

Pseudomorphic Growth and Critical Thickness

For heteroepitaxial growth with identical crystal structures the first few monolayers of the deposited material adapt to the lattice parameters of the underlying substrate in the directions within the growth plane. This adaptation is called *pseudomorphic growth*. (However, in growth direction the lattice of the deposited material usually does not adapt, i. e. it remains relaxed.) The lattice mismatch results in an accumulation of biaxial strain energy in the growing layer, which is tensile for $\boldsymbol{f} < 0$, e. g. Si grown on Ge, and compressive for $\boldsymbol{f} > 0$, e. g. Ge grown on Si. The pseudomorphic growth mode is retained until a critical thickness $\boldsymbol{h_c}$ is reached and the strain is partly released by the formation of misfit dislocations. In principle, the critical thickness is defined as the thickness where the strain energy of the grown coherent layer (which depends on the thickness) and the energy of the dislocated system are the same. Above $\boldsymbol{h_c}$ the formation of dislocations becomes favourable to lower the overall energy of the system. For most of the calculations of the critical thickness it is assumed that the misfit dislocations form a regular, non-interacting rectangular array ('regular network of misfit dislocations').

First calculations of the critical thickness were presented by Frank and van der Merwe based on a thermodynamic equilibrium model [85], and later by Matthews and Blakeslee based on the consideration that the force associated with the strain and the line tension of the misfit dislocation balance each other at the critical thickness [86-88]. In [86] Matthews and Blakeslee derived the following equation for the critical thickness:

$$h_c = \frac{|\vec{b}|}{2 \cdot \pi \cdot f} \cdot \frac{(1 - \nu \cdot \cos^2 \theta)}{(1 + \nu) \cdot \cos \lambda} \cdot \left[\ln \left(\frac{h_c}{|\vec{b}|} \right) + 1 \right], \tag{7}$$

where $\vec{b}$ is the dislocation's Burgers vector, $\boldsymbol{\theta}$ is the angle between dislocation line and Burgers vector, $\boldsymbol{\nu}$ is the Poisson ratio, and $\boldsymbol{\lambda}$ is the angle between the Burgers vector and the direction in the interface normal to the dislocation line. For the Si-Ge system $\cos \boldsymbol{\lambda} = \cos \boldsymbol{\theta} = 0.5$.

The actual lattice mismatch ***f*** of a Ge layer grown on Si depends on the Ge content ***X*** which is achieved in the epitaxially grown layer. Due to reasons discussed in a later section, the Ge concentration is usually below 100 per cent, even if pure Ge is deposited. Thus, in reality, a $Si_{1-X}Ge_X$ binary alloy is obtained which is miscible over the full composition range. The alloy's lattice parameter varies, according to *Vergard's Law*[1], linearly with the Ge content:

$$\boldsymbol{a}(Si_{1-X}Ge_X) = (1-\boldsymbol{X}) \cdot \boldsymbol{a}(Si) + \boldsymbol{X} \cdot \boldsymbol{a}(Ge). \tag{8}$$

As a result ***f*** can be calculated by the following formula:

$$f(X)=0.042 \cdot X. \tag{9}$$

Combining (7) and (9) an approximation of equation (6) for the Si-Ge system is given by [90]:

$$h_C \approx 1.7793 \cdot X^{-1.2371}. \tag{10}$$

Resulting lattice mismatches and the corresponding critical thickness for different compositions are shown in Table 3.

$Si_{1-X}Ge_X$			
X	0.25	0.5	1
f	≈ 0.011	≈ 0.021	≈ 0.042
h_C	≈ 9.9 nm	≈ 4.2 nm	≈ 1.8 nm

Table 3: Lattice mismatch and critical thickness for different compositions of $Si_{1-X}Ge_X$

However, experimental results especially at low growth temperatures showed a large deviation from the Matthews/Blakeslee model leading to a huge metastable regime [91-94]. A new approach was proposed by Dodson and Tsao [95,96], who account for the temperature dependence. Extensive studies were also done by Houghton [97] who also considered the nucleation of dislocations and glide velocities in single and multiple epilayers.

Nevertheless, since the metastable layer can relax over long times or under high stress the critical thickness calculated by the Matthew/Blakeslee equilibrium model is still the upper limit for functional strained $Si_{1-X}Ge_X$ layers in industrial devices. Figure 3 shows the dependence of the critical thickness of a Ge layer on the Ge content according to the Matthew/Blakeslee model as well as the metastable regime for MBE growth at 550°C, where the critical thickness depends on the growth conditions, especially the temperature.

---

[1] Deviations from this law are discussed in [89].

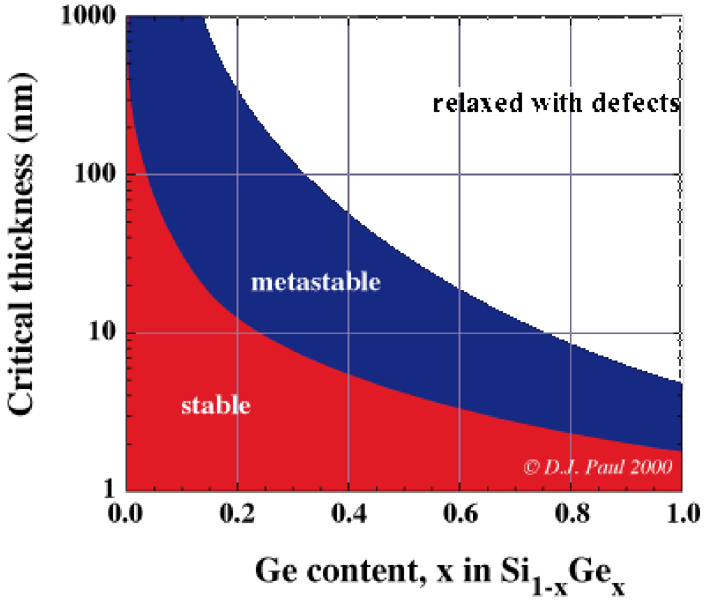

*Figure 3: Critical thickness of Ge layer growth on Si depending on the Ge content **X**. [98]*

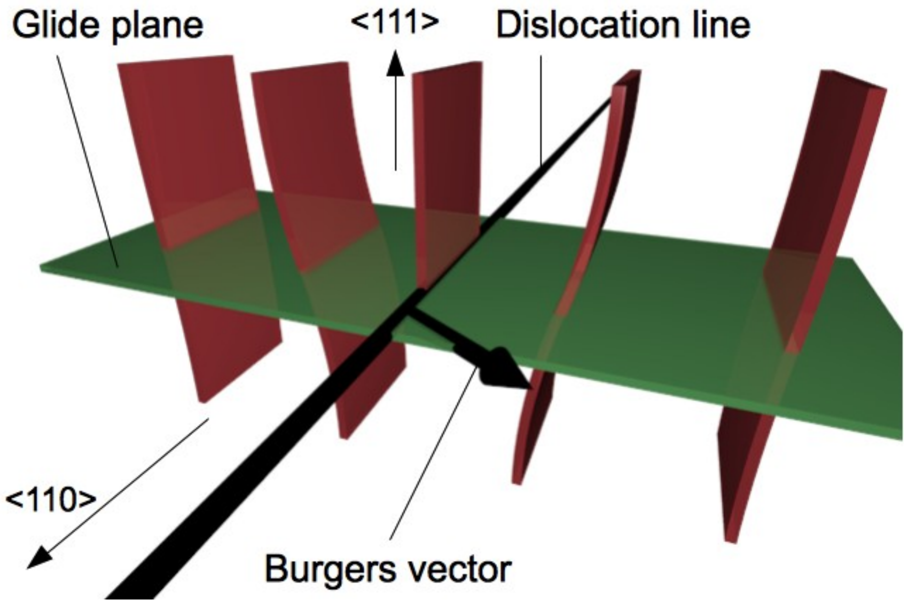

Figure 4: Typical dislocation in a diamond cubic lattice. Both Burgers vector and dislocation line are aligned in <110> directions with an angle of 60° in between. The glide plane is a {111} plane.

Dislocations in the Diamond Lattice

In the diamond cubic lattice, dislocations lie primarily along <110> directions (Figure 4), with a Burgers vector ½ <110> [99]. The glide plane is the {111} plane which is also the plane with the highest density of atoms. Because dislocation line and Burgers vector are inclined at an angle of $\theta = 60°$ in their projection on the glide plane, the dislocations are called 60° dislocations. These 60° dislocations can be split into a 30° and a 90° *Shockley partial dislocation* with a stacking fault in between. For each dislocation line there are two possible {111} glide planes, each of them containing four potential Burgers vectors.

Surface Energy and Germanium Segregation

But the formation of misfit dislocations is only one challenge when growing Ge on Si. It is also difficult to obtain Si/Ge heterostructures with abrupt interfaces due to the segregation of Ge. The reason for the segregation is the low surface energy γ of Ge relative to Si (Table 4) [100]. A high surface saturation of Ge (approx. 90%) is required before steady state films are growing [101]. Thus the shape of the leading interface resembles an error function because a certain time is required until the equilibrium value is reached. Naturally, the leading interface sharpens with higher Ge fluxes [101,102]. If then again intrinsic Si is grown on top, the surface acts as a Ge source leading to Ge incorporation in the growing Si film. This results in a trailing interface with its shape resembling an exponential decay function [101,103,104]. The Ge segregation can be partially eliminated by saturation of the dangling bonds with low energy surfactants, e. g. Ga or Sb. However, these surfactants simultaneously act as dopants in the growing film, changing, for instance, the optical and electrical properties [103].

Element	***Orientation***	***Surface Energy γ***
Si	(100)	1.41 J · m^{-2}
	(111)	1.36 J · m^{-2}
Ge	(100)	1.00 J · m^{-2}
	(111)	1.01 J · m^{-2}

Table 4: Surface energy of Si and Ge depending on crystal orientation.

2.3 Crystal Defects in Nanowires

Crystal Defects

In general, crystal defects are divided into four categories, depending on their dimensionality (0D, 1D, 2D, 3D). However, 3D defects (*voids* and *precipitates*) and planar defects (2D), which include *stacking faults*, *grain boundaries* and *anti phase boundaries*, are not the subject of this work. Nevertheless it must be mentioned that the surface of a crystal and thus also the surface of a NW can be regarded as an interruption of the crystal lattice and therefore represents a two-dimensional defect.

Vacancies, *interstitials* and *substitutional atoms* are referred to as point defects (0D). The latter two also include dopant atoms, although they are incorporated intentionally. Linear defects (1D) in solid materials are called *dislocations*. They have already been mentioned above. The strain field induced by dislocations and the dangling bonds which are introduced into the lattice alter the properties of the material. They act, for instance, as a linear arrangement of charged scattering centres and are reducing the charge carrier mobility. Therefore the presence of dislocations is of great concern in device engineering. The following sections deal with Au atoms which can be incorporated into the NWs as point defects during growth, and the formation and behaviour of misfit dislocations in NWs.

Gold Contamination in Nanowires

The solubility of Au in Si is of special interest since Au is usually the preferred catalyst for Si NW growth via the VLS mechanism. The main advantage of the Au-Si system is the existence of a low temperature eutectic melt. Compared to other metals, e. g. silver, this allows the rapid growth of NWs at low temperatures. However, Au also acts as a deep level impurity in Si, with energy levels roughly at the middle of the band gap [105]. Au impurity atoms at substitutional sites are effective recombination centres in Si and thus reduce the charge carrier lifetime [106]. Therefore, the inclusion of catalyst atoms must be avoided for most of the desired applications. An exception are high frequency applications with very fast switching times where the Au contamination does not interfere with the desired properties or even supports them [107].

The bulk solubility of Au in Si has never been measured for lower temperatures which are in the range of 400-600°C. Extrapolations from results measured at higher temperatures (e. g. 10^{17} cm^{-3} at 1300 °C [108]) indicate a solubility of Au in Si in the range of 10^{14} cm^{-3} at 450 °C [109].

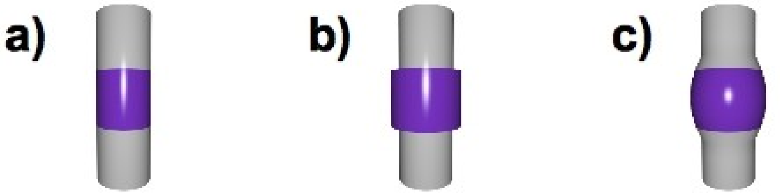

Figure 5: Lateral expansion in nanowires. a) NW heterostructure if there is no lattice mismatch. b) Illustration of a possible lattice mismatch. c) Illustration of the lateral expansion in a NW heterostructure where the individual lattices are strained to adapt to each other.

Dislocations in Nanowires

In contrast to their bulk counterparts NWs can expand not only in growth direction, but also in lateral direction (Figure 5). This lateral expansion might also release a certain amount of strain energy accumulated during heteroepitaxial, pseudomorphic growth. Following this thought, a critical NW radius $\boldsymbol{r_C}$ can be postulated. Below this radius, the lateral expansion prevents the formation of misfit dislocations in the growing NW. Above the critical thickness, the lateral expansion might increase the critical thickness $\boldsymbol{h_C}$, but eventually dislocations are formed anyway.

Theoretical calculations on $\boldsymbol{r_C}$ were performed by Ertekin *et al.* [110] and Kästner *et al.* [18]. Ertekin *et al.* used a simple model for their first attempt, in analogy to the equilibrium models used by Matthews/Blakeslee and Frank/van der Merwe for the calculations of the critical thickness, to compare a coherent, undislocated system with a system containing a perpendicular pair of intersecting misfit dislocations in the interfacial plane which both run through the centre of the plane. For their model system comprising a single, infinitely thick NW substrate and a single, infinitely thick NW overlayer with an atomically sharp interface in between, they obtained a critical radius where the coherent, undislocated structure becomes unstable, i. e. its energy is higher than the energy of the dislocated system [110]. The calculated critical radius in this model is more than five times larger than the corresponding critical thickness for the same lattice mismatch.

However, the model of Ertekin *et al.* only considered one particular set of preexisting misfit dislocations which might not be the optimum configuration for strain relaxation. Therefore, Kästner *et al.* calculated the critical radius based on the assumption of a preexisting misfit dislocation which can move in the interface plane and rest in any possible minimum [18]. This is similar to the approach of Matthews/Blakeslee who used an existing threading dislocation as the source for the generation of the misfit dislocation.

The local minimum in terms of energy was found for a straight dislocation half-loop running along the diameter of the cylindrical NW. However, this minimum vanishes if the radius is below a critical radius $\boldsymbol{r_C}$. The dislocation then becomes unstable and is pushed towards the NW surface. For the critical radius Kästner *et al.* obtained the following equation (for 60° dislocations):

$$r_C = \frac{|\vec{b}|}{f} \cdot \left(0.12 \cdot \ln \frac{8 \cdot r_C}{|\vec{b}|} + 0.18 \pm 0.37 \right), \tag{11}$$

where the last term is positive if an atomic slip step is created at the NW surface by the dislocation, which is the usual case, or negative if a preexisting slip step is accidentally annihilated. As a rule of thumb, Kästner gives the formula

$$\frac{r_C}{|\vec{b}|} \approx \frac{1}{f} \tag{12}$$

if a slip step is created, and

$$\frac{r_C}{|\vec{b}|} \approx \frac{1}{2 \cdot f} \tag{13}$$

if a slip step is annihilated.

A comparison of results obtained by Ertekin *et al.* and Kästner *et al.* is given in Table 5. However, two things must be kept in mind: First, these radii were calculated for an abrupt heterotransition which yields the highest possible stress. The critical radius might be significantly higher for NWs with a non-abrupt heterotransition which is the case for most grown NWs. Second, both models are based on preexisting dislocations. Kästner suggests that the probability of nucleating a dislocation in a NW, even if its radius is above the critical radius, is very low because of the high activation energy for the nucleation of a dislocation half-loop in a nanowire [18].

$Si_{1-X}Ge_X$			
X	0.25	0.5	1
f	≈ 0.011	≈ 0.021	≈ 0.042
r_C (Ertekin)	≈ 85 nm	≈ 42 nm	≈ 18 nm
r_C (Kästner)	≈ 50 nm	≈ 25 nm	≈ 12 nm
r_C (Kästner) *(rule of thumb)*	≈ 36 nm	≈ 19 nm	≈ 9.8 nm

Table 5: Lattice mismatch and critical radius for the stability of a misfit dislocation in a nanowire growing in <111> direction for different compositions of $Si_{1-X}Ge_X$

Dislocations in Etched Nanowires

If NWs are etched in a Si/Ge heterostructure containing dislocations, there is a certain probability that an individual NW might also contain a dislocation (Figure 6). This probability increases with increasing radius $\boldsymbol{r}$ and increasing NW density $\boldsymbol{\rho_{NW}}$.

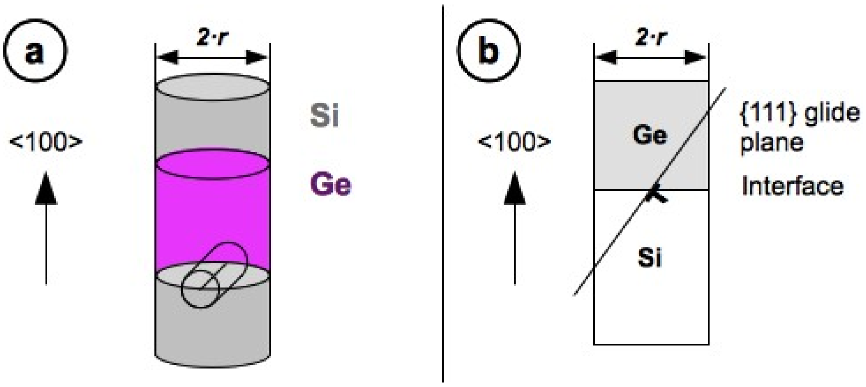

Figure 6: a) Si/Ge nanowires may contain a dislocation half-loop after etching. b) Projection of the glide plane in a <100>-oriented Si/Ge heterostructure NW.

As shown above, this dislocation is unstable if the NW radius is below the critical radius $\boldsymbol{r_C}$, resulting in a driving force to move the dislocation out of the NW by a *dislocation glide* process. Dislocation glide is the conservative motion of dislocations along the direction of closest spacing in the (glide) plane which contains both the dislocation line and its Burgers vector. Dislocations can move if the atoms from one of the surrounding planes break their bonds and re-bond with the atoms at the terminating edge. The movement of the dislocation might finally stop at a grain boundary or another surface, i. e. the NW surface, where the dislocation eventually vanishes.

It has been shown in literature that dislocation movement can be initiated by a thermal annealing process [111]. For Si and Ge, dislocation movement was investigated for temperatures above 500-600 °C. The velocity $\boldsymbol{v}$ (in mm/s) of moving dislocations in a $Si_{1-X}Ge_X$ layer is generally given by the empirical law

$$v=9.8\times10^{4}\cdot(\tau_{eff})^{2}\cdot\exp\left(-\frac{E_A}{k_B\cdot T}\right), \tag{14}$$

where $\boldsymbol{\tau_{eff}}$ is the effective stress in MPa, and $\boldsymbol{E_A}$ the activation energy for dislocation movement. In Si the activation energy is ≈ 2.25 eV, however, it depends strongly on impurities and the doping concentration [111]. An upper limit for the velocity of moving dislocations is the speed of sound in this crystal lattice along the direction.

3 Analytical Methods

The NWs fabricated by both the bottom-up and the top-down approach were investigated by different methods of electron microscopy. They are briefly outlined in this chapter. Reflection high energy electron diffraction is described in detail in [77]. Further information concerning scanning electron microscopy can be obtained in [112]. More details on conventional and analytical transmission electron microscopy are given in [113], [117] and [118].

3.1 *In situ* Methods

The experimental set-up of PVD deposition techniques prevents the application of most analytical methods because the hemisphere above the sample surface is filled with deposition sources. Furthermore, any potential analytical method must not interfere with the growth process. In the case of reflection high energy electron diffraction (RHEED), the electron beam hits the sample at a glancing angle of only about 2°. Therefore the electron gun can be easily mounted to the machine without any interference with the deposition sources. RHEED is often the method of choice for *in situ* observations during MBE growth processes.

3.1.1 Reflection High Energy Electron Diffraction

Working Principle

Reflection high energy electron diffraction (RHEED) is based on a high energy electron beam hitting the sample at a glancing angle of only a few degrees, then being diffracted by the first few monolayers of the sample material. RHEED is a surface sensitive method, revealing time-resolved information on the crystal structure and the surface morphology of the sample.

Equipment Configuration

Compared to other methods, the RHEED set-up is rather simple. It consists of an electron gun and attached deflexion units mounted on one side of the chamber and a fluorescent screen on the opposite side. Often a CCD camera is placed behind the screen.

Image Formation

Diffraction occurs if a wave interacts with periodic arrangements of particles, like a crystal lattice, and the wavelength has the same order of magnitude as the period length or below. In this case, electrons with a *de Broglie wavelength* $\boldsymbol{\lambda_e}$ are scattered at atoms in crystal lattices whenever *Bragg's Law*

$$2 \cdot d_{hkl} \cdot \sin \Theta = k \cdot \lambda_e \tag{15}$$

is fulfilled. $\boldsymbol{d_{hkl}}$ represents the distance between the lattice planes described by the set of Miller indices ***hkl***, $\boldsymbol{\Theta}$ the glancing angle, and ***k*** the diffraction order. The kinetic energy $\boldsymbol{E_{kin}}$ of the electrons is given by

$$E_{kin} = e \cdot U_{acc} \,, \tag{16}$$

where $\boldsymbol{U_{acc}}$ is the acceleration voltage. The velocity of the electrons can be calculated using the relativistic equation

$$E_{kin} = m_e \cdot c_0^2 \cdot \left(\sqrt{1 - \frac{v_e^2}{c_0^2}} \right)^{-1} - m_e \cdot c_0^2 \,, \tag{17}$$

and $\boldsymbol{\lambda_e}$ can then be obtained through the equation

$$\lambda_e = \frac{h}{m_e \cdot v_e} \cdot \sqrt{1 - \frac{v_e^2}{c_0^2}} \,. \tag{18}$$

For an acceleration voltage $\boldsymbol{U_{acc}}$ of 30 kV, $\boldsymbol{\lambda_e}$ is approx. 0.007 nm.

Secondary electrons and inelastically scattered electrons often do not have the energy necessary to reach the screen [114]. Therefore mostly elastically scattered electrons contribute to the diffraction pattern. For the diffraction on a two-dimensional surface, the points of the reciprocal lattice are transformed to one-dimensional parallel rods [77]. The intersections of these rods in reciprocal space with the *Ewald sphere* with radius $|\vec{k}|$ create the diffraction pattern. For the wave vector $\vec{k}$, the wave vector $\vec{k}\,'$ of the diffracted beam and the lattice vector $\vec{g}$ in reciprocal space the equations

$$\vec{k}\,' = \vec{k} + \vec{g} \tag{19}$$

and

$$|\vec{k}\,'| = |\vec{k}| \tag{20}$$

are valid. The scattering angle is given by

$$|\vec{g}| = 2 \cdot |\vec{k}| \cdot \sin \varphi \tag{21}$$

with $\boldsymbol{2\varphi}$ being the angle between $\vec{k}$ and $\vec{k}\,'$ [115]. However, in the case of island formation or NW growth on the crystal surface, a *transmission electron diffraction* (TED) pattern is observed in analogy to transmission electron microscopy (TEM) investigations.

Obtainable Information

RHEED allows to obtain valuable time-resolved information on the crystal structure of the substrate and the deposited material. Furthermore, first information on the epitaxial orientation of the growing material is revealed, allowing the adjustment of process parameters during growth, eventually changing the crystal structure of the epilayer [116]. Furthermore it allows the investigation of the growth mode and growth rate of materials. It also gives first indications on the growth of NWs on a substrate and their crystal orientation, although the informations must be verified *ex situ*, e. g. by scanning electron microscopy or transmission electron microscopy.

Examples of diffraction patterns obtained by RHEED during MBE NW growth are shown in Figure 7. The first two pictures show the typical 7x7 surface reconstruction of (111)-oriented Si surfaces. After NW growth the pattern has changed to a TED pattern indicating a 3D growth (Figure 7c).

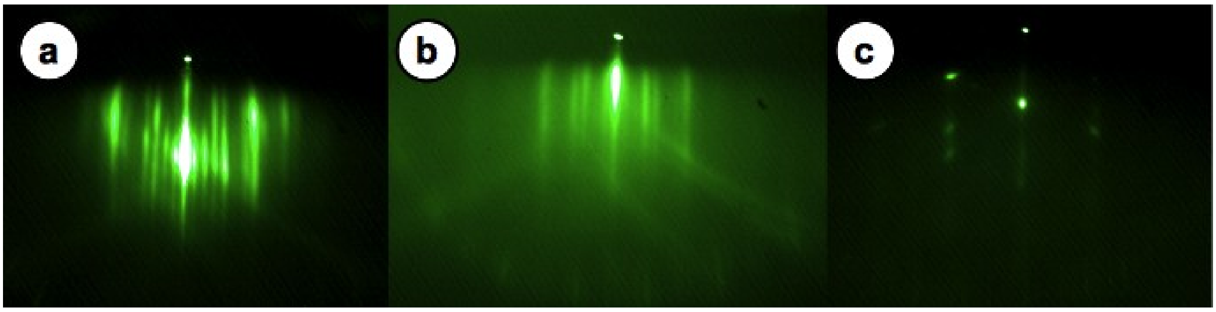

Figure 7: Diffraction patterns obtained by RHEED during MBE NW growth: a) Wafer surface prior to deposition process. b) After deposition of Si buffer layer. c) After NW growth.

Technical Details

For the *in situ* investigations of the MBE process, a 35 kV STAIB Instruments NEK 35 R RHEED system was used, although it was operated at only 30 kV.

3.2 *Ex situ* Methods

3.2.1 Scanning Electron Microscopy

Working Principle

In scanning electron microscopy (SEM) the sample is scanned with a high energy electron beam ($U_{acc} \approx$ 1 kV to 40 kV). Simultaneously, backscattered electrons and secondary electrons are detected. By correlating the detector signals with the beam position, a distribution map of the intensity of the signal is created.

Equipment Configuration and Image Formation

Like in RHEED or transmission electron microscopy (TEM), the electron beam is thermionically emitted from the cathode filament of an electron gun. The beam is then focussed by condenser lenses and passes the scanning coils or pairs of deflector plates, deflecting it in the x and y axes. The backscattered electrons and secondary electrons generated in the interaction volume of the beam with the sample material can be detected by specialized detectors.

The detector signals are displayed as variations in brightness on a computer monitor. Because the scanning of the display is synchronised with the scanning of the beam on the specimen in the microscope, the resulting image is a distribution map of the intensity of the signal being emitted from the scanned area of the specimen. While the interaction volume depends on the electron energy, the atom number of the atoms in the specimen and the specimen's density, the scattering processes are also greatly influenced by the morphology and surface topology.

Obtainable Information

By SEM valuable information on the morphology and surface topology of the sample can be obtained. Furthermore, in combination with analytical techniques like energy dispersive X-ray spectroscopy (EDX), SEM enables the microscopist to gather information on the elemental composition of the specimen.

Technical Details

The majority of the SEM micrographs were taken on a JEOL JSM-6701F Field Emission Scanning Electron Microscope which is equipped with a cold field emission cathode at an acceleration voltage of 8 kV. The error of both the magnification and thus the resulting dimensions was below 10%.

3.2.2 Transmission Electron Microscopy

Working Principle

Transmission electron microscopy (TEM) is another valuable and versatile technique for the characterisation of solid materials. Inside the electron microscope, the sample is exposed to a confined beam of high-energy electrons. Unlike in SEM, the beam is not supposed to be reflected and scattered on the sample surface, but instead to pass through the sample. Although the acceleration voltage and thus the kinetic energy of the electrons is larger by approximately an order of magnitude, the sample still has to be very thin to allow the transmission of the beam. If this condition is fulfilled, TEM enables the microscopist to collect information about the inner structure of the material (crystal class, lattice parameter, defects such as dislocations), and also the chemical composition almost simultaneously. This, however, comes at the cost of an expensive set-up and a laborious sample preparation procedure.

Sample Preparation

For cross-section investigations, two samples are glued face to face and cut into thin (≈ 300 µm) slices perpendicular to their surfaces and perpendicular to the <110> direction. One of these slices is then embedded into a copper or ceramic ring with a diameter of 3 mm. This specimen is then thinned even further down to a few ten µm. Afterwards it is exposed to an ion beam under a glancing angle of 3 – 6° until a tiny hole is formed in the middle of the specimen. The edges of this hole are transparent to the electron beam. For plan view samples, a small piece of the sample is embedded into the 3 mm copper or ceramic ring. The back side is then treated analogical to the cross-section samples.

Equipment Configuration and Image Formation

Besides the high energy electron gun, the microscope contains several sets of electromagnetic lenses to collimate and focus the electron beam. The interaction of the beam with the specimen takes place in the central section of the microscope, in the objective plane of the objective lens. A simplified representation of the optical paths within this section of the microscope is shown in Figure 8. The objective lens focusses the electrons leaving the specimen and forms a diffraction pattern in the back focal plane of the lens, and an (intermediate) image of the specimen in the (first) image plane. In the conventional TEM the diffraction pattern or the image can be projected and magnified on the final screen by the projective system, another set of electromagnetic lenses located below the objective lens.

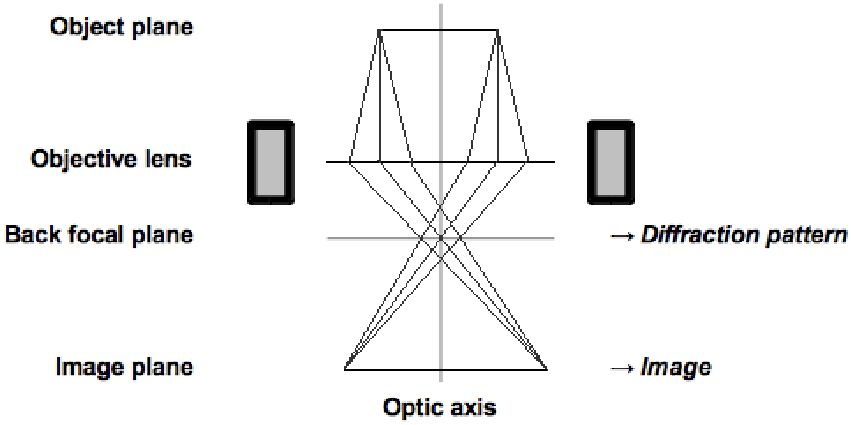

Figure 8: Schematic view of the optical paths in the central section of a transmission electron microscope.

Bright Field Image

The primary electron beam is used to generate a bright field image. Brighter and darker areas in this image are created by absorption or diffraction of electrons within the specimen. While the diffraction contrast reveals information on crystallites, grain boundaries, defects and strain, the absorption contrast is linked to variations in the thickness and/or the chemical composition of the material. The latter was used to generate profiles of the concentration of Ge within the Si/Ge heterostructures (see below).

Dark Field Image

Alternatively, the primary beam can be blanked out and a diffracted beam can be selected instead for the image generation by choosing a reflex ***hkl*** with an aperture. The image is then referred to as a ***hkl**-dark field image*. This technique can, for instance, be used to look for the existence of specific crystal orientations or special features like dislocations in the specimen, including dislocation splitting.

High-Resolution Transmission Electron Microscopy

To achieve resolution at the atomic scale, an interference pattern of the primary beam and one or more diffracted beams can be produced. Thus the positions of the individual atoms within the crystal lattice are revealed, although they cannot be directly seen.

Obtainable Information

TEM allows to gather information on the internal structure of crystals including the orientation. At the same time crystal defects like dislocations or grain boundaries are revealed. Furthermore, differences in the chemical composition can be seen on a TEM image due to the absorption contrast, although there is no direct confirmation of the existence of a specific chemical element.

Concentration Profiles

Because of the lack of other, more sophisticated methods, the absorption contrast in TEM bright field images was used to gather information on the Ge concentration in NW heterostructures and the superlattice structures. Therefore, a line scan was performed perpendicular to the Ge layer, and the obtained intensity differences $\Xi_{SiGe}(x) - \Xi_{Si}$ were converted to a concentration profile by the following procedure: First, the integral

$$\int_{-\infty}^{\infty} (\Xi_{SiGe}(x) - \Xi_{Si})\,dx = A \tag{22}$$

was calculated. The Ge content was then obtained by

$$X(x) = \frac{\Xi_{SiGe}(x) - \Xi_{Si}}{\Xi_1} = \frac{\Xi_{SiGe}(x) - \Xi_{Si}}{A \cdot h^{-1}} \,. \tag{23}$$

where Ξ_1 is the expected intensity at $X = 1$. Ξ_1 was calculated by dividing the area A by the nominal Ge layer thickness h.

Possible Sources of Error

For the NWs grown by the bottom-up approach,

$$\Xi_1 = \frac{A}{h} \tag{24}$$

is only valid if there is no contribution of the surface diffusion to the NW growth, i. e.

$$I = I_1 + I_2 \overset{I_2=0}{=} I_1 \, . \tag{25}$$

This assumption is supported by the low mobility of Ge on Si surfaces. However, since Ge NW growth by MBE was observed at 360 °C, it can be assumed that $\mathbf{I_2}$ becomes larger than zero as soon as a closed Ge layer with a high Ge content is formed on the substrate surface. Then, as a result, the incorporated amount of Ge is higher than the one anticipated in the calculations above. Thus the calculated concentrations are the minimum values.

The error of the distances obtained by TEM measurements are below 3%. With $\boldsymbol{h}$ fixed, the Ge content $\boldsymbol{X}$ is proportional to $\boldsymbol{A^{-1}}$, which depends linear on the distance $\boldsymbol{x}$. For the Ge content, the error is therefore also roughly 3%. (An increase in the distance by a factor of 1.03 would lead to a modification of the Ge content by a factor of $(1.03)^{-1}$.)

In case of the superlattice structures grown as part of the top-down approach, the distance between the Ge peaks was normalized to the nominal layer thickness prior to the calculations of the Ge content. Therefore the results do not depend on the distance $\boldsymbol{x}$, and they should be accurate. Furthermore, the flux of atoms is not divided into two parts and can be regarded as uniform throughout the whole wafer surface.

Technical Details

The NWs were investigated in a Philips CM20 transmission electron microscope with an acceleration voltage of 200 kV. High-resolution TEM (HRTEM) was performed at a JEOL JEM-4010F with an acceleration voltage of 400 kV and a point resolution of 0.155 nm.

3.2.3 Energy Dispersive X-Ray Spectroscopy

Working Principle and Spectrum Generation

Energy dispersive X-ray spectroscopy (EDX) is an analytical technique used for the chemical characterisation of a sample [113]. Both scanning electron and transmission electron microscopes can be equipped with an EDX detector which is an energy dispersive spectrometer. In EDX the specimen is exposed to a high energy electron beam to stimulate the secondary emission of X-rays. If the incident electron beam excites an electron in an inner shell ***n*** of an atom, eventually ejecting it from the shell, an electron hole is left behind. This hole might be filled by an electron from an outer shell ***m*** with a higher energy. The energy difference

$$\Delta E = E_m - E_n = \hbar \cdot \omega \qquad (26)$$

is then released in the form of an X-ray with frequency ***ω***. The amount of X-rays and their individual energy can be measured by the spectrometer. As a result a unique spectrum is generated reflecting the elemental composition of the specimen. By moving the electron beam across the sample surface ("scanning"), concentration profiles can be obtained.

Obtainable Information

As mentioned above, EDX allows the detection of individual elements. It is a useful technique, complementing, for instance, TEM investigations where only differences in the composition can be seen due to changes in the absorption contrast. However, there are several limitations. First of all, the detector has a limited area, allowing only the detection of X-rays escaping the sample in the direction of the detector itself. Second, the spacial resolution is limited by the diameter of the electron beam. Therefore, a quantitative analysis and the detection of small quantities of atoms, e. g. impurities, is difficult. Furthermore, several elements have overlapping peaks, making it difficult to verify the existence of these elements unless the EDX spectrum is compared with data obtained by other analytical techniques. Also, EDX does not allow the detection of chemical compounds and molecules but only the elements they are made of. And, last but not least, the accuracy of the EDX spectrum decreases for lighter elements. Elements with atomic number below 5 cannot be detected at all because of the absorption of low-energy X-rays in windows in front of the detector [119]. The limitation of the spatial resolution is the reason why EDX could not be used for the generation of the Ge concentration profiles in the NWs and Si/Ge heterostructures because the diameter of the beam and especially the projection of the interaction volume are much larger than the thickness of an individual Ge layer within the superlattice structure.

Technical Details

The 200 kV Philips CM20 FEG microscope used for the TEM investigations was also equipped with an EDX detector for analytical investigations of the chemical composition of the samples.

4 Bottom-Up Approach

4.1 Vapour-Liquid-Solid Mechanism

Wagner and Ellis [34-36], and Givargizov [37,38] proposed and studied the vapour-liquid-solid (VLS) mechanism already in the 1960s and 1970s, respectively. Although this concept was first designed to explain the growth of NWs by CVD, it was later transferred to also describe the NW growth by PVD methods, including MBE. There are several differences between the two deposition methods, however, when looking at the details they have more things in common than expected at first glance.

The VLS mechanism requires a liquid catalyst to initiate the NW growth. The growth material is supplied to this tiny droplet in excess, leading to a supersaturation inside. The supersaturation initiates the precipitation of the material at the interface of the droplet with the substrate thus forming the NW. This process repeats until the material is no longer provided.

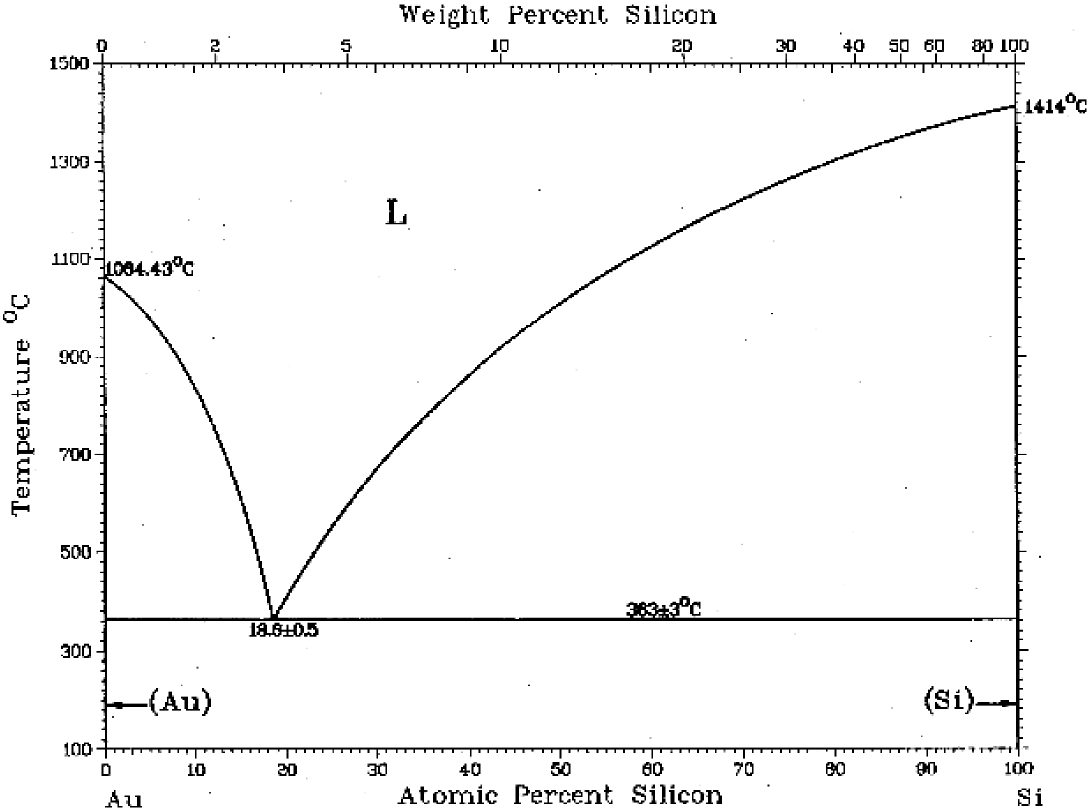

Figure 9: Au-Si Phase Diagram (the dependence on the pressure is not shown) [120]

Au is by far the most common catalyst for Si NW growth because the Au-Si system is a simple eutectic with a low melting point (Figure 9). The alloy becomes liquid at 363 °C at a composition of 81.4 at.-% Au and 18.6 at.-% Si. However, the phase diagram which is often quoted is only a simplified model for the bulk material. The influence of the pressure is not shown. Furthermore, the liquid-solid transition shows a hysteresis which means that the values for the cooling curves and heating curves might differ. For instance, Predel and Bankstahl obtained a value of 345 °C for the cooling curve [121].

The catalyst droplets are either formed by deposition of a thin Au film or by dropping Au colloids onto the wafer surface. In both cases a subsequent annealing above the eutectic temperature is necessary to obtain liquid Au-Si droplets which are randomly distributed on the substrate.

When growing Si/Ge heterostructure NWs, Ge atoms are also solved within the droplet resulting in a ternary alloy. This system was also extensively studied by Predel and Bankstahl who reported on the phase transition temperatures (cooling curves) in 1976 [122]. A projection of the Au-Ge-Si liquidus surface is shown in Figure 10. They found a minimum temperature of 326 °C at a composition of 79 at.-% Au, 7.5 at.-% Ge and 13.5 at.-% Si.

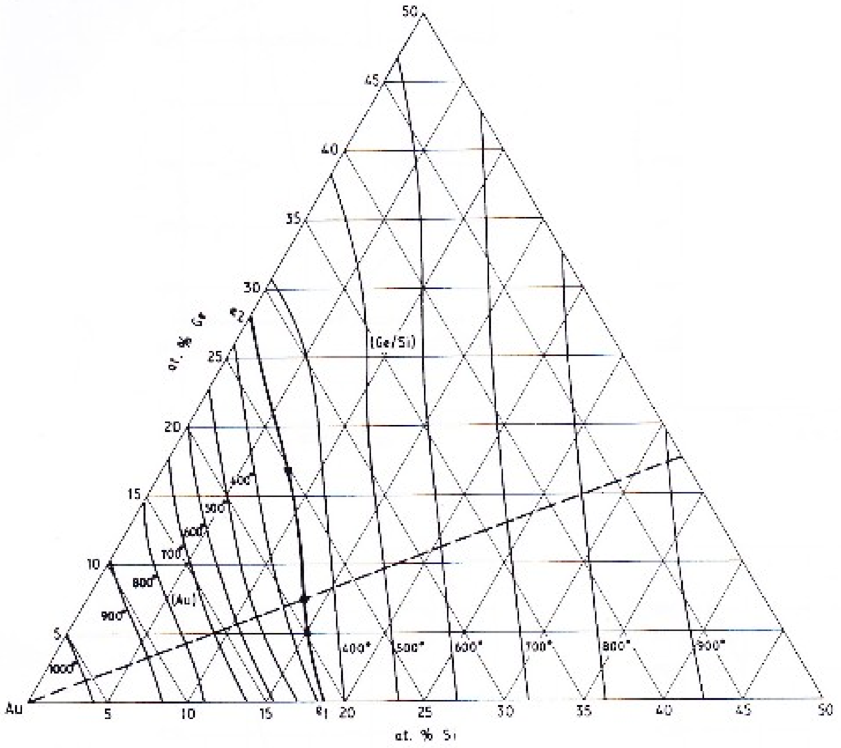

Figure 10: Au-Ge-Si Phase Diagram: Projections of the Au-Ge-Si liquidus surface for Au contents ≥50 at.-%

Silicon Nanowire Growth by Molecular Beam Epitaxy

The growth of Si NWs by MBE was studied in detail by Schubert *et al.* [55,57,60]. A short summary is given on the following pages. In contrast to CVD, the growth material is not provided as a precursor gas, but instead is deposited homogeneously on the whole surface as single atoms. Thus the droplets absorb the same amount of Si as the Si substrate. Therefore, both should grow at the same speed. However, the NWs below the Au-Si droplets grow faster than the epilayer. The reason is the surface diffusion which is additionally enhanced by an Au-Si wetting layer.

Surface diffusion of Si can be described as a random walk process of a single Si atom on the Si substrate surface. To allow the atom to change its position an activation energy $\boldsymbol{E_A}$ is required. This energy might be provided by an energy transfer through scattering events, e. g. the impingement of a Si atom onto the surface and the transfer of its ballistic energy, or by a thermal energy through substrate heating. The diffusion process continues until the atom reaches an anomaly on the surface, a place were the activation energy increases so that the probability for another diffusion step rapidly drops to zero. Typically, at these places the atom forms more covalent bonds than on the plain surface. Such a place might be a crystal defect, e. g. a threading dislocation, a terrace on the wafer surface due to a certain miscut, or the interface of the Au-Si eutectic droplet. All these places act as nucleation points for crystal growth.

As a result of the surface diffusion, a net flux of particles, $\boldsymbol{I_2}$, from the surface towards the nucleation points, and in this specific case especially towards the interface of the Au-Si eutectic, is obtained. Combined with direct impingement on the droplet, $\boldsymbol{I_1}$, this leads to the total flux of Si atoms $\boldsymbol{I} = \boldsymbol{I_1} + \boldsymbol{I_2}$ which are incorporated into the growing NW. $\boldsymbol{I_2}$ is also the flux that determines the visible length of the NW $\Delta \boldsymbol{l} = \boldsymbol{l_{NW}}\text{-}\boldsymbol{l_{epi}}$ which is the difference of the total length of the NW and the thickness of the epilayer (Scheme 4).

Macroscopically, the material transport is determined by the chemical potentials of the catalyst and the surface. The chemical potential $\boldsymbol{\mu}$ is the change of the free energy $\boldsymbol{G}$ with the number of particles $\boldsymbol{n}$:

$$\mu = \left(\frac{\partial G}{\partial n} \right)_{T,p} . \tag{27}$$

A difference in the chemical potential leads to a particle flux from the area with the higher chemical potential to the area with the lower chemical potential which lowers the free energy of the entire system itself. Because the catalyst droplet has a hemispherical shape, the chemical potential additionally depends on the curvature of the hemisphere. The larger the curvature, the higher the chemical potential compared to the chemical potential at the absence of a curvature $\boldsymbol{\mu_0}$. Thus the difference in the chemical potential is lowered by [123]:

$$\Delta\mu=\mu-\mu_0=\frac{-2\cdot\Sigma\cdot\Omega}{r} \; . \tag{27}$$

$\boldsymbol{r}$ is the curvature radius, $\boldsymbol{\Sigma}$ is the specific surface energy and $\boldsymbol{\Omega}$ represents the specific atomic volume.

This effect is called the *Gibbs-Thomson-Effect* and was referred to by Givargizov and Chernov to explain the difference of the growth rate between thinner and thicker NWs in CVD NW growth [124]. In CVD growth, thinner NWs show a lower growth rate. However, for MBE NW growth the opposite behaviour was observed: Smaller NWs grow faster than larger ones. This is again explained by the surface diffusion because the particle flux towards the catalyst is directly proportional to the diameter of the droplet, and not to the surface area of the droplet. Therefore, the growth rate during MBE NW growth is decreasing with increasing diameter [55].

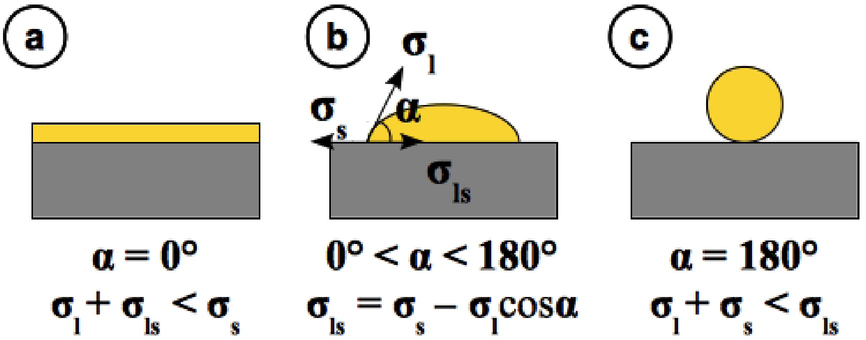

Figure 11: Dependence of the coverage of a surface on the surface tension and the resulting contact angle. a) Total coverage. b) Partial coverage. c) No coverage.

The diameter of the NW depends on the contact area between the catalyst droplet and the substrate. The area on the other hand is determined by the volume of the droplet and the contact angle $\boldsymbol{\alpha}$ (Figure 11). Obviously, NWs do not grow if $\boldsymbol{\alpha}$ = 0° (complete wetting), and if $\boldsymbol{\alpha}$ = 180° (no wetting) because the contact area is either infinite or zero. The contact angle can be calculated using the *Young Equation*

$$\sigma_s=\sigma_{ls}+\sigma_l\cdot\cos\alpha \; , \tag{28}$$

where $\boldsymbol{\sigma_l}$, $\boldsymbol{\sigma_{ls}}$, and $\boldsymbol{\sigma_s}$ are the surface tension of the droplet surface, the liquid-solid interface transition and the Si surface tension, respectively. However, experimental results and theoretical calculations by Schmidt *et al.* have shown, that there are even more restrictions to the contact angle and the surface tension for the successful growth of NWs [125]. Since the surface tension not only depends on the orientation of the substrate, but also on the doping of the wafer, a very high doping level might prevent the formation of NWs.

During Si NW growth there is not only the surface diffusion of Si atoms, but also a diffusion of Au atoms leading to an alteration of the diameter distribution of the catalyst droplets. This alteration of the diameter distribution of the droplets by surface diffusion is known as an effect of *Ostwald ripening* [60,126]. In principle, larger Au-Si droplets grow at the expense of smaller droplets which eventually vanish. The *LSW-Theory* [127,128] can be applied to describe the time-dependent behaviour of the diameter distribution:

$$f(r,t)=\frac{C}{\left(\frac{r'(t)}{r'(t=0)}\right)^{4}}\cdot\left(\frac{r}{r'(t)}\right)^{2}\cdot\left(\frac{3}{3+\left(\frac{r}{r'(t)}\right)}\right)^{\frac{7}{3}}\cdot\left(\frac{\frac{3}{2}}{\frac{3}{2}-\left(\frac{r}{r'(t)}\right)}\right)^{\frac{11}{3}}\cdot\exp\left(\frac{-\left(\frac{r}{r'(t)}\right)}{\frac{3}{2}-\left(\frac{r}{r'(t)}\right)}\right), \qquad (29)$$

C is a constant, ***r'*** is an equilibrium NW radius where the diameter is stable and does not change due to the Au diffusion. Furthermore, the theory gives a minimum NW radius r_{min} and a maximum NW radius r_{max}, which depend on the growth conditions and the growth time [60]. Ostwald ripening also occurs in CVD NW growth, especially at lower growth rates and if the catalyst is deposited as a thin film prior to the experiment [129]. It might be significantly suppressed if colloids are used as a catalyst and at high growth rates.

MBE NWs generally grow in <111> direction, independent of the substrate orientation. The growth velocity ***v*** of a crystal is given by:

$$v\sim d_{hkl}\cdot v_N=d_{hkl}\cdot B\cdot e^{-\frac{-\Delta G_K}{k_B\cdot T}}, \qquad (30)$$

where v_N is the nucleation frequency, ***B*** a frequency factor and ΔG_K the nucleation enthalpy. The probability of growth increases with the energy gained by incorporation of an atom at a specific crystallographic plane [130]. Surfaces with the lowest *displacement velocity* dominate the morphology of the NW [131]. Even if there are planes with a higher displacement velocity at early stages of NW growth, they will eventually vanish with time. For Si, the {111} planes, which are the planes with the highest density of atoms, dominate the crystal growth process. In CVD NW growth <112> and <110> growth directions start to dominate if the diameter of the NWs is below 20 nm [132]. However, MBE grown NWs usually have diameters above 60 nm.

4.2 Experimental Details

The NWs were grown by MBE on (111)-oriented P doped 5” Si wafers (n-type doping) which were cleaned by the conventional RCA I and RCA II procedure before their insertion into the MBE machine. After an annealing process to remove the protective oxide layer, a 200 nm intrinsic Si buffer layer was grown at a substrate temperature $\boldsymbol{\vartheta_S}$ = 550 °C ($\boldsymbol{T}$ ~ 823 K) for better comparability of the experiments (Scheme 7a). Then, an Au thin film with a nominal thickness of 1.5 to 2 nm was deposited at $\boldsymbol{\vartheta_S}$ = 525 °C ($\boldsymbol{T}$ ~ 798 K). The thickness of the film was measured *in situ* with an oscillating quartz crystal. Due to the high temperature of the wafer, an Au-Si eutectic alloy is formed immediately, as well as liquid Au-Si alloy droplets, which will later act as the catalysts for the NW growth (Scheme 7b). This step is immediately followed by a second Si deposition step at $\boldsymbol{\vartheta_S}$ = 525 °C (Scheme 7c). As a standard experiment, the nominal Si film thickness for this period was chosen to be 270 nm, which corresponds to a deposition time of 1.5 hours at a growth rate of 0.05 nm/s. The Ge layers were either deposited interrupting the Si NW growth time (Scheme 7d) or afterwards (Scheme 7e). The gold droplet on top of the NWs as well as the gold decoration at the side walls and on top of the epilayer can be removed, for instance, in a solution containing 20 g KI and 5 g I_2 per 100 ml H_2O (Scheme 7f).

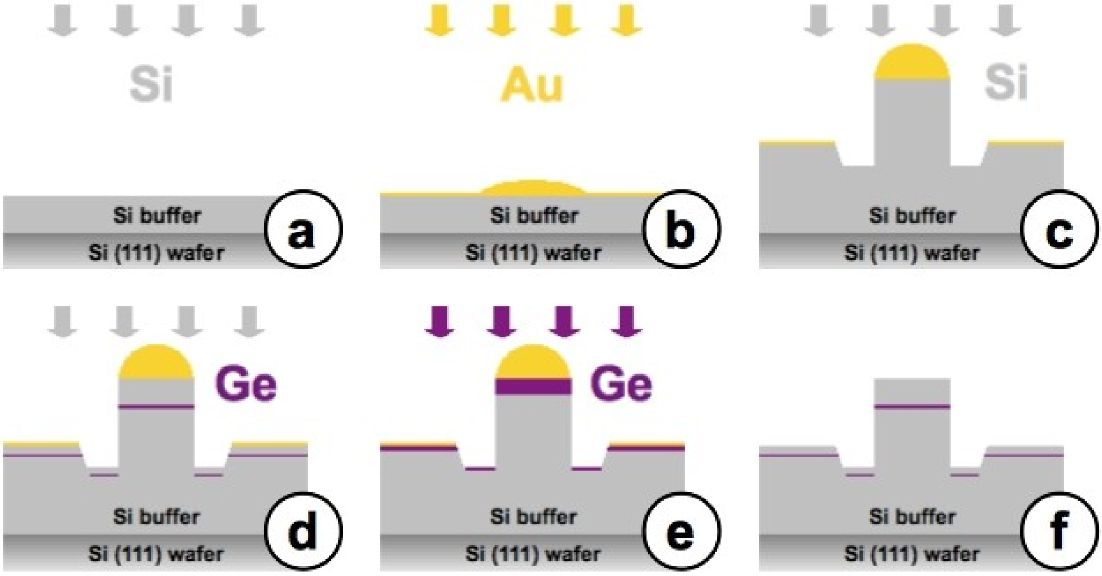

Scheme 7: Schematic diagram of the fabrication process of silicon nanowires and Si/Ge heterostructure nanowires by molecular beam epitaxy. At first a Si buffer layer is grown (a). Then, an Au thin film with a nominal thickness of 1.5 to 2 nm is deposited (b). Liquid Au-Si alloy droplets are formed which will later act as the catalysts for the NW growth. This step is immediately followed by a second Si deposition step (c). Ge layers can be grown either interrupting the Si nanowire growth (d) or afterwards (e). The catalyst can be removed by an appropriate gold etch after the growth process (f).

4.3 Results and Discussion

4.3.1 Nanowire Growth: Position, Dimensions, Crystal Structure and Morphology

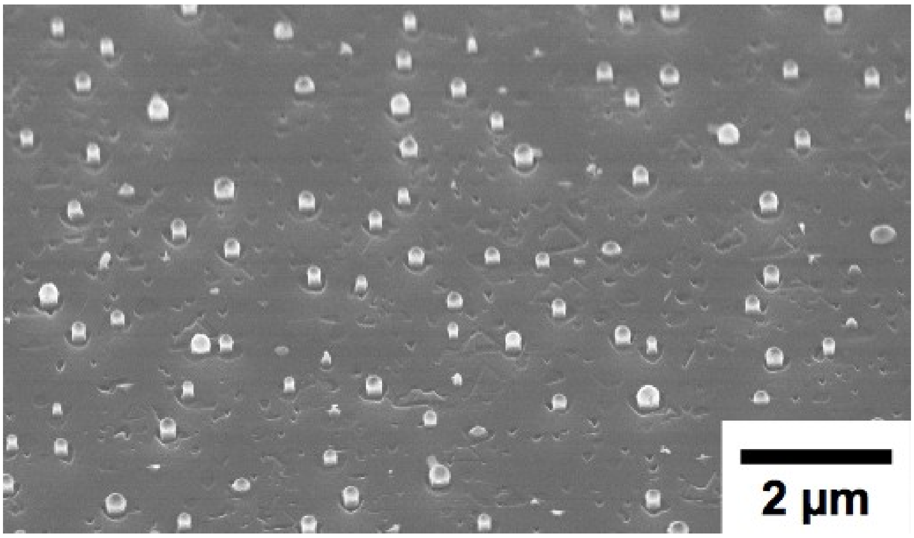

Figure 12: Large area SEM micrograph of a section of a 5" wafer with Si nanowires grown by MBE. (Experiment #070607) The nanowires are randomly distributed throughout the whole wafer. (Sample is tilted by 45°)

<u>Nanowire Positioning and Ordering</u>

Prior to the fabrication of the Si/Ge heterostructure NWs, pure Si NWs were grown as a reference and to determine the NW density and diameter distribution. The NWs were grown by MBE on a 200 nm Si buffer layer for 1.5 hours at a growth rate of 0.05 nm/s (Experiment #070607). The nominal thickness of the Au film was 2 nm. Figure 12 shows a SEM micrograph image of a section of a 5" wafer with VLS Si NWs. They are oriented perpendicular to the wafer surface and are randomly distributed on the whole wafer surface. There is neither a short nor a long range ordering. The NW density is approx. $8 \cdot 10^8$ NW per cm^2, which corresponds to an average centre-to-centre distance of roughly 440 nm (assuming a hexagonal close-packed arrangement). A closer look is offered by Figure 13. The darker spot on top of the NWs is the Au cap.

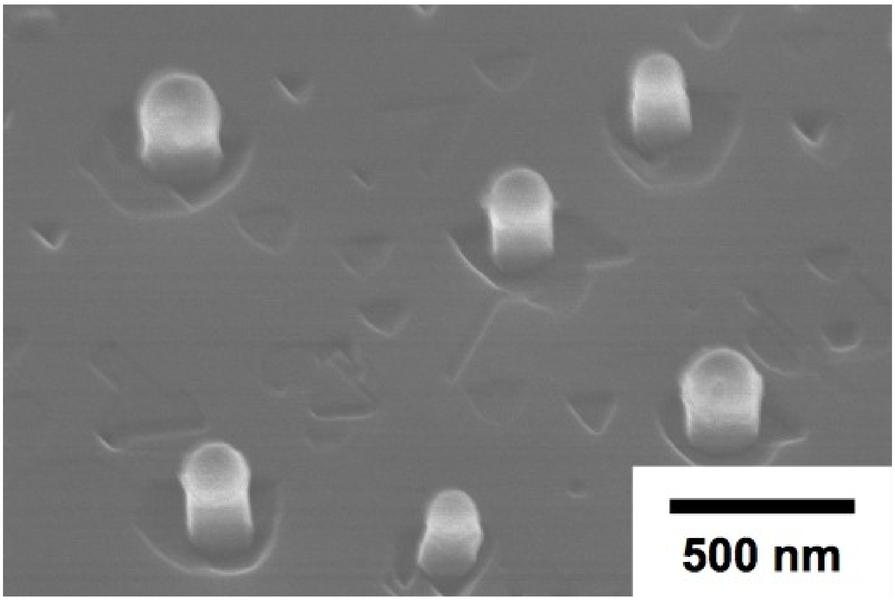

Figure 13: SEM micrograph of a section of a <111> oriented silicon wafer with silicon nanowires. These nanowires grow perpendicular to the surface of the substrate. The darker spots on top of the nanowires are the Au caps. (Sample tilted by 45°)

Nanowire Length and Diameter

If the catalyst is deposited as a thin film, the NW diameters are not fixed. Instead a diameter distribution is given which depends on the growth conditions, e. g. temperature, time, and growth rate. The nominal thickness of the Au film also determines the diameters and the NW density. A maximum of the NW density was found at a thickness of approx. 2 nm at a growth temperature of 525 °C [60]. For the reference sample, the NW diameter distribution which is shown in Figure 14 was obtained. It shows a minimum NW diameter of approx. (100 ± 10) nm and a maximum NW diameter of approx. (260 ± 26) nm. The average value is (184 ± 19) nm with a standard deviation of 33 nm. Although the NW diameter depends on the diameter of the catalyst droplet, it is not fixed during growth because the volume of the droplet might change due to Ostwald ripening, leading to conically shaped NWs.

In CVD, NWs can also be grown catalysed by Au colloids. Since the size distribution of these colloids is rather narrow, the NW diameters can be adjusted more precisely. Furthermore, the absence of a Au-Si wetting layer suppresses Ostwald ripening. However, this approach can not be transferred to MBE NW growth. Experiments with 20 nm diameter Au colloids did not result in NW growth. Instead the catalyst droplets were either completely dissolved or agglomerated to large Au islands (Figure 15). This can be explained by the very low growth rates which do not suppress the Au diffusion from the droplet into the Si substrate, which occurs due to the concentration gradient.

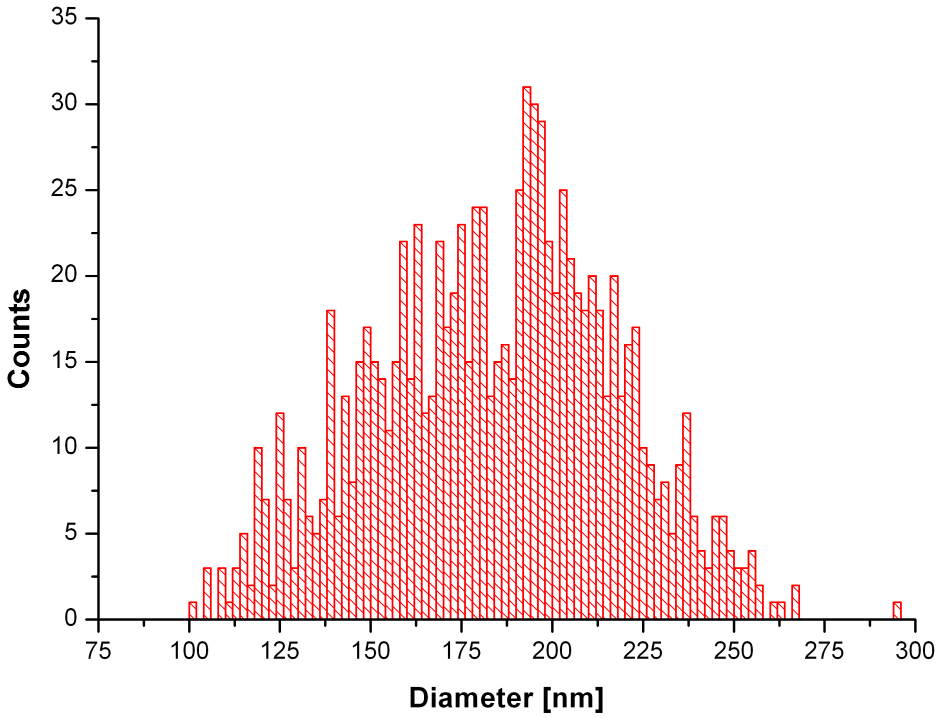

Figure 14: Diameter distribution of sample #070607. Silicon nanowire growth for 1.5 hours at 0.05 nm/s.

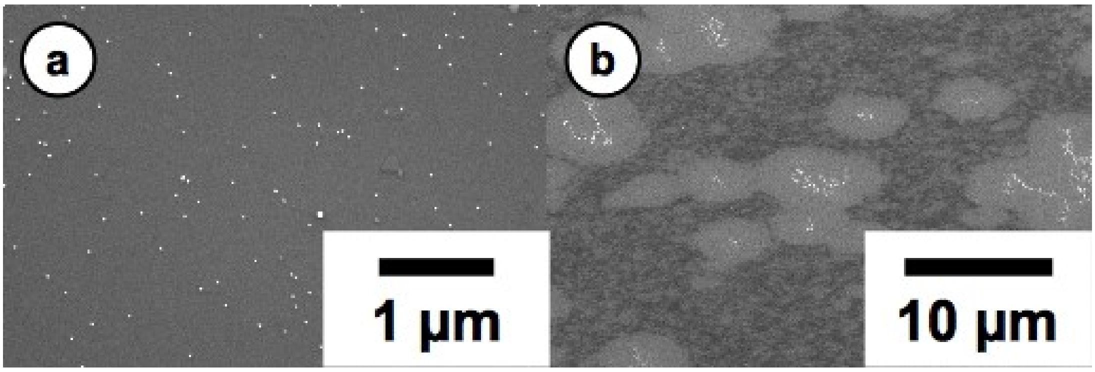

Figure 15: NW growth experiments with Au colloids. a) Au colloids with 20 nm diameter were distributed on the Si surface to act as the catalyst for the nanowire growth. b) However, no growth was observed. The colloids were either dissolved or agglomerated to large Au islands.

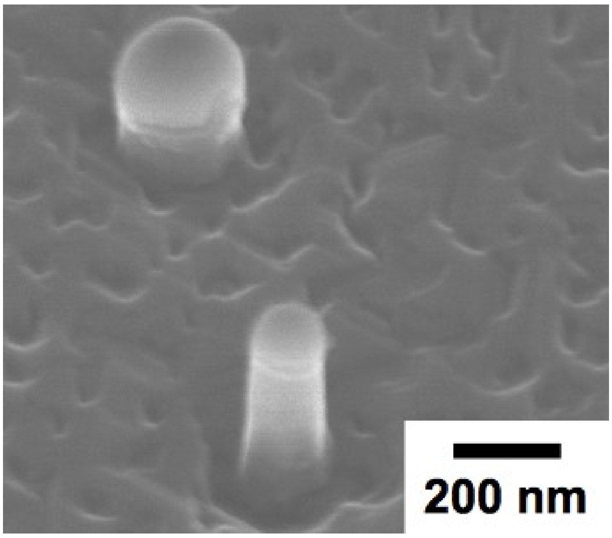

Figure 16: Diameter dependence of the length of Si nanowires. Thinner nanowires are longer after the same growth time. (SEM micrograph)

The diameter of the catalyst droplet not only determines the NW diameter, but, as a secondary effect, also the length of the NW [55]. In contrast to CVD NW growth, the length of the NWs increases the smaller the diameter of the NW (Figure 16). The dependence of the length on the diameter can be described by the equation

$$l(r)=C\cdot\frac{1}{2\cdot r}\ . \tag{31}$$

The change of the volume of a NW with nearly cylindrical shape follows the relation

$$\frac{\partial V}{\partial t}=\pi\cdot r^2\cdot\frac{dl}{dt} \tag{32}$$

with

$$\frac{dl}{dt}\sim\frac{1}{r}\ . \tag{33}$$

The linear dependence on ***t*** indicates a very fast surface diffusion and a limitation of the rate of NW growth only by the rate of incorporation at the interface.

However, this relations are only valid for NW lengths below approx. 600 to 800 nm. Above, the growth saturates and the NWs grow at the same rate as the epilayer. This essentially means that the flux $\boldsymbol{I_2}$ drops to zero, which can be explained if the NW length exceeds the diffusion length of ad-atoms.

Crystal Structure and Morphology

The NWs are single crystalline and grow homoepitaxially on the substrate surface. They are oriented in <111> direction. They are, however, not perfect cylinders but instead have features which become more visible the longer the growth time, which is consistent with the differences in the displacement velocity of different crystal orientations.

Sawtooth faceting in Si NWs was observed both for CVD grown NWs [133] and MBE grown NWs [57,60]. Furthermore, in both cases, the cross-section area of the NWs resembles a trigonal hexagon with {112} planes as the side walls. However, these side wall planes are not "real". A closer look reveals that they consist of an alternating sequence of {111} facets, which is the reason for the "sawtooth shape". The faceting and the pseudo-hexagonal shape of MBE grown Si NWs can be seen in Figure 17.

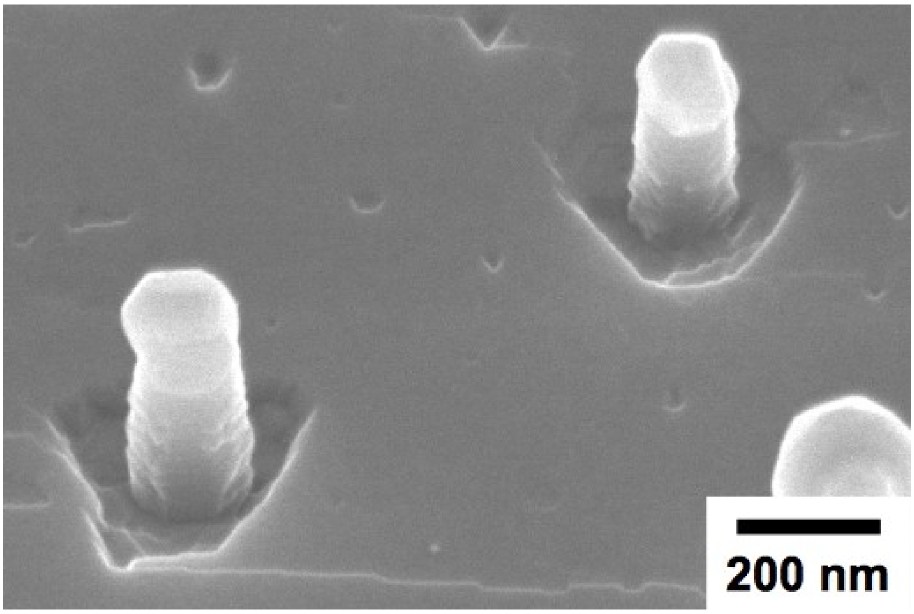

Figure 17: Sawtooth faceting and pseudo-hexagonal shape of Si nanowires. (SEM micrograph)

4.3.2 Heterostructure Growth: Position, Concentrations, Interfaces

A) Incorporation of Thin Germanium Layers

There are two major challenges for the incorporation of thin Ge layers into VLS grown Si NWs. The first one is the exact positioning of the individual layer and the second one is the maximization of the Ge concentration, which goes hand in hand with the task of optimizing the sharpness of the Si/Ge interfaces.

Zakharov *et al.* have already reported on the incorporation of Ge layers in MBE-grown Si NWs [58]. In their experiments, the nominal thickness of the Ge layers varied between 0.5 and 1.5 nm. They observed several phenomena: i) an increase of the Ge concentration with increasing nominal Ge thickness, but at the same time ii) a decrease of the NW growth rate with an increasing amount of Ge within the catalyst droplet, eventually leading to a stop of the growth at all and a dissolution of the NW; iii) a maximum Ge content below 0.2; iv) both a broadening of the layer inside the NW and a decrease of the maximum concentration by a factor of two compared to the corresponding layers in the epilayer structure. The FWHM of the Ge layers in the NWs is approximately ten times larger than the nominally deposited Ge thickness.

It has to be mentioned that the layers were incorporated at the growth temperature of 525 °C, which is far above the Au-Si eutectic temperature and the eutectic temperature for the Au-Ge-Si system. The temperature dependence of these phenomena has not been observed up to now. However, it sounds reasonable to assume a strong dependence of the Ge concentration on the temperature because it influences both the diffusion and the composition of the eutectic droplet.

While MBE-Si NWs grow best at 525 °C [60], growth of Ge NWs was observed at 360 °C which is close to the eutectic point of the Au-Ge system. Combining these results, the Si parts of the following heterostructures were grown at 525 °C. During the incorporation of Ge, the temperature was lowered to 360 °C.

Germanium Concentration and Concentration Profile

Figure 18 shows a representative SEM micrograph of several experiments (#070814a / #070921 / #090102) where 2.5 nm Ge were deposited interrupting the Si NW growth to incorporate a Ge layer into the NWs. However, only very few NWs remained after the Ge deposition step. The majority of the wires had dissolved. This effect of growth suppression due to Ge incorporation has up to now not been reported in the case of CVD Si NW growth.

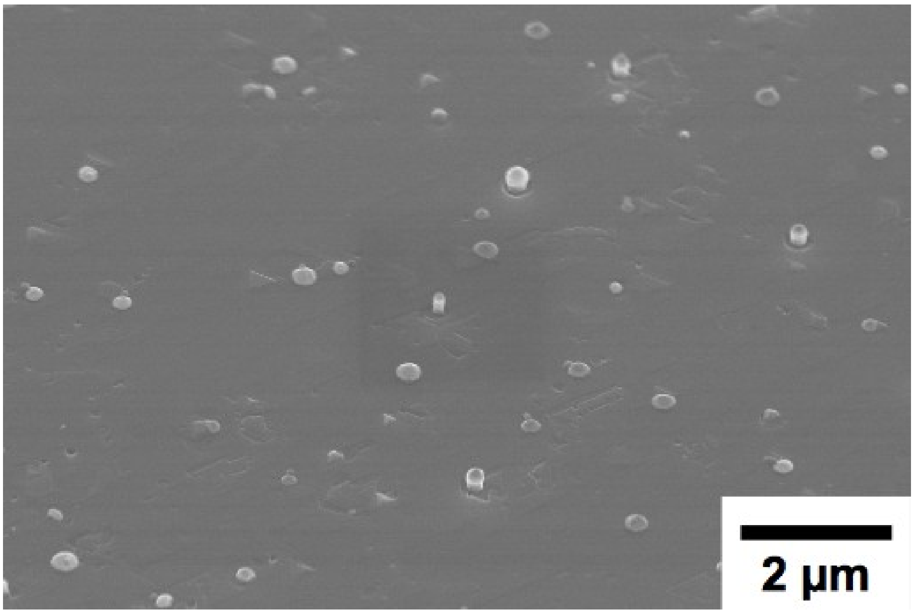

Figure 18: When a Ge layer with 2.5 nm nominal thickness is incorporated into the Si nanowires at 525 °C, most of the nanowires are destroyed. (Experiment #070921)

For the next experiments, before the Ge deposition, the temperature was lowered from 525 °C to 360 °C (Scheme 8). The latter is a common growth temperature for pure Ge NWs on <111>-oriented Ge substrates. During the second Si deposition phase the temperature was increased back to 525 °C. A representative TEM micrograph of a NW obtained after such an experiment can be seen in Figure 19a. For this experiment, the nominal thickness of the Ge layer was 2.5 nm (Experiment #070801). Figure 20 shows the corresponding concentration profile (light grey). Compared to the results reported earlier [55], the temperature reduction led to an increase in the Ge content by approximately a factor of two up to 0.26 ± 0.01. Although the nominal thickness of the Ge layer was increased from 1.5 nm to 2.5 nm, the FWHM could be decreased nearly by a factor of two from ≈ 15 nm to ≈ (8 ± 1) nm. A possible explanation for the increase of the Ge concentration and the decrease of the FWHM might be the reduction of the Si concentration within the eutectic droplet due to the lower temperature.

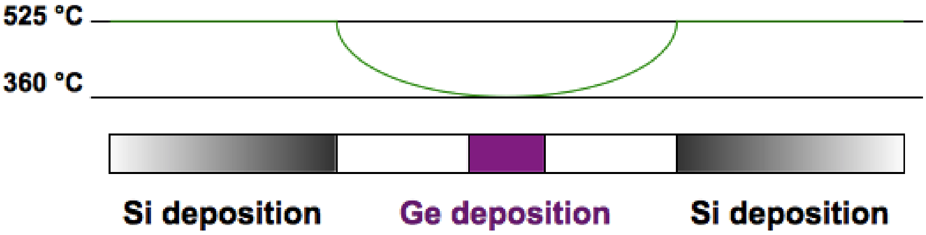

Scheme 8: Illustration of the temperature profile during the Ge layer deposition (green curve).

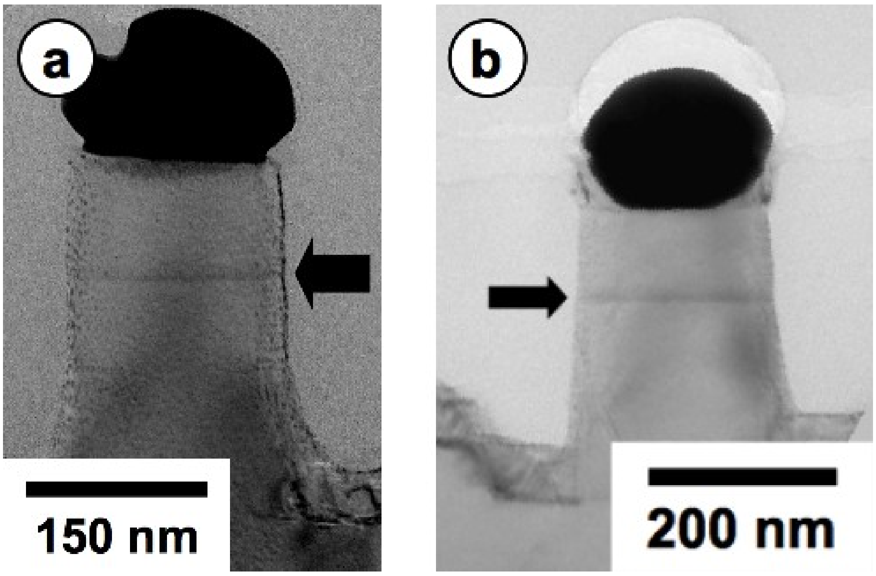

Figure 19: TEM micrographs of Silicon nanowires which contain a Germanium layer inside, roughly in the middle of the visible part (black arrows). The nominal Ge layer thickness was 2.5 nm (a) and 5 nm (b), respectively. (Experiments #070801 and #071017b)

Based on this results, the nominal Ge thickness was increased even further from 2.5 to 5 nm (Experiment #071017b). This led to another jump of the Ge content to a maximum of approx. 0.36 ± 0.01, which is already in the regime of some conventional Si/Ge superlattice heterostructures. However, the peak is fairly wide, with a FWHM of ≈ (12.7 ± 1) nm. But this value is still below the FWHM of the reference value. Thus at the same length scale a much larger amount of Ge was incorporated into the NW due to the temperature reduction. A representative TEM micrograph of a NW can be found in Figure 19b, and Figure 20 again shows the corresponding concentration profile (dark grey). Table 6 gives a final comparison of the experimental parameters of the experiments and the obtained Ge concentrations.

The shape of the profiles itself is in good agreement with the results of Clark *et al.*, who reported on the growth of Si/Ge heterostructure NWs by low pressure CVD using silane and germane precursors [63]. They described the shape of the leading edge with an error function, which was explained by a delay between the modulation times for the vapour and liquid phases caused by the time required to establish a steady-state composition of the catalyst droplet. During this time, a certain amount of Ge must be solved in the droplet, while at the same time excess Si atoms must be precipitated at the interface where they are incorporated in the growing NW. The result is a broadening of the interface. The shape of the trailing edge can be modelled by an exponential decay function.

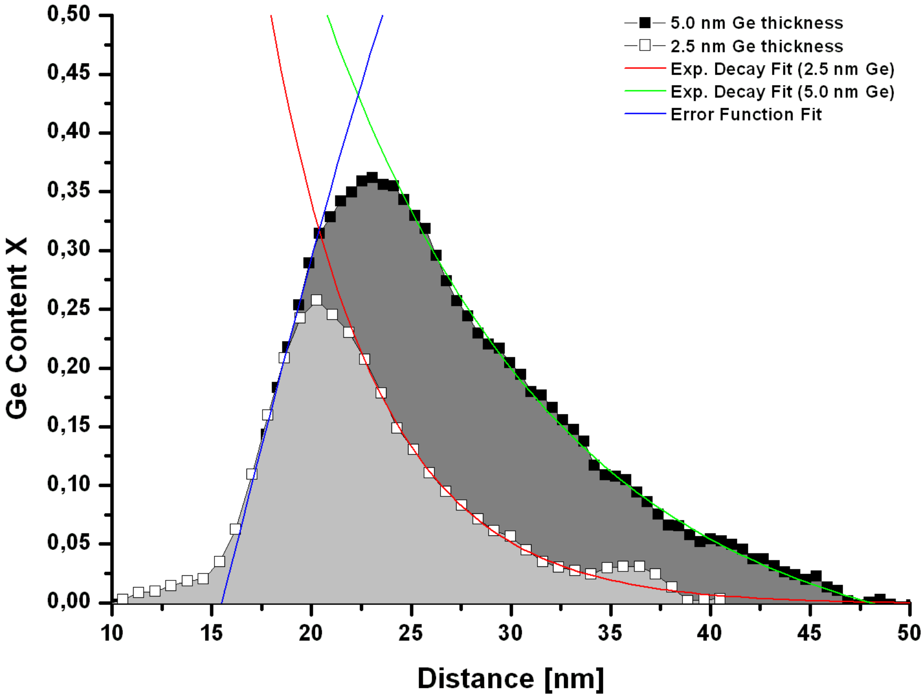

Figure 20: Concentration profiles along the growth direction obtained by TEM. Light gray corresponds to the nanowire in Figure 19a (#070801); dark grey corresponds to the nanowire in Figure 19b (#071017b). The maximum Germanium concentration found was 26 at.-% and 36 at.-%, respectively.

In analogy to the results of Clark *et al.*, the equation to model the trailing edge of the concentration profiles in Figure 20 was of the following form:

$$X(x)=C_1\cdot\exp\left[\frac{-(x+x_0)}{C_2}\right]-C_3\,, \tag{34}$$

where $\boldsymbol{X}$ is the Ge content, $\boldsymbol{x}$ is the distance, $\boldsymbol{x_0}$ an offset and $\boldsymbol{C_1}$, $\boldsymbol{C_2}$ and $\boldsymbol{C_3}$ are fitting parameters. For the leading edge, only a single function was used as a fitting curve for both concentration profiles:

$$X(x)=1\cdot erf\left[\frac{(x-x_0)}{C_1}\right]. \tag{35}$$

In contrast to the experiments of Clark *et al.*, who provided a mixture of GeH_4 and SiH_4 to grow $Si/Si_{1-X}Ge_X$ heterostructure NWs, pure Ge was provided as a source material for the MBE heterostructure NW growth experiments. Because of identical growth parameters except for the nominal thickness, it is proposed that in both cases the Ge content increases until the Ge shutter is closed. At this time the leading edge starts to diverge from the fitting curve. If the shutter hadn't been closed, the Ge content would have continued to increase along the fitting curve. However, it is doubtful whether the concentration would have reached 100 per cent. It is more likely that the NWs would have been destroyed at a critical concentration similar to the experiments described above.

Clark *et al.* also proposed the possibility to produce more abrupt interfaces by reducing the solubility of Ge and Si in the catalyst, e. g. by using another and/or a solid catalyst. The results presented above have shown that a reduction of the growth temperature also increases the Ge concentration and leads to a more abrupt interface as indicated by the reduction of the FWHM.

Experiment	***Reference Sample***	***090102 / 070814a / 070921***	***070801***	***071017b***
Nominal Ge layer thickness	1.5 nm	2.5 nm	2.5 nm	5 nm
Temperature during Ge deposition	525 °C	525°C	360 °C	360 °C
Maximum Ge concentration	10 at.-%	– (Dissolution of NWs)	26 at.-%	36 at.-%
FWHM	15 nm	–	8.1 nm	12.7 nm

Table 6: Overview on results of several experiments to incorporate Ge layers into Si nanowires.

Germanium Layer Position

The presented NWs contain a Ge layer approximately in the middle of the visible part. This can be seen on the TEM micrographs in Figure 19. Since the length of the NW depends on its diameter and therefore on the diameter of the catalyst droplet, an exact positioning of the Ge layer can only be done when the diameter of the NW is adjusted before the growth. But, in any case where the catalyst is deposited as a film, only a diameter distribution is given. Nevertheless, if a medium growth rate of the NW is assumed for the average NW diameter, the position of the Ge layer can be adjusted with a good accuracy. If the NW diameter differs from the average value, at least the ratio of the top and bottom Si part can be adjusted. The total growth rate of the NWs was 0.083 nm/s compared to 0.05 nm/s for the Si epilayer [60]. The Ge layers with a nominal epilayer thickness of 2.5 nm and 5 nm were placed between two deposition steps of 230 nm and 40 nm of Si. Thus the layer should have been 66.4 nm below the Au droplet. The values obtained from the TEM micrographs give a distance of approximately (72 ± 3) nm for the NW in Figure 19a ((160 ± 5) nm diameter) and (80 ± 3) nm for the NW in Figure 19b ((185 ± 6) nm diameter). However, it is difficult to determine the position were the Ge flux was switched off. Therefore these values are only estimations. Nevertheless, the results emphasize the good accuracy of placement of the Ge layer which is in principle possible by MBE NW growth.

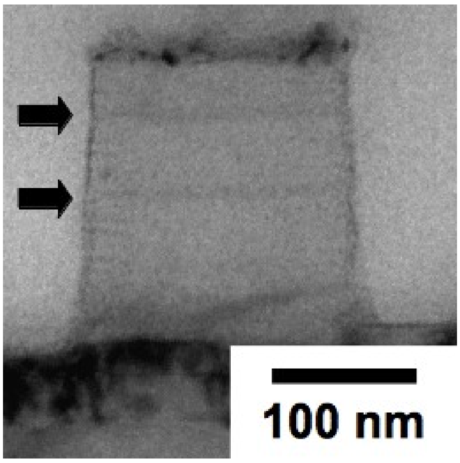

Figure 21: Si nanowire with two Ge-rich layers inside. TEM micrograph. (Experiment #070928)

Figure 21 shows a TEM micrograph of a Si NW with two Ge-rich layers inside (arrows). In this experiment, the Si spacer between the layers had a nominal thickness of 30 nm, and the top Si part had a nominal thickness of 20 nm. (Experiment #070928) Assuming again the medium growth rate of 0.083 nm/s, the distances should be approximately 50 nm and 33 nm, respectively. The values obtained from the TEM micrograph, (52 ± 2) nm and (35 ± 2) nm (≈ (180 ± 6) nm diameter), are in good agreement with the calculated ones and even reflect the ratio of 20 to 30.

In contrast to previous results, a reduction of the NW growth rate due to the incorporation of Ge layers was not observed. This phenomenon might again be connected to the reduction of the temperature. When the temperature is increased during the final Si deposition step, the Ge concentration obviously is too low to influence the supersaturation of the catalyst droplet. In contrast, as it is proposed in [58], at 525 °C much more Ge is solved into the ternary eutectic eventually leading to a reduction of the supersaturation and, finally, a stop of the NW growth.

B) Continued Growth of Germanium Nanowires on Silicon Nanowires

Motivated by the results above, experiments were performed where even larger amounts of Ge were grown on top of Si NWs, eventually leading to the fabrication of Ge NWs on Si NWs. At the same time, the growth temperature was reduced even further when the first results indicated that NWs were again dissolved after the deposition of a certain amount of Ge. Figure 22 shows SEM micrographs of MBE grown Si NWs where 20 nm Ge were deposited afterwards at 325 °C (left image / Experiment #090105) and 300 °C, respectively (right image / Experiment #090106a). A lot of NWs were destroyed in the first case, while all NWs remained intact at the lower temperature.

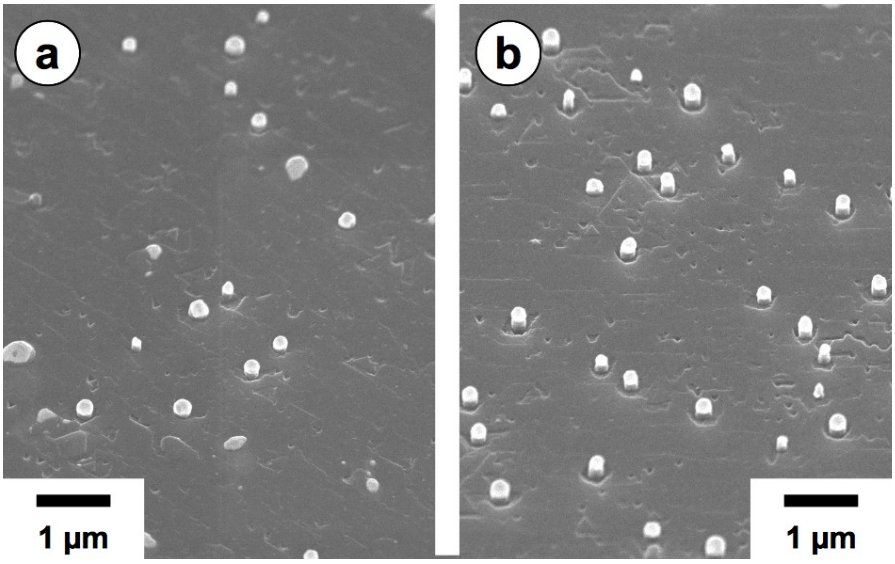

Figure 22: SEM micrographs of samples where we tried to grow Ge nanowires on top of Si nanowires. The Ge was deposited at 325 °C (a) / Experiment #090105) and 300 °C, respectively (b) / Experiment #090106a).

Representative TEM micrographs of two NWs from the second sample (Ge deposition at 300 °C / Experiment #090106a) are shown in Figure 23. The dark black spot on top is the Au catalyst, the middle part is a Ge rich $Si_{1-X}Ge_X$ alloy, and the bottom part is the Si NW. Since *in situ* TEM investigations during MBE growth are not possible at the present time, we can not say if the Au catalyst was solid or liquid during the Ge deposition. Thus we cannot easily compare our results with those published by Kodambaka *et al.* who reported on the growth of pure Ge NWs below the Au-Ge eutectic temperature [46,134].

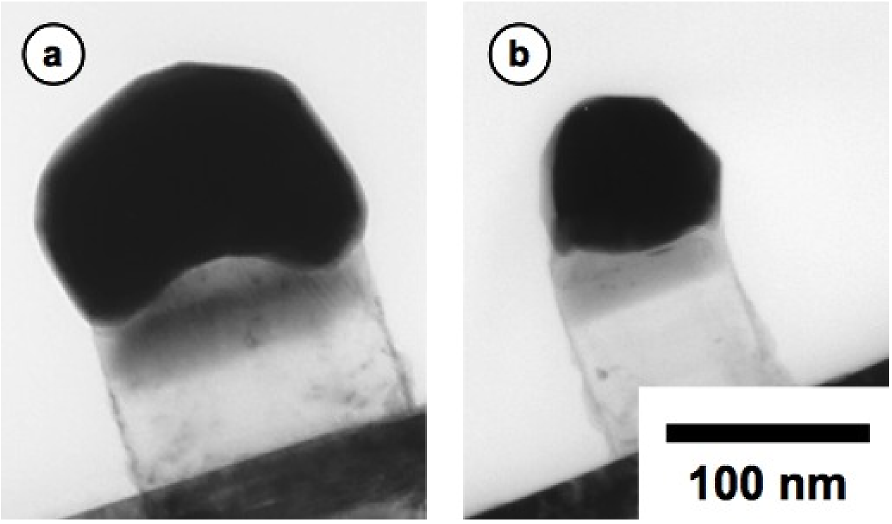

Figure 23: TEM micrographs of two representative Si/Ge nanowire hetero-structures with a Ge part grown on top of a Si part. The dark black spot on top is the Au catalyst, the middle part is a Ge rich $Si_{1-X}Ge_X$ alloy, and the bottom part is the Si nanowire.

However, the growth temperature (300 °C) was below any known eutectic temperature of the ternary Au-Ge-Si system, which is assumed to have a minimum at 327 °C at a composition of 79 at.-% Au, 7.5 at.-% Ge and 13.5 at.-% Si for the bulk material [122]. Since these values were obtained by investigating the cooling curves, they are already at the lower side of the temperature spectrum, indicating that, in the experiments, the Au droplet must have already been solidified during temperature reduction. But the profile of the progression of the Ge concentration along the NW growth axis, which was obtained by TEM from the absorbtion contrast, reveals only a slow increase of the Ge concentration at the beginning (Figure 24). Electron Energy Loss Spectroscopy (EELS) will be performed to quantify the Ge content, however, results are not available up to now.

These results lead to the conclusion that at least a part of the catalyst particle is still liquid and contains a certain amount of Si. Even if the hysteresis of the eutectic temperature is again considered, the growth temperature (300 °C) is significantly lower than the eutectic temperature of the Au-Si system (345 °C for the cooling curve [121]). The cooling time between the Si (525 °C) and the Ge deposition (300 °C) was 10 minutes with an additional 15 minutes for temperature stabilization.

Kodambaka *et al.* also discussed the possibility of the reduction of the point of the liquid-solid phase transition below ϑ_E [46]. For the Au-Ge system, which has an eutectic temperature of 361 °C at a Germanium concentration of 28 at.-%, they estimate from their empirical data that a 1% increase in Ge concentration might reduce the Au nucleation temperature by approximately 40 K. Considering the parameters of the presented experiment (#090106a), this might also explain the experimental results.

The Si NWs were grown at 525 °C, which means that the Si concentration in the Au-Si catalyst droplet exceeded the value at the eutectic temperature by roughly 5 at.-%. Dropping the temperature by more than 200 °C might lead to a rather high supersaturation in the droplet, in turn leading to a delay of the solidification process. This suggests further experiments at lower cooling rates, longer stabilization times, and lower temperatures in order to enhance the Ge concentration and investigate VSS growth phenomena.

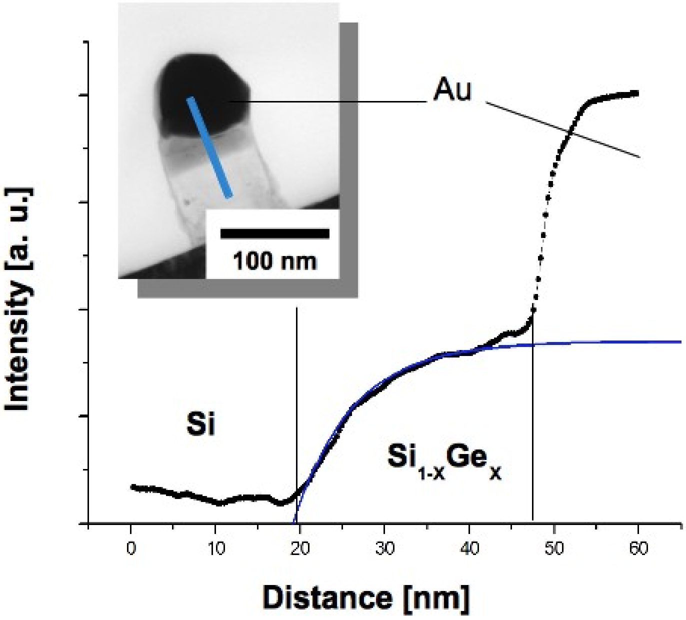

Figure 24: Representative profile of the progression of the Ge concentration along the nanowire growth axis starting a few nm below the interface (at ≈ 20 nm)

4.3.3 Crystal Defects: Point Defects and Dislocations

Dislocations

Neither in the case of Ge layers nor in the case of continued growth of Ge NWs on Si NWs any dislocations were found. Considering only the maximum measured value of the Ge content of 0.36, the critical thickness and the critical radius calculated with (10) and (12) are by far exceeded: For $\boldsymbol{X} = 0.36$ (r = 93 nm), $\boldsymbol{h_C} = 6.3$ nm and $\boldsymbol{r_C} = 26$ nm are obtained. However, the theoretical models only take account of abrupt heterotransitions. In contrast, the experimentally observed transitions showed an almost linear increase and an exponential decrease of the Ge content. Although Kästner *et al.* already mentioned that the strain is significantly lower in NWs with non-abrupt transitions, and thus the critical radius should be much higher [18], a reliable model is still needed to calculate the critical parameters for both layer structures and NWs with non-abrupt heterotransitions.

Gold Contamination

As mentioned above, Au atoms may act as recombination centres in Si. But on the other hand, being a simple eutectic with a low melting point, the Au-Si system is the most common eutectic used as catalyst for VLS NW growth. But if Au is deposited uniformly on the whole wafer not only the Au cap on top of the NW is left after an experiment. Instead the whole surface of the wafer and the NW side walls are covered with tiny Au particles. They are the remnants of the Au-Si wetting layer. Even when Au colloids are used as catalysts, the particles on the side walls are formed.

The solidified Au cap on top of the NWs can be removed quite easily in an ultrasonic bath. If the native SiO_2 layer is formed after a certain time, and the oxide is also formed at the Au/Si interface, the Au cap even falls of without any special treatment because it does no longer stick to the oxide. The gold decoration at the side walls can be removed in an aqueous KI/I_2 solution. The successive removal process is illustrated in Figure 25a-c.

Now the question remains, how much Au is left inside the Si NW which was incorporated during growth. Until recently, there was no possibility to determine the Au concentration inside Si NWs. The first reason was, of course, the size of the NWs which were simply to small for conventional detection methods like, for instance, secondary ion mass spectroscopy or Rutherford-Backscattering. Secondly, the estimated Au concentration is below the detection limit for other analytical methods, e. g. EDX.

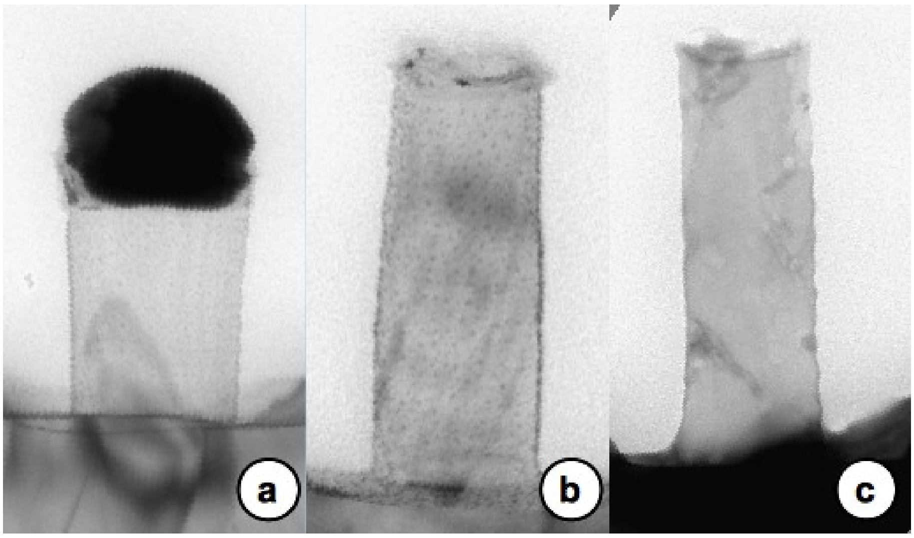

Figure 25: Successive removal of the Au cap and the Au decoration. a) A Si nanowire after growth. b) Another Si nanowire with removed Au cap. c) Also the Au decoration was removed in an aqueous solution containing KI and I_2.

Recent advances in analytical methods like high-angle annular dark-field scanning transmission electron microscopy [135136] and secondary ion mass spectroscopy at the nanoscale [137] enabled the detection of Au atoms within Si NWs. The maximum Au concentration was found to be 1.7×10^{16} cm^{-3} [137] and 5×10^{17} cm^{-3} [135]. These values are the same for MBE and CVD NW growth and are exceeding the expected bulk solubility of Au for the growth temperature [135,136]. However, only very few investigations have been performed so far, and the concentrations might differ depending on the specific growth process and the growth temperatures. For instance, it might be interesting to investigate the Au concentration within Si or Ge NWs grown by the VSS mechanism. In this case the diffusion and the solubility of Au should be drastically reduced.

Although for current Si NWs surface recombination controls the minority carrier transport and the influence of Au can be neglected [135], it has to be mentioned that this might change soon since an effective surface passivation and thus the reduction of surface states is one of many goals necessary for the successful implementation of NWs into devices.

4.4 Summary and Conclusions on the Bottom-Up Approach

Based on previous results reported by Schubert *et al.* [60] and Zakharov *et al.* [58], vertical Si/Ge heterostructure NWs were grown by applying the diffusion-based VLS mechanism to MBE. First, possibilities to increase the Ge concentration in individual Ge layers incorporated into Si NWs were investigated. A reduction of the growth temperature during the Ge deposition resulted in a significant increase of the obtainable Ge concentration. At the same time, the FWHM of the Ge peaks was drastically reduced, increasing the abruptness of the interface. Furthermore, the temperature reduction allowed the incorporation of Ge layers with a higher nominal thickness, which in turn led to another increase of the concentration. The position of the Ge layers could be adjusted with high accuracy. However, although the Ge concentration for the layer could be improved by a reduction of the growth temperature, it remains low compared to conventional heterostructure layer growth by MBE.

Second, experiments were performed to investigate the continuous growth of Ge NWs on Si NWs at even lower temperatures close to and even below the eutectic temperature of the Au-Ge-Si system which is given in literature for the bulk material. However, the concentration profiles indicate that the catalyst droplet was still liquid since high amounts of Si were simultaneously deposited in the NW when the Ge deposition was started. The Ge concentration in the NWs was then constantly increasing.

Based on the results on the incorporation of Ge layers into Si NWs and on the continued growth of Ge NWs on Si NWs, the following conclusions can be drawn: First of all, further experiments are necessary to investigate the influence of the growth temperature on the thermal stability and the maximum achievable Ge concentration. The experiments that were performed have already shown that the growth temperature is one of the most critical parameters. A further reduction of the growth temperature during the Ge deposition in order to further increase the Ge concentration appears promising. In addition, the ternary Au-Ge-Si system requires further investigation, specifically considering the background pressure and the size of the alloy particle to finally determine the temperature values of the phase transitions.

Concerning crystal defects, no dislocations have been found so far in MBE grown NWs. Furthermore, the catalyst particle and the Au decoration on the side walls of the NWs were removed. However, other groups have shown that single catalyst atoms can be incorporated into the crystal lattices of the growing NWs as point defects, independent of the deposition technique.

5 Top-Down Approach

5.1 Nanowire Fabrication by Electron Beam Lithography and Reactive Ion Etching

While crystal growth by molecular beam epitaxy (MBE) has already been illustrated, the fabrication of NWs by electron beam lithography and reactive ion etching needs yet to be explained.

Electron Beam Lithography

The history of electron beam lithography (EBL) began already shortly after the development of the first scanning electron microscopes in the 1960s. The fabrication of 100 nm microstructures was demonstrated as early as in 1965 [138]. Current state-of-the-art systems can produce line widths of 10 nm or even smaller [139].

Working Principle

Similar to optical lithography, EBL is based on the principle that some macromolecular polymers are sensitive to electrons. More precisely, by absorbing the energy of secondary electrons activated by inelastic scattering of the primary electrons with the macromolecules of the polymer, either chain secession (positive resist) or cross linking (negative resist) can occur. Thus the desired pattern can be directly written into the resist and later be transferred to the substrate by etching techniques (Scheme 9). In contrast to optical lithography, a separate photomask is not required.

The set-up of an EBL system is very similar to a scanning electron microscope (Chapter 3.2.1). Actually, various conventional scanning electron microscopes can be upgraded to EBL systems.

Advantages and Disadvantages of Electron Beam Lithography

In optical lithography, the resolution is limited by the optical wavelength. On the contrary, for an acceleration voltage of 30 kV, the wavelength of electrons is already in the range of only several pm. Thus the wavelength of the electrons is not the limiting factor for the ultimate resolution of EBL. In fact, the smallest feature to date with a line width of only 4 nm has been produced by combining EBL with ultrasonically assisted resist development [140]. The resolution, however, is limited by aberrations of the electron optical system and electron scattering effects in both the resist and the substrates. It is therefore rather difficult to produce structures below 20 to 30 nm.

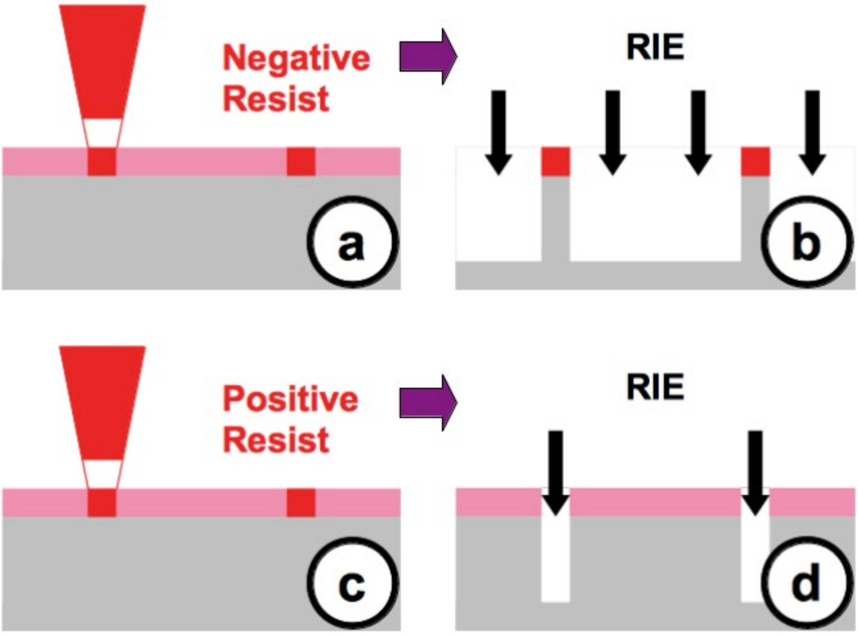

Scheme 9: Comparison of negative e-beam resist and positive e-beam resist and the corresponding structures obtained after the same (fully anisotropic) etching process.

The scattering effects that occur in both resist and substrate can be divided into two categories: forward scattering and backscattering. The former one leads to a statistical broadening of the incident electron beam, while the latter results in reflection of the electrons back into the resist, eventually leading to an unintentional exposure at random positions. Both the ratio of backscattered electrons and the penetration depth of the electrons strongly depend on the initial kinetic energy of the electrons, the density of the target material and its atomic number. For Si the penetration depth may reach several µm. The calculation and visualization of electron scattering trajectories can be done by *Monte Carlo simulations*.

The most prominent consequence of electron scattering in EBL is the *proximity effect*. It refers to an unwanted exposure of adjacent areas of the desired pattern due to an energy transfer by scattered electrons (inter-shape proximity effect). But also within the pattern itself, an energy gradient from the centre to the edges is often observed due to a higher accumulated energy in the centre part (intra-shape proximity effect). The proximity effect can be at least partially compensated by dose correction, pattern adjustments or background exposure compensation.

The major drawback concerning the application of EBL in mass production is its low throughput. Depending on the pattern design and density, it might take hours or even days to expose an area of only 1 cm^2, not to mention a whole 12” wafer. This is several million times slower than conventional optical lithography.

Reactive Ion Etching

As a dry etching process, reactive ion etching (RIE) does not involve any wet chemical etching solutions like, for instance, a mixture of HF and H_2O_2. Instead it relies on physical and chemical processes taking place in a plasma discharge which is generated at low pressures by an electromagnetic field [141].

Working Principle

Chemically active gaseous ions generated by a gas discharge are accelerated towards the substrate surface where they react with the material. Additionally, physical sputtering occurs due to the ion bombardment. This combination removes layer by layer from the surface until the desired etch depth is reached. The simplest RIE set-up is a planar diode electron system with the sample being placed on the cathode. While the anode and the reaction chamber are grounded, the cathode is connected to a radio frequency (RF) power source. Parameters influencing the etch process include the composition of the gas, the gas flow, the chamber pressure, the substrate temperature and the RF power [142].

Advantages and Disadvantages of Reactive Ion Etching

Many (although certainly not all) chemical etching processes are isotropic (Scheme 10a). This also applies to the chemical reactions in RIE. However, for most applications a fully anisotropic etching is required (Scheme 10b). The physical sputtering is more anisotropic but it is not selective. Therefore, enhancing the sputtering component might eventually destroy the mask. With the mask destroyed the surface will be etched homogeneously. Thus both the maximum etch depth and the shape of the structures are determined by the etching selectivity and the etching anisotropy, especially the ratio of lateral etching to vertical etching. This also means that it is more difficult to obtain nanostructures with cylindrical and smooth surfaces than the reduction of their minimum diameter at the cost of a concave shaped surface. For the fabrication of NWs by highly anisotropic etching, the process parameters must be carefully balanced. Even then, lateral etching can never be completely excluded and increases with etch depth.

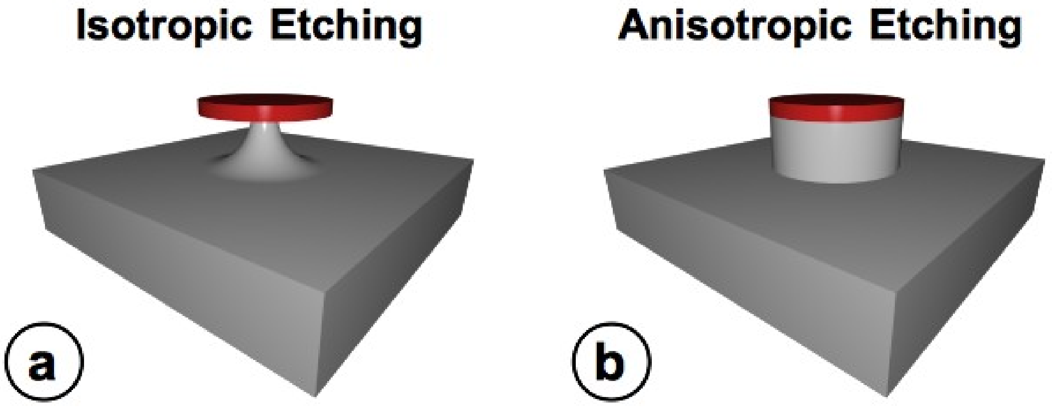

Scheme 10: Comparison of isotropic (a) and anisotropic etching (b). In principle, chemical etching processes are isotropic. However, anisotropic etching is often required for applications. (RED: Mask / GREY: Substrate)

5.2 Experimental Details

For the top-down approach the growth of a Si/Ge superlattice by MBE was combined with mask fabrication by EBL and a RIE step to fabricate ordered arrays of vertical Si/Ge heterostructure NWs. Like the VLS NWs described above, the Si/Ge superlattices were grown in a Riber SIVA 45 MBE machine on 5” P doped Si wafers (Scheme 11a). Again, a 200 nm Si buffer was deposited first, followed by alternating sequences of Si and Ge layers. The growth rate for Si was fixed at 0.05 nm/s. The growth rate for Ge varied between 0.02 nm/s and 0.01 nm/s for different experiments. At the end, a 20 nm Si capping layer was put on top to protect the superlattice. To prevent the formation of Ge islands, the samples were doped with Sb during growth, which acts as a surfactant. Due to the segregation of Sb, the doping concentration varied from approx. 10^{16} cm^{-3} at the bottom of the superlattice to approx. 10^{18} cm^{-3} at the top as measured with secondary ion mass spectrometry on a reference sample.

After the MBE deposition the wafer was cut into 1 cm x 1 cm pieces. These pieces were then used for EBL and RIE individually at different parameters. Before the EBL procedure, the individual specimen was again cleaned chemically. Then, a 30 nm adhesive layer was put on top of the sample by spin-coating, followed by an e-beam resist thin film (negative resist) with a thickness of 50 nm (AR-N 7500.046 / Allresist GmbH). Afterwards the sample was loaded into the EBL machine and exposed to a 40 kV electron beam at defined positions with varying doses between 1000 $\mu C/cm^2$ and 1650 $\mu C/cm^2$ (Scheme 11b). To minimize the proximity effect, the distances between the structures were rather large. The nominal NW diameter was varied between 40 nm and 80 nm. The overall size of the exposed field was 100 µm x 100 µm.

Low-temperature dry etching was applied next to fabricate ordered arrays of Si/Ge heterostructure NWs (Scheme 11c). RIE processes in a SF_6/O_2 plasma (RF power 40 W, $p = 5 \times 10^{-6}$ bar) at a substrate temperature of $\vartheta = -110$ °C were used resulting in etch rates in the order of 80 nm/min. The homogeneous etching of the Si and Ge multilayers was controlled by the SF_6/O_2 ratio and pressure. At the end, the photoresist was removed (Scheme 11d).

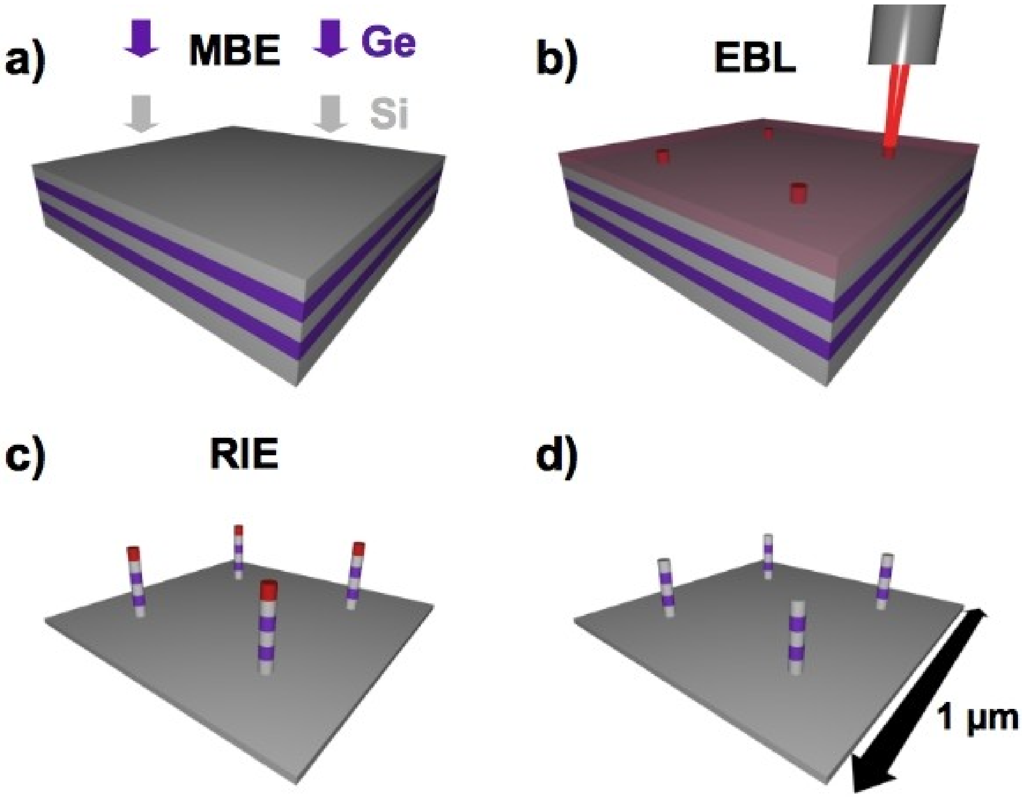

Scheme 11: Schematic diagram of the fabrication process of Si/Ge heterostructure nanowires by molecular beam epitaxy, electron beam lithography and reactive ion etching. At first, the Si/Ge superlattice is grown by molecular beam epitaxy (a). Then, a photoresist is placed on the sample and exposed to an electron beam at defined positions (b). Afterwards, the prepared sample is exposed to a reactive plasma (c). At the end, the remaining photoresist is removed (d).

5.3 Results and Discussion

5.3.1 Heterostructure Growth: Position, Concentrations, Interfaces

In the top-down approach the length of the NW and thus the position of the Ge layers is determined by the etching rate and etch time in the RIE process, and by the structure of the Si/Ge superlattice grown by MBE. The superlattice heterostructures were deposited on (111)- and (100)-oriented Si wafers. In Figure 26 a TEM cross-section micrograph of a superlattice is compared with a scheme based on the nominal growth rates and the deposition time. This superlattice was grown at ϑ_S = 550 °C on a (100)-oriented 5” Si wafer. It consists of 30 periods of an alternating sequence of 0.57 nm (≈ 4 ML) Ge and 1.35 nm (≈ 10 ML) Si. Thus the thickness of a Si/Ge period amounts to 1.92 nm and the total thickness of the superlattice structure amounts to 57.6 nm. The growth rates for Si and Ge were 0.05 nm/s and 0.01 nm/s, respectively.

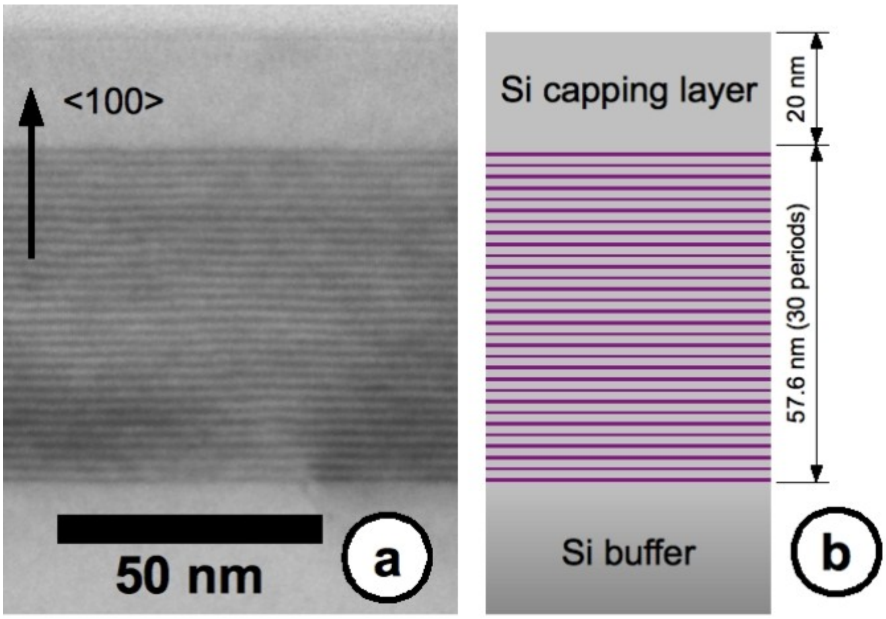

Figure 26: Comparison of a TEM cross-section image of a Si/Ge superlattice grown on a (100)-oriented 5" Si wafer (a) with the calculated model (b)

The comparison shows the excellent growth control for Si and Ge layers which is possible by MBE and has up to now not been achieved by any other deposition method. The Si (bright) and Ge (dark) layers can be clearly distinguished. A concentration profile of a part of the superlattice was obtained by TEM bright field imaging. The TEM cross-section micrograph and the corresponding concentration profile are shown in Figure 27 and Figure 28, respectively.

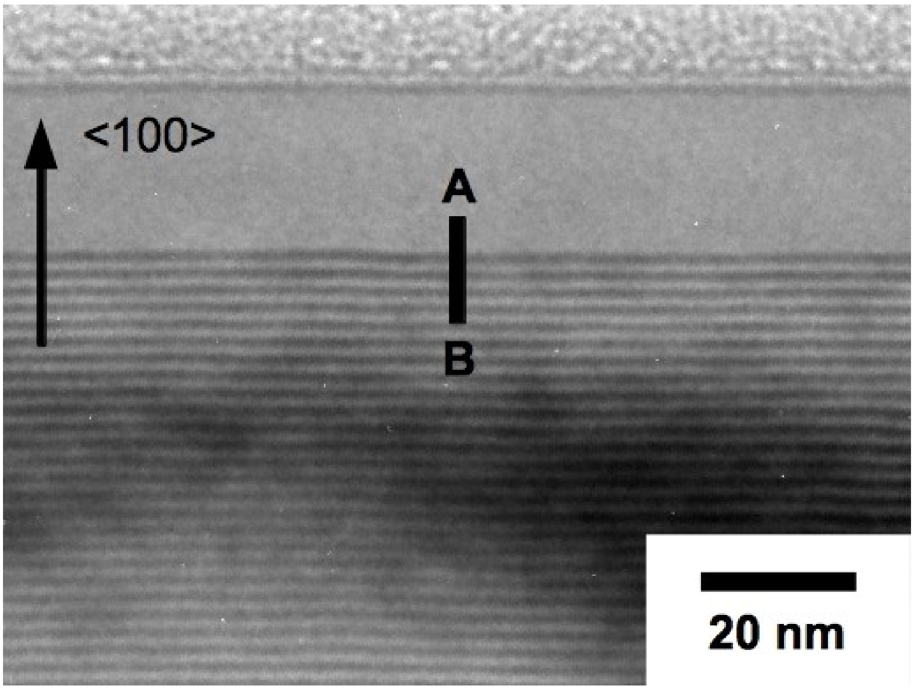

Figure 27: Section of the Si/Ge superlattice #081020 grown on a <100>-oriented Si wafer (TEM micrograph). The line A → B indicates the position where the concentration profile (Figure 28) was obtained.

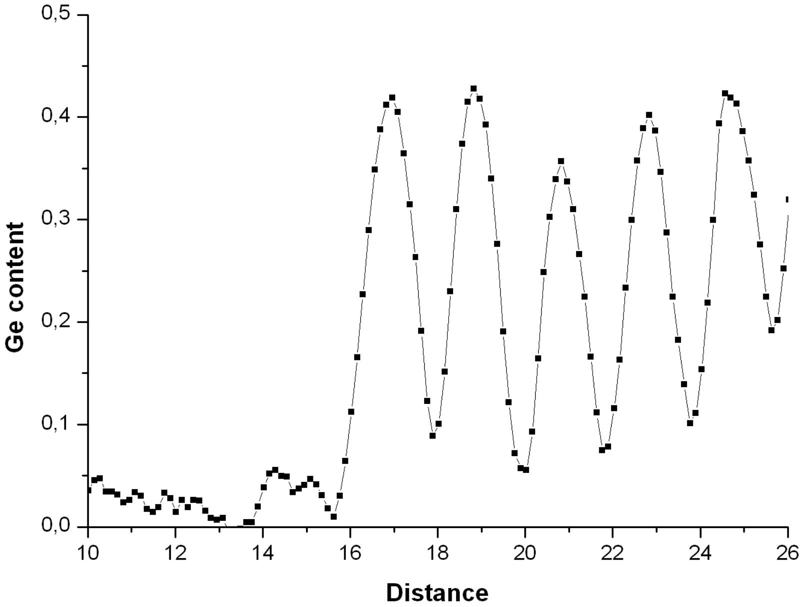

Figure 28: Concentration profile of a section of the Si/Ge superlattice structure #081020 obtained by TEM bright field imaging. The Germanium content X in the $Si_{1-X}Ge_X$ *alloy varies between 0.35 and 0.45. The average peak distance was normalized to 1.92 nm in order to obtain the appropriate Germanium content.*

The maximum Ge content is roughly 0.4 with an average FWHM of 0.9 nm. Compared to the nominal Ge layer thickness of 0.57 nm at an intended Ge content of $\boldsymbol{X} = 1$, theses values emphasize the difficulty of heteroepitaxial growth of Ge on Si, especially the Ge segregation due to the differences in the surface energy, as already mentioned above. However, the profile also shows that the Ge content is reduced below 0.1 within only a couple of monolayers. Therefore, the fabrication of heterostructures with multiple $Si_{1-X}Ge_X$ quantum wells is possible.

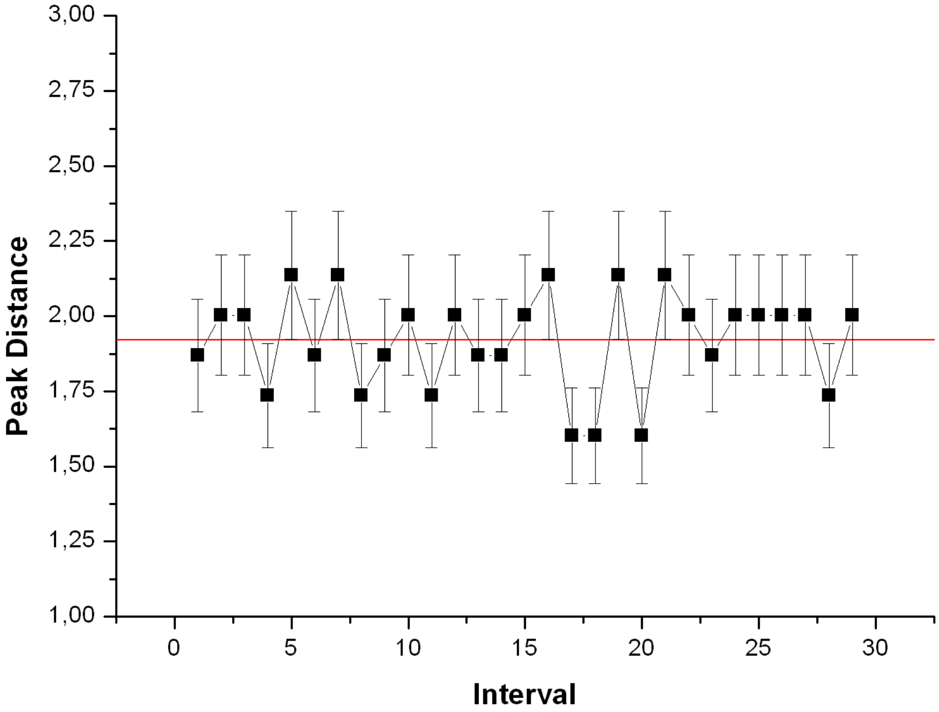

Figure 29: Germanium peak distance (normalized to 1.92 nm (red line)) plotted versus the index of the Germanium layer interval.

Figure 29 shows the distances of the individual Ge peaks. Their average value is already normalized to 1.92 nm (red line) for the future measurement of the Ge concentration. The standard deviation is 0.16 nm, while the minimum value is at 1.6 nm and the maximum at 2.1 nm. The deviations occur due to the instability of the particle flux generated by the electron beam evaporators.

5.3.2 Etching of Nanowires: Position, Dimensions, Crystal Structure and Morphology

Nanowire Position and Dimensions

First etching experiments were performed on Si/Ge superlattice structures grown on <111>-oriented Si wafers (#080819a). A representative SEM micrograph of the resulting nanostructures can be seen in Figure 30. The resist is still on top of the NWs. The centre-to-centre distance is 240 nm, leading to a NW density of approximately $1.7 \cdot 10^9$ NWs per cm^2. The image already shows that the etching process is not fully anisotropic, resulting in a concave shape of the NWs.

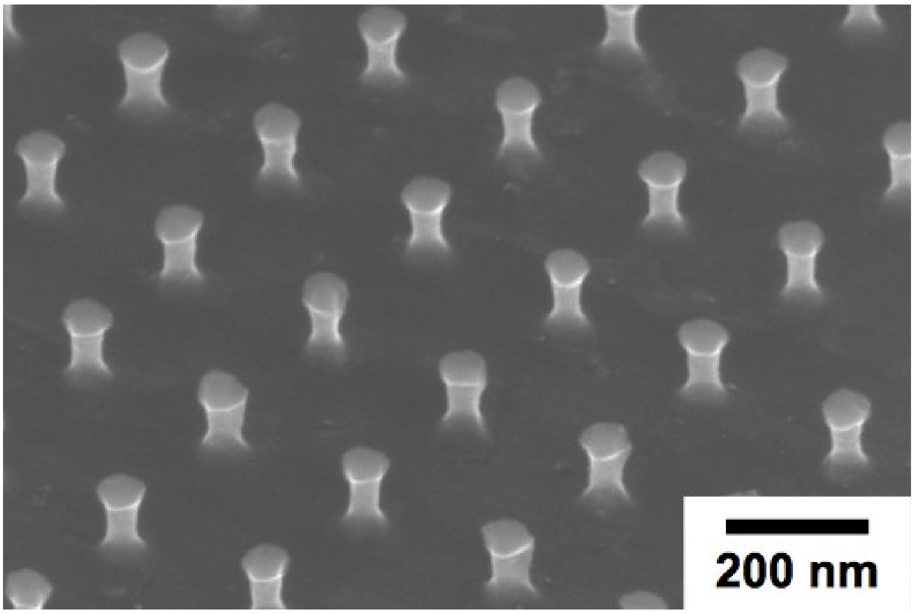

Figure 30: SEM micrograph of a section of a nanowire array etched into a Si/Ge superlattice. The nanowires and the substrate are aligned in <111> direction. (#L1300)

A diameter distribution is given in Figure 31. However, the diameters only refer to the area directly below the resist. Due to shadowing effects a distribution of the diameters at lower positions could not be obtained. Figure 30 indicates that the diameter in the middle of the NWs might be significantly smaller due to an increased lateral etching. The intended cross-section of the NWs was 40 x 40 nm^2 corresponding to a diagonal of approximately 56 nm. The average diameter is ≈ (59 ± 6) nm with a standard deviation of ≈ 3 nm. Therefore it can be concluded that the exposure dose was a little bit too high at the edges of the structure. The distribution of the diameter itself can be explained by intra-shape proximity effects and random exposure of adjacent areas.

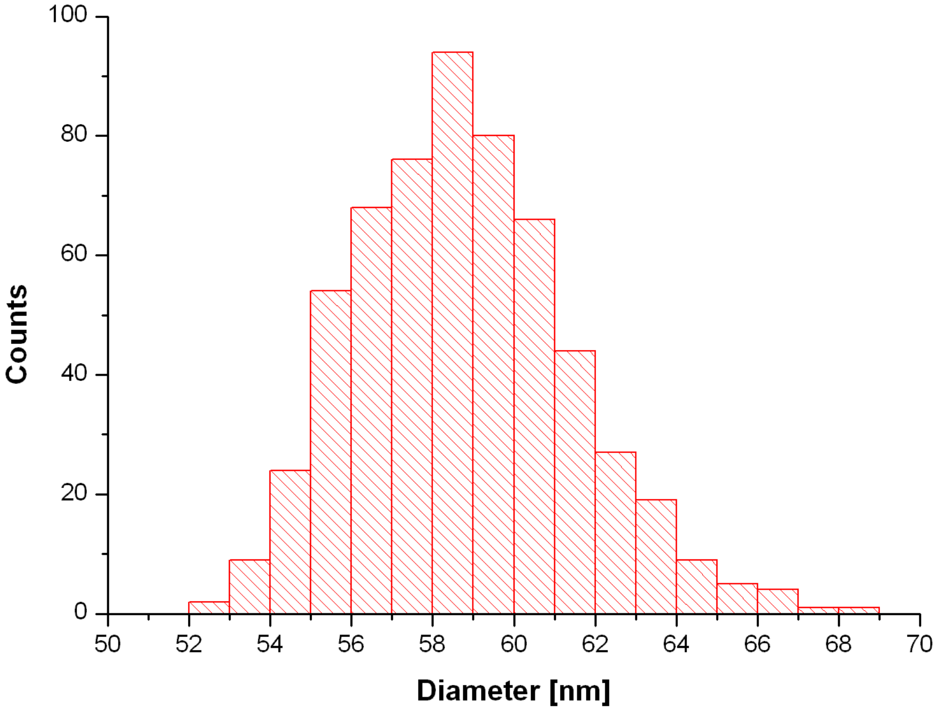

Figure 31: Diameter distribution of a section of experiment #L1300. The diameter refers to the cross-section area directly below the resist. The minimum diameter is even lower.

Since <100>-oriented substrates are preferred for most applications, the etching process was transferred to such wafers as soon as <100>-oriented Si/Ge superlattices were available. The quadratic arrangement and the size of the NW structures was kept but the distance between the individual NWs was increased to 500 nm to minimize inter-shape proximity effects. A part of such a NW array (#L1308) etched into the superlattice #081020 can be seen in Figure 32. The SEM micrograph (tilt angle 52°) shows the quadratic arrangement of the NWs and also the constant distance of 500 nm. The NW diameter varies between (27 ± 3) nm and (43 ± 5) nm. Again it can be seen that there is a certain underetching because the shape of the NWs reminds of mushrooms. Due to the increase of the distance, the NW density dropped to approximately $3.4 \cdot 10^8$ NWs per cm^2 (Table 7).

Experiment-#	*Orientation*	*Structure Size*	*Distance*	*Nanowire Density*
L1300	<111>	40 x 40 nm^2	200 nm	$1.9 \cdot 10^9$
L1302D	<100>	40 x 40 nm^2	500 nm	$3.4 \cdot 10^8$
L1308	<100>	40 x 40 nm^2	500 nm	$3.4 \cdot 10^8$

Table 7: Selected parameters and resulting NW densities for different experiments.

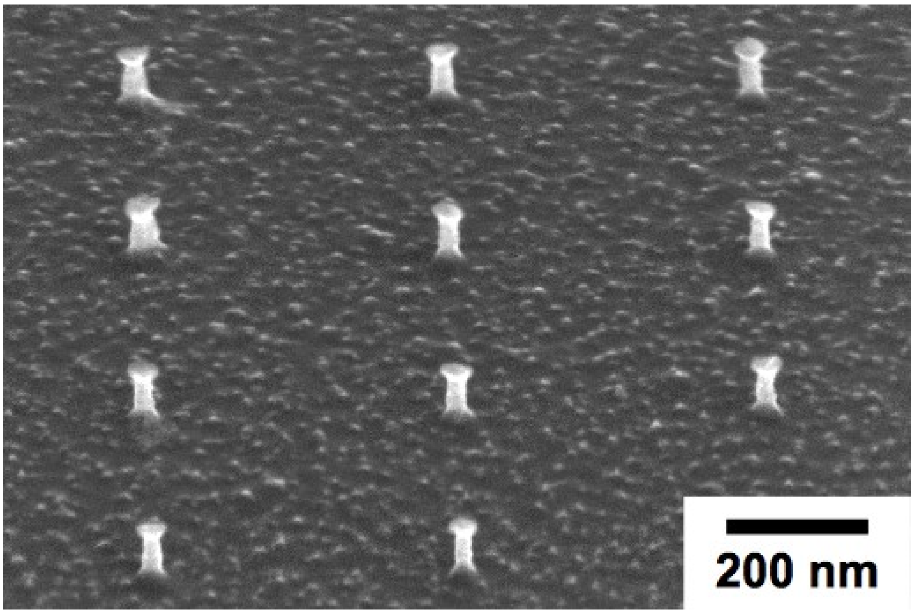

Figure 32: Section of a nanowire array etched into a Si/Ge superlattice structure. The nanowires and the substrate are aligned in <100> direction. (#L1308)

A large area SEM micrograph of another Si/Ge heterostructure NW array (#L1302) is shown in Figure 33. The minimum diameter of these NWs is 15 nm which was achieved by an increased lateral etching. The actual size of the entire field is 100 x 100 µm^2. Over the whole area the NWs are arranged as homogenous as in the section of this field, showing the precise control of the position and arrangement of the NWs which is possible by EBL.

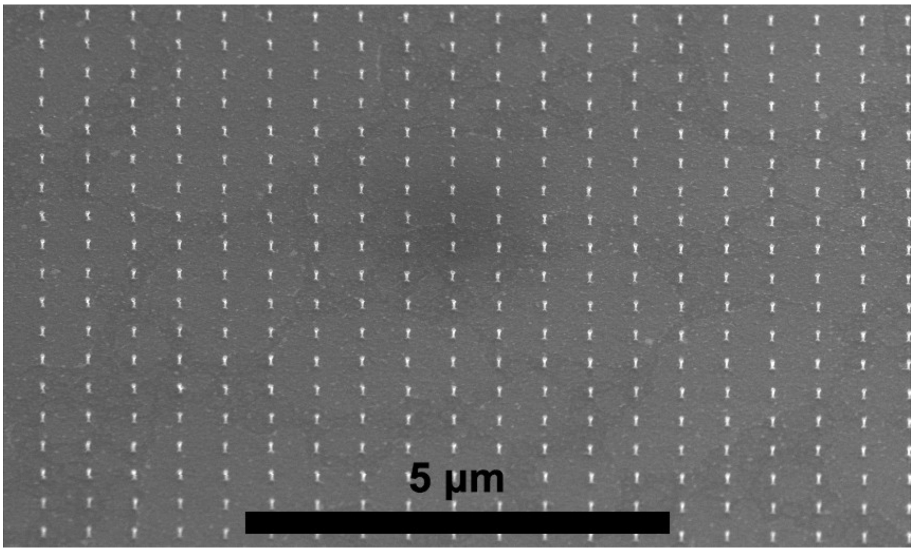

Figure 33: Large area SEM micrograph of Si/Ge heterostructure NWs with d = 15 nm arranged in a quadratic pattern with a = 540 nm (L1302D)

For the top-down approach the length of the NWs is determined by the etch time ***t***. This is demonstrated in Figure 34 where the results of the experiments L1329 (a) and L1323 (b) are shown. The NWs were etched for 70 s (L1329) and 100 s (L1323), respectively, resulting in lengths of ≈ (100 ± 10) nm and ≈ (170 ± 17) nm. The difference in the corresponding overall etch rates (85 nm/min and 100 nm/min) can be explained by the difference of the NW composition: The upper part contains the Si/Ge superlattice; below the superlattice the etching process is only applied to pure Si. For the lower, pure Si part the etch rate can be extracted from the values above as 70 nm / 30 s = 140 nm/min. In both cases the resist was still on top of the NWs when the SEM micrographs were taken.

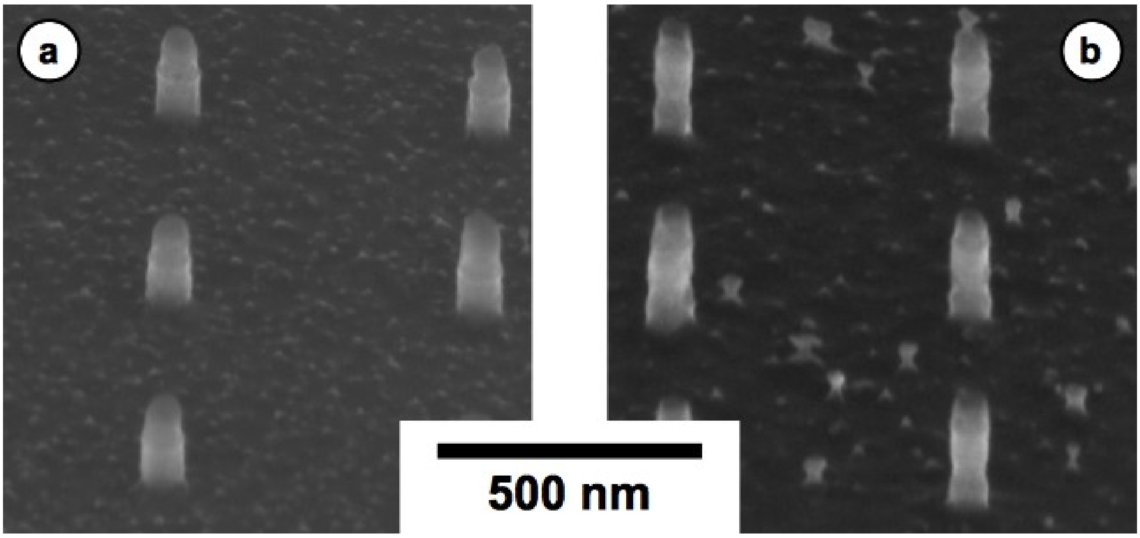

Figure 34: Comparison of NWs obtained after different etch times. a) t = 70 s (L1329). b) t = 100 s (L1323).

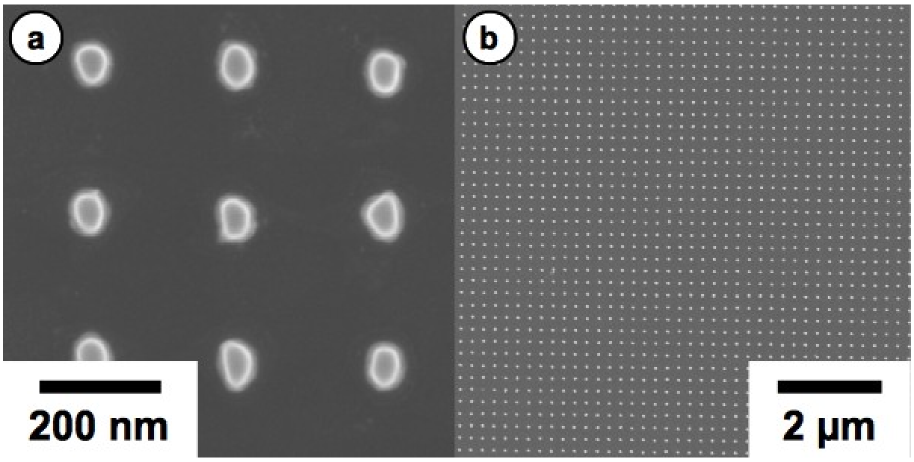

Figure 35: Top view SEM micrographs of a section of a nanowire array. (#L1300)

Crystal Structure and Morphology

All the NWs are single-crystalline and, depending on the underlying substrate, either aligned in <111> or <100> direction, i. e. their orientation is always perpendicular to the substrate surface. Their shape, however, depends on the isotropy and selectivity of the etching process, and is influenced by the proximity effect. The latter leads to an irregular cross-section which is illustrated in Figure 35a, where a top view on the NW array #L1300 is shown. Figure 35b shows the same NW array on a larger scale.

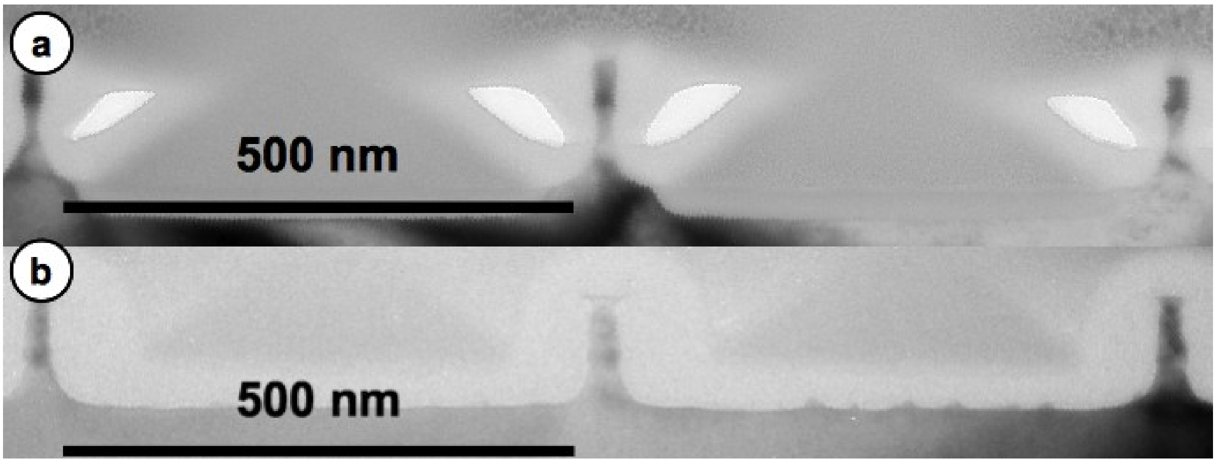

Figure 36: TEM cross-section samples prepared by focussed ion beam technique. The distance between the nanowires is 500 nm. The intended diameter was 40 nm. a) Due to underetching, the nanowire diameter is 15 nm at the thinnest position (L1302D). b) The nanowire diameter varies between 30 to 40 nm (L1308).

The possible influence of the etching process on the shape and curvature of the side walls is illustrated in Figure 36. In the upper part (#L1302D), the lateral etching is not only stronger, resulting in smaller diameters, but also more selective to the silicon etching, resulting in a concave shape below the superlattice. As mentioned above, it is extremely challenging to achieve a fully anisotropic etching.

Finally, Figure 37 shows a HR-TEM micrograph of the upper part of a NW of the experiment #L1308. This verifies the existence and integrity of the superlattice in the NW. The Ge (dark lines) and Si layers can be clearly distinguished. Another NW with a Si/Ge superlattice can be seen on the TEM micrograph in Figure 38. This time the lateral etching was suppressed due to an increase of the oxygen flow. As a result the shape of the NW is more cylindrical. Nevertheless it can still be seen that the etching process is more selective to the Si segments of the NW.

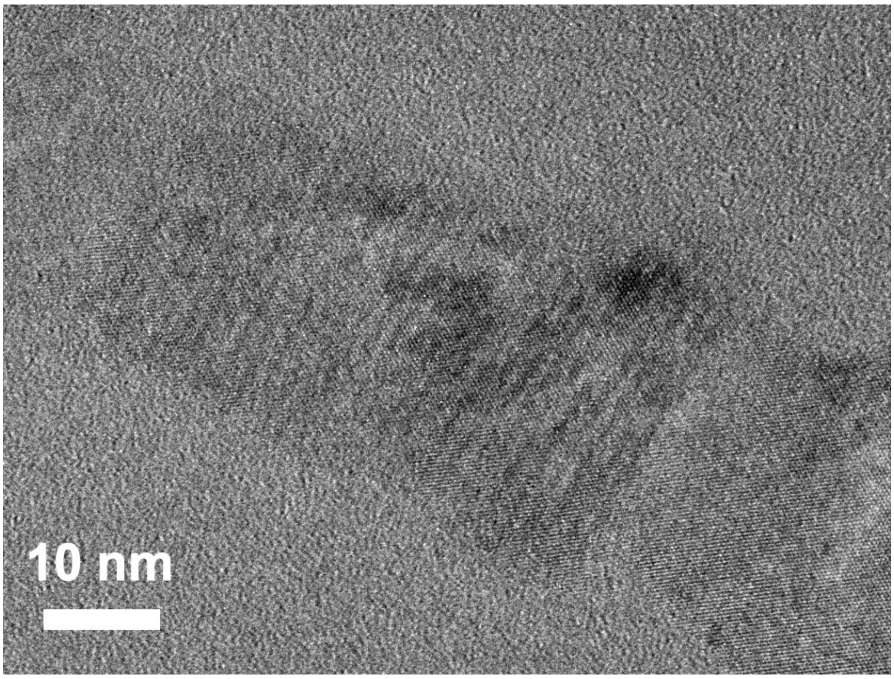

Figure 37: Cross-section HR-TEM micrograph of a 35 nm diameter nanowire with a Si/Ge superlattice inside. The Ge (dark lines) and Si parts can be clearly distinguished. (L1308)

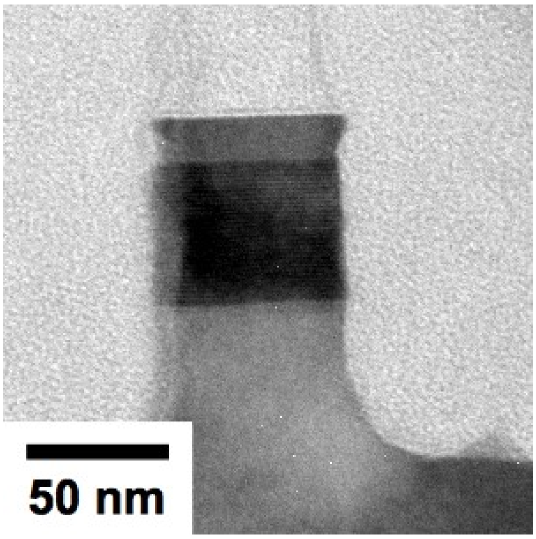

Figure 38: Cross-section HR-TEM micrograph of a 60 nm diameter nanowire with a Si/Ge superlattice inside. (L1329)

5.3.3 Crystal Defects: Point Defects and Dislocations

In contrast to the majority of the bottom-up approaches and also top-down approaches based on metal-assisted etching techniques, no metal is involved in the MBE/EBL/RIE process. Furthermore, each of the individual steps is done at least under high vacuum conditions. Thus the inclusion of metal atoms as point defects into the NWs can be practically excluded. Therefore this chapter focusses solely on the possibility of misfit dislocations within the etched NWs.

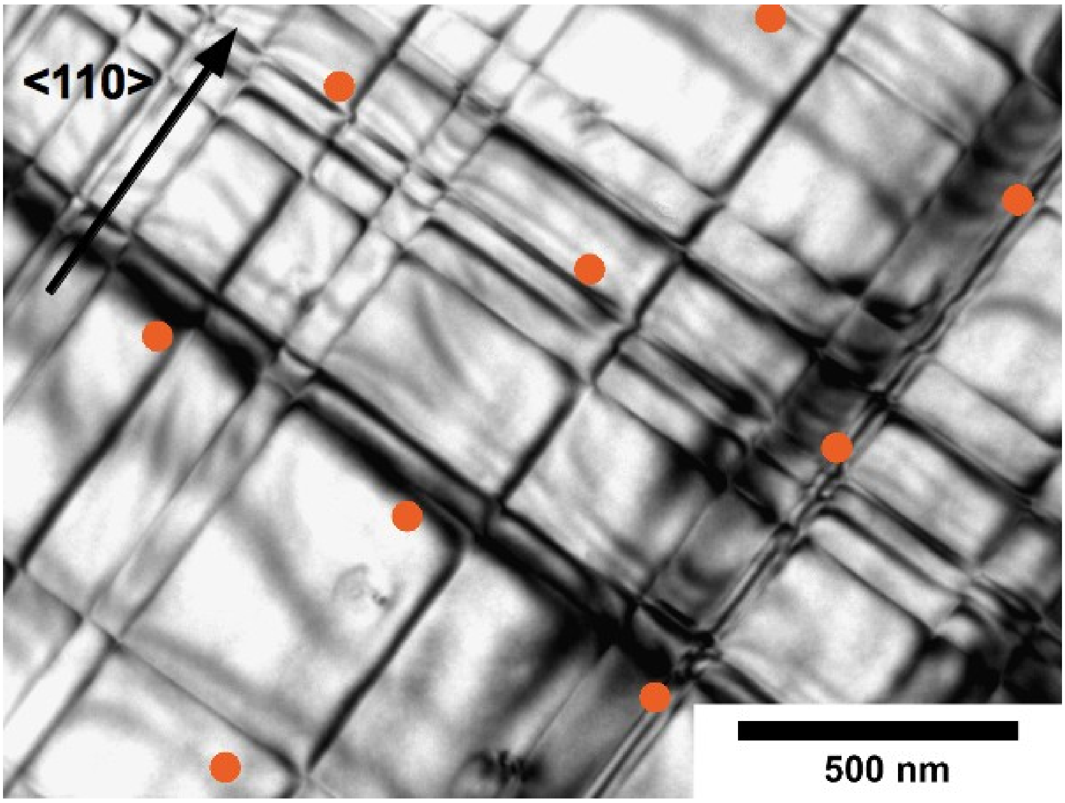

Figure 39: Network of misfit dislocations in a Si/Ge superlattice structure grown on a (100)-oriented Si wafer (#081020) and projection of the nanowire array that will later be produced by electron beam lithography and reactive ion etching. (Plan view TEM micrograph)

Figure 39 shows the projection of a NW array onto a plan view TEM micrograph of the Si/Ge superlattice #081020. The NW rows are aligned in <110> direction. Their intended diameter is 40 nm; the distance in between is set to 500 nm. Several things can be seen on this image. First, a network of misfit dislocations is generated during the deposition of the Si/Ge superlattice due to the strain induced by the lattice mismatch between Si and Ge. The dislocation lines are aligned in <110> directions in the crystal, which is the direction with the highest density of atoms perpendicular to the growth direction.

Since dislocations preferably nucleate at preexisting defects or impurities, they are not aligned with a constant distance, but instead they are clustered. The dislocation density is approximately 2×10^9 cm^{-2}. The correlation with the corresponding cross-section TEM micrograph (Figure 40) shows that the dislocations are located in the interface region below the superlattice. Also, they are pure 60° dislocations, no dislocation splitting could be found.

In a superlattice, the strain energy stored in the individual layers add up until the nucleation energy for dislocation formation is exceeded. The average Ge content

$$X_{av} = \frac{X_1 \cdot d_1 + X_2 \cdot d_2}{d_1 + d_2} \tag{36}$$

of a superlattice consisting of two alternating layers 1 and 2 must be used for calculating its critical thickness [143-146]. The critical thickness obtained for $\boldsymbol{X}$ = 0.3 is 8 nm and is therefore by far exceeded by the total thickness of the superlattice, which is 57.6 nm.

The position of the misfit dislocations is in contrast to the conventional concept of pseudomorphic growth, where first a pseudomorphic layer is grown which is followed by a partly relaxed layer with misfit dislocations, finally covered by a fully relaxed layer. Whether the dislocations were generated at the interface or were pushed to the interface during growth remains unclear.

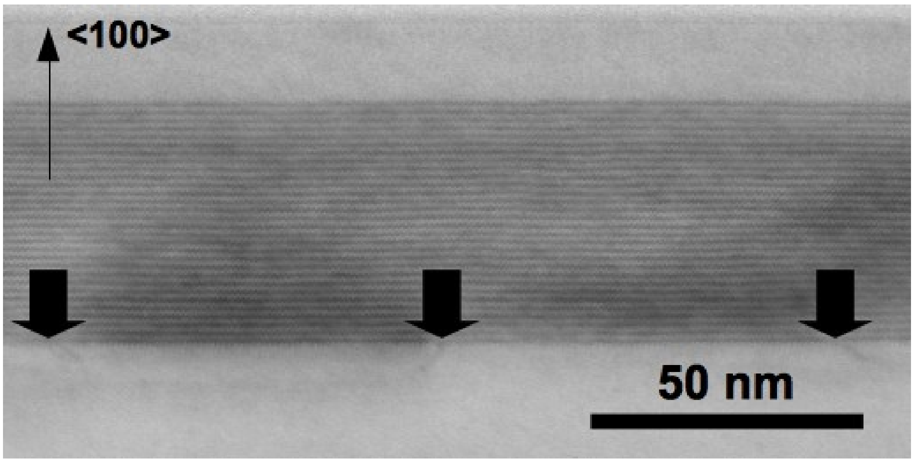

Figure 40: Misfit dislocations at the interface between the Si/Ge superlattice and the Si buffer layer. Cross-section TEM micrograph (Direction: <110>).

The second observation connected to Figure 39 is that most of the NWs etched into this heterostructure should be free of dislocations, but there should also be entire rows of NWs with a dislocation inside. However, the presence of dislocations could not be verified for any of the investigated NWs, which where in the diameter range of 15 to 70 nm. This can either be explained by technical reasons or physical reasons. Since the cross-section TEM samples were prepared in <110>

direction, only the dislocations aligned with the beam axis can be seen. The preparation of plan view TEM samples was not possible up to now due to the small size of the NW array fabricated by EBL and RIE.

Using the average Ge content of 0.3 in the superlattice structure, a critical NW radius of ≈ 44 nm is obtained through equation (12). Thus any dislocation which is left in the NW after the etching process should be unstable. If there are any dislocation half-loops left in the NWs, which has yet to be proven, the theoretical considerations above led to the conclusion that these misfit dislocations can be removed by a proper thermal treatment to provide the activation energy $\boldsymbol{E_A}$ for an initiation of dislocation glide. If the radius of the NW is below the critical radius $\boldsymbol{r_C}$, it can be transformed from the relaxed state with the dislocation to a strained state without the dislocation. Although the strain inside the NW is increased in the end, the free energy of the system is lowered. If the average distance between the dislocations in Figure 39 is compared with the NW diameter, the conclusion that the NW radius is below $\boldsymbol{r_C}$ is reasonable. The question is, whether the dislocations already moved out of the NW during the etching process – implying that there really are no dislocations left which can be investigated – or a sufficient energy was provided by the ion bombardment during sample preparation or by the TEM electron beam to initiate the movement.

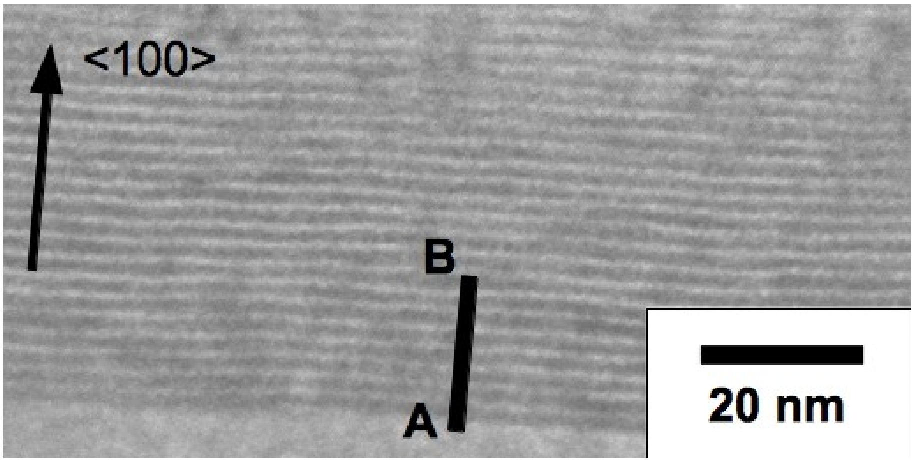

Figure 41: Section of the Si/Ge superlattice #081020 annealed at 600 °C for one hour. The line A → B indicates the position where the concentration profile was obtained.

But a thermal treatment might also induce a diffusion of the Si and Ge atoms, eventually leading to the transformation of the superlattice structure to a single $Si_{1-X}Ge_X$ block. The latter state is also energetically favourable because of a reduction of the maximum Ge concentration and thus a reduction of the strain. Considering the potential application as a thermoelectric element, this transformation must be prevented. This, on the one hand, limits the possibilities to anneal the NWs, and, on the other hand, also the temperature range for their application. To guarantee a long lifetime and high yields, a thermoelectric device containing Si/Ge superlattice structures must operate at temperatures below the activation threshold for diffusion.

As a preliminary experiment for the dislocation removal procedure and as a reference for future experiments with the NW arrays, the superlattice #081020 was annealed at 600 °C for one hour. A TEM cross-section micrograph of this sample can be seen in Figure 41. The corresponding concentration profile A → B (Figure 42) did not reveal any significant change in the Ge contents. Furthermore, the same dislocation pattern and dislocation density was observed by TEM plan view investigations of the superlattice structure.

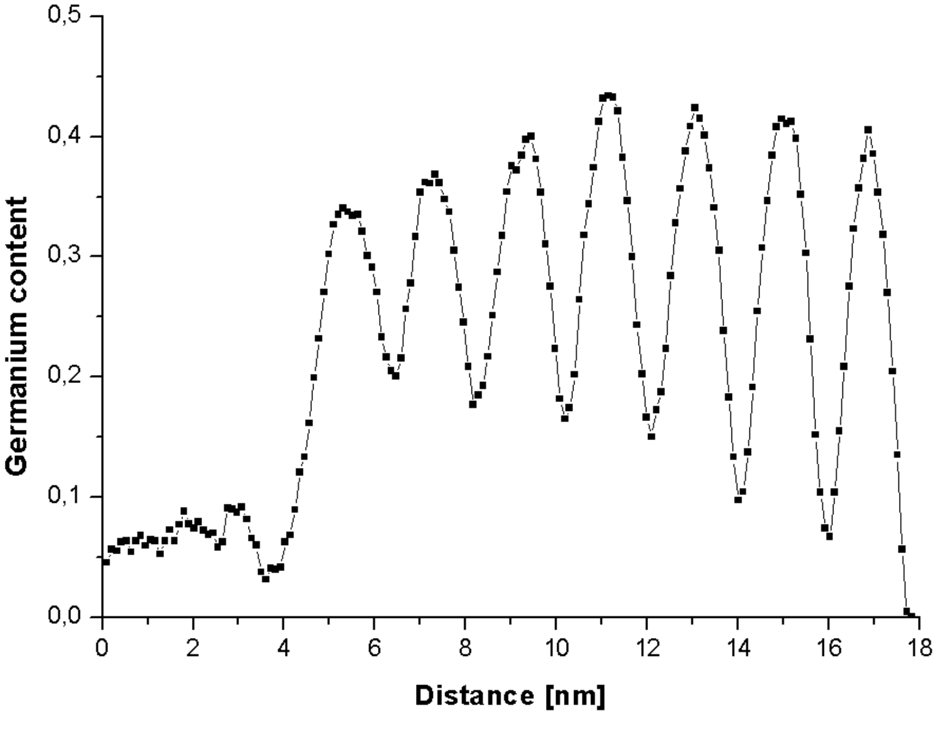

Figure 42: Concentration profile of a section of the Si/Ge superlattice structure #081020 annealed at 600 °C for one hour. The Germanium content X in the $Si_{1-X}Ge_X$ *alloy again varies between 0.35 and 0.45. The average peak distance was normalized to 1.92 nm in order to obtain the appropriate Germanium content.*

5.4 Summary and Conclusions on the Top-Down Approach

Arrays of nanowire-based vertical Si/Ge heterostructures were fabricated on Si (100) and Si (111) substrates by an approach combining crystal growth by MBE, mask fabrication by EBL, and NW etching by RIE. The NWs contain a 30 or 40 period Si/Ge superlattice. For the 30 period superlattice heterostructure grown on Si (100), a concentration profile was obtained revealing an average maximum Ge content of approximately 0.4 in the individual layer. Due to the difference in the surface energy, Ge strongly segregates in Si leading to the lower Ge concentration compared to the fact that 100 at.-% Ge were deposited. Nevertheless, enough strain is accumulated in the superlattice during growth to obtain a network of pure 60° misfit dislocations at the bottom of the superlattice. After etching, there is a certain chance that a NW contains one of these dislocations. However, no dislocations were found so far by TEM investigations. If there are indeed any dislocations left, they might be removed by proper thermal treatment of the NW arrays if the annealing temperature provides enough thermal energy to overcome the activation energy necessary to enable the movement of the dislocations.

The formation of dislocations is a drawback of this approach, but it can not be avoided if Ge layers with high concentrations and sharp interfaces should be obtained. Furthermore, there is no other approach available which offers the precise growth control of MBE for the fabrication of Si/Ge heterostructures. EBL and RIE also have there specific drawbacks, especially the proximity effect and an isotropic etching component leading to a non-uniform shape and irregular side walls of the NWs. It remains to be seen how the surface influences the electrical and thermoelectric properties of these NWs.

On the positive side, this approach allows the precise control not only of the distance of the individual NWs but also the exact position of each NW over large areas which is especially important for later contacting. The size of the NW field was 100 µm x 100 µm, but it can be easily expanded. The current set-up of the EBL machine that was used limits the size of the exposed spot of the photoresist to a minimum structure size of 40 nm x 40 nm. By underetching, the NW diameter can be decreased even further, although at the cost of a rough and concave surface, as mentioned above. Since this specific method for NW fabrication does not involve any metals, a metal contamination can be excluded.

6 Comparison of the Investigated Bottom-Up and Top-Down Approaches

There are several significant differences between the two approaches to fabricate Si/Ge NW heterostructures. They not only manifest themselves in the morphology and structural properties of the NWs but also in the influence of the process parameters. The bottom-up approach presented in this work is a single-step process, i. e. the catalyst deposition and the NW growth are done in the same UHV MBE machine, without interruption. Therefore the growth occurs under very clean and reproducible conditions. On the other hand, the top-down approach consists of three separate steps: i) the Si/Ge heterostructure growth, ii) the pattern formation / mask fabrication by EBL, and, finally, iii) the etching of the NWs by RIE. Obviously, much more independent parameters are involved in the second method, resulting in a more time consuming and more complicated process.

This, however, also comes with certain benefits, especially concerning potential applications. Although the parameters might differ, the etching process is not limited to <111> directions. Instead, it can be applied to other crystal orientations, e. g. the <100> direction, which is the preferred wafer orientation in industrial fabrication processes. Furthermore, the NW fabrication does not involve a metal catalyst, excluding potential contaminations of the NWs from the beginning. Last but not least, the presented top-down process results in well-ordered structures with well-defined distances and positions, allowing future contacting of the NWs. On the negative side, the NWs still have an irregular cross-section due to the proximity effect, which is a statistical effect based on electron scattering processes. Possibilities to prevent this effect need to be studied. There is also a certain lateral etching leading to side walls with a concave shape and a rough surface.

The potential formation of misfit dislocations is directly linked to the maximum achievable Ge concentration in the NWs and the sharpness of the Si/Ge interfaces. A high element concentration and sharp interfaces favour the formation of dislocations (top-down approach), while low Ge concentrations and diffuse interfaces are accompanied by the absence of dislocations (bottom-up approach).

Other advantages of the bottom-up approach are the hexagonal cross-section and the defined surfaces due to the formation of facets. The disadvantages include the statistical distribution of the NWs on the surface thus preventing a contacting of individual NWs, and the metal contamination due to the incorporation of catalyst atoms. A comparison concerning the application potential is summarised in Table 8.

Comparison: Applications	
Bottom-Up Approach	**Top-Down Approach**
🟢 Single step process	🔴 Multi-step process
🟢 No dislocations	🔴 Dislocations
🟢 Hexagonal cross-section	🔴 Irregular cross-section
🟢 Surface planes are crystal planes	🔴 Surface roughness
🔴 No growth in <100> direction	🟢 Independent of crystal orientation
🔴 Metal contamination (catalyst)	🟢 No metal contamination
🔴 Statistical distribution of nanowires	🟢 Ordered structures
🔴 Low Ge concentrations	🟢 High element concentrations
🔴 Diffuse interfaces	🟢 Sharp interfaces

Table 8: Comparison of the bottom-up and the top-down approach concerning their application potential

Both approaches offer more than enough future challenges and are equally interesting from a scientific point of view (Table 9). There is, for instance, a growing interest in the investigation of the optical properties of Si/Ge superlattice structures including the possibility of light emission [2-8]. Furthermore, Si/Ge NW heterostructures fabricated by the top-down approach offer a possibility to study quantum confinement effects. On the other hand, the diffusion phenomena that occur during the growth of NWs by the bottom-up approach are not fully understood. This includes the diffusion of the Si and Ge atoms, the incorporation of catalyst atoms, but also the incorporation of dopant atoms. Especially the VSS growth seems to be a promising candidate for the fabrication of sharp interfaces by the bottom-up approach.

Comparison: Physics	
Bottom-Up Approach	**Top-Down Approach**
• Crystal growth	• Crystal growth
• Diffusion phenomena	• Formation and motion of dislocations
• VLS growth	• Quantum well structures
• VSS growth	• Optical properties
• …	• …

Table 9: Comparison of the bottom-up and the top-down approach concerning physics

Finally, Table 10 gives an overview on selected NW parameters and their dependence on corresponding process parameters. It points out the importance of the diameter of the catalyst droplet because it influences the NW diameter, length, and the absolute position of the Ge layer. Although there are more parameters involved in the top-down approach, this also leads to a greater flexibility. For instance, the NW diameter and the distance, as well as the arrangement can be adjusted individually by the EBL mask.

Parameter	***Dependence***	
	Bottom-Up Approach	**Top-Down Approach**
NW Length	• Deposition time ***t*** • Deposition rate • Diameter of catalyst (MBE: $l \rightarrow const.$ / $l_{max} \approx 1\,\mu m$)	• Etch time ***t*** • Etch rate
NW Diameter	• Diameter of catalyst	• Primarily: EBL mask • Secondarily: Lateral etching (RIE)
NW Position	• Statistical distribution	• EBL mask
Ge layer position	• Deposition time ***t*** • Deposition rate • NW diameter	• Deposition time ***t*** • Deposition rate
Ge concentration	• Si to Ge ratio in vapour phase* • Temperature ***ϑ*** (→ Composition of eutectic droplet)	• Si to Ge ratio in vapour phase* • Temperature ***ϑ*** (→ Interdiffusion)
** For the experiments mentioned in this work, either 100% Si or 100% Ge were deposited.*		

Table 10: Overview on NW parameters and their controllability

7 Summary, Conclusions and Outlook

7.1 Summary and Conclusions

Nanowire-based Si/Ge heterostructures are considered as building blocks for future devices, especially FETs and thermoelectric elements. They are also interesting candidates for the scientific investigation of quantum confinement effects in nanostructures.

In principle, there are two categories of approaches to fabricate these Si/Ge NW heterostructures: Bottom-up approaches and top-down approaches. The former ones are constructive approaches with the NWs being directly grown on the substrate surface via a catalyst. Depending on the physical condition of the catalyst (liquid or solid), the underlying growth mechanism is either the vapour-liquid-solid (VLS) mechanism or the vapour-solid-solid (VSS) mechanism. The top-down approaches are mostly based on etching techniques. The Si/Ge heterostructures are grown first, and the NWs are later etched inside decomposing the surrounding volume.

To allow the successful implementation in devices, several tasks still have to be accomplished. This includes the exact control of the NW orientation and also its position for future contacting. Further challenges are the positioning of the Ge layers and the realization of sharp Si/Ge interfaces and high element concentrations within the Si and Ge part of the NWs.

Both approaches were compared concerning their potential to overcome these challenges. The diffusion-based VLS NW growth was selected as a representative bottom-up approach, whereas a multi-step etching process was selected as a representative top-down approach. In the latter case the NWs were fabricated by reactive ion etching (RIE), while the mask for the etching process was created by electron beam lithography (EBL). Both the VLS NWs and the Si/Ge heterostructures for the etching process were grown by MBE, a deposition technique which allows a precise growth control and clean and reproducible conditions due to the deposition in an UHV environment. In contrast to CVD techniques, where often GeH_4 is used as a precursor gas, it is also a non-toxic and safe process to fabricate Si/Ge heterostructures. A clear disadvantage of the MBE Si NW growth is the limitation of the NW diameter to values above 50-70 nm.

Simple Ge NW on Si NW heterostructures were grown by MBE as well as Si NWs with one or two thin Ge layers inside. The position of the Ge layers could be adjusted with high accuracy. It was also shown that the growth temperature is one of the most crucial process parameters, influencing not only the Ge concentration but the thermal stability of the NWs itself. The reduction of the growth temperature during the Ge deposition led to an increase in the Ge concentration and a reduction of the FWHM of the layers.

While no dislocations have been found up to now at the interfaces of the grown NWs, other groups have shown that catalyst atoms can be included into the crystal lattices of the growing NWs as point defects, independent of the deposition technique. This questions the application potential of VLS grown Si NWs and also Si/Ge NW heterostructures because these atoms act as recombination centres in Si and are drastically reducing the carrier lifetime.

In the top-down approach the Si/Ge heterostructure was grown first by MBE, leading to sharper interfaces and much higher element concentrations with the drawback of the generation of misfit dislocations at the interface. Nevertheless, by combining MBE deposition with EBL and RIE, well-ordered arrays of vertical nanowire-based Si/Ge heterostructures were fabricated on Si (100) and Si (111) substrates. The size of the NW array was 100 µm x 100 µm, but it could be easily expanded. The current set-up of our EBL machine limits the achievable minimum structure size to approx. 40 nm x 40 nm. By underetching the NW diameter could be decreased down to 15 nm, although at the cost of a rough and concave surface. Since no metal was involved in the fabrication process, metal inclusions could be excluded for this specific top-down approach.

From a scientific point of view, both approaches are equally interesting, for instance, to study crystal growth and diffusion mechanisms, and also to investigate the structural, electrical and optical properties of low-dimensional structures compared to the respective bulk properties. However, concerning their application potential for future devices, the top-down approach has several advantages over the bottom-up approach. First of all, for top-down approaches it is easier to obtain well-ordered structures, with a high homogeneity in NW diameters and lengths. Especially the MBE/EBL/RIE method also allows the future contacting of individual NWs, because the position of each NW is well known. One of the advantages of bottom-up approaches was their high NW density, NW length and homogeneous (but statistical) distribution over large areas of up to 5”-6” wafers. Today, this can, for instance, also be achieved by colloidal lithography and wet chemical etching techniques, another top-down approach [66-72].

The growth of NWs in <100> direction has up to now not been demonstrated for the conventional bottom-up approach. Depending on their diameter and the underlying substrate, Si NWs grow only in <111>, <110>, and <112> directions [132]. Unfortunately, (100) silicon substrates are the most common substrates for industrial applications. In contrast, vertical <100> NWs on (100) Silicon substrates can be easily produced by etching techniques.

Dislocations generated during the growth of the Si/Ge superlattice heterostructures may limit the application potential of the top-down approach, especially for optical and electric devices. However, in the case of thermoelectric devices, where large arrays of NWs are required, it should not matter if some NWs have dislocations and show a lower performance than the rest of the array.

The existence of dislocations in NWs after etching still needs to be verified by detailed investigations. Theoretical considerations emphasize that these dislocation half-loops are unstable and may be eliminated from etched NWs (with a radius below the critical radius) by a proper annealing procedure which has to be demonstrated experimentally.

7.2 Outlook

Several groups were able to combine both approaches to force Si NWs to grow in an ordered arrangement and/or in <100> direction, e. g. a colloidal mask was used to deposit the Au in a hexagonal arrangement [146], or the NWs were grown within an anodic aluminium oxide membrane on a <100> oriented Si wafer [147,148]. However, as long as the VLS growth depends on a metal droplet or particle as a catalyst, one of the major drawbacks of the bottom-up approach remains. With the possible inclusion of metal catalyst atoms inside the NWs as point defects, their application potential, especially for optical devices, is unclear. For the VSS growth, the metal contamination inside the NW could be drastically reduced. However, this has to be proven experimentally.

Although first experiments for the growth of Si/Ge NW heterostructures by CVD and VSS mechanism led to relatively sharp interfaces, misfit dislocations were observed at the interface [148]. As shown above, these dislocations could possibly be removed by thermal treatment. Again, this has to be proven experimentally. If the assumptions can be validated by experimental observations, the philosophy behind the fabrication of NW heterostructures will possibly change. Si/Ge heterostructures could be grown ignoring the formation of dislocations during growth, because they could be removed later.

Focussing back on the MBE/EBL/RIE method, Figure 43 gives an outlook how this process could be improved in the future. On the SEM micrograph a regular array of larger NWs (70 to 80 nm diameter) can be seen, but also much thinner NWs with diameters down to 10 nm. Although these NWs were created unintentionally by electron backscattering, these NWs demonstrate the possibility to decrease the NW diameter, if the spot size of the EBL set-up could be reduced. Both kinds of NWs also show a relatively smooth surface.

To demonstrate the application potential of the NW heterostructures fabricated by the top-down approach, prototype devices must be produced. Therefore reliable methods of surface passivation have to be developed. Also, possibilities of embedding the NWs in insulating materials must be studied, and last but not least, the NWs have to be contacted individually.

The mask for the contact pads and tracks could be produced, for instance, by another EBL step or by laser interference lithography. Furthermore, the thermoelectric properties, like electrical conductivity, thermal conductivity, and Seebeck coefficient of these NWs need to be studied to investigate in detail the application potential for thermoelectric devices.

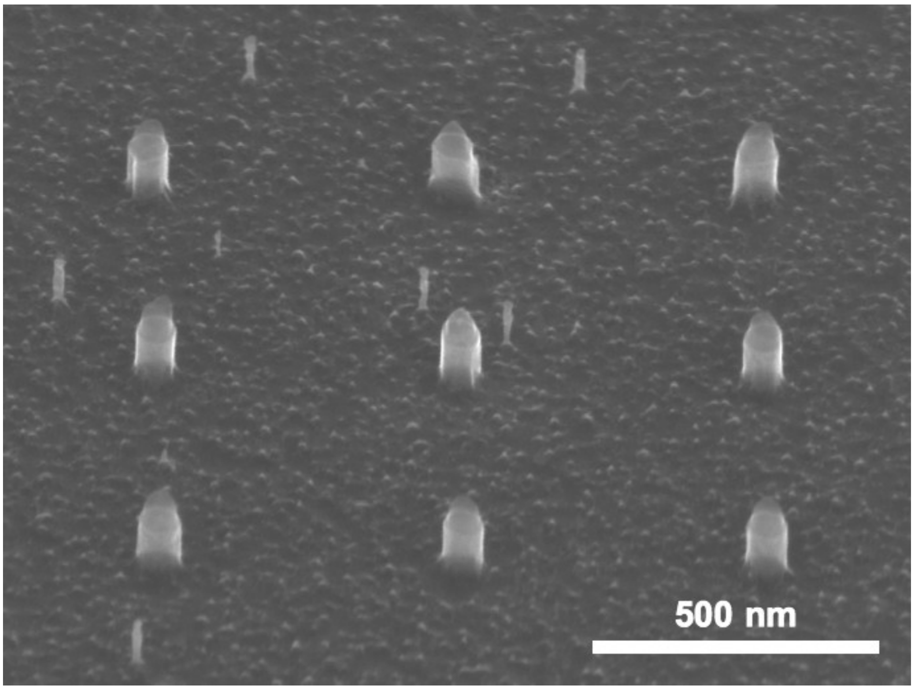

Figure 43: RIE of Si/Ge heterostructure nanowires with smooth surfaces (r = 30 to 40 nm). The smaller NWs were created unintentionally by electron backscattering. Their radius is about 5 to 7 nm. The photoresist is still on top of the nanowires.

References

[1] Y. Maeda, N. Tsukamoto, Y. Yazawa, Y. Kanemitsu, Y. Masumoto, *Appl. Phys. Lett.* 59 (1991) 3168

[2] A. J. Read, R. J. Needs, K. J. Nash, L. T. Canham, P. D. J. Calcott, A. Qteish, *Phys. Rev. Lett.* 69 (1992) 1232

[3] T. Ohno, K. Shiraishi, T. Ogawa, *Phys. Rev. Lett.* 69 (1992) 2400

[4] M. S. Hybertsen, M. Needels, *Phys. Rev. B* 48 (1993) 4608

[5] R. J. Needs, S. Bhattacharjee, K. J. Nash, A. Qteish, A. J. Read, L. T. Canham, *Phys. Rev. B* 50 (1994) 14223

[6] X. Y. Zhao, C. M. Wei, L. Yang, M. Y. Chou, *Phys. Rev. Lett.* 92 (2004) 236805

[7] S. Bhattacharya, D. Banerjee, K. W. Adu, S. Samui, *Appl. Phys. Lett.* 85 (2004) 2008

[8] N. D. Zakharov, V. G. Talalaev, P. Werner, A. A. Tonkikh, G. E. Cirlin, *Appl. Phys. Lett.* 83 (2003) 3084

[9] N. Usami, T. Mine, S. Fukatsu, Y. Shiraki, *Appl. Phys. Lett.* 64 (1994) 1126

[10] Y. Nakajiama, Y. Takahashi, S. Horiguchi, K. Iwadate, H. Namatsu, K. Kurihara, M. Tabe, *Appl. Phys. Lett.* 65 (1994) 2833

[11] J. L. Liu, Y. Shi, F. Wang, Y. Lu, R. Zhang, P. Han, S. L. Gu, Y. D. Zheng, *Appl. Phys. Lett.* 68 (1996) 352

[12] C. M. Lieber, *Mater. Res. Bull.* 28 (2003) 128

[13] H. J. Fan, P. Werner, M. Zacharias, *Small* 2 (2006) 700

[14] L. J. Lauhon, Mark S. Gudiksen, C. M. Lieber, *Phil. Trans. R. Soc. Lond. A* 362 (2004) 1247

[15] Y.-J. Yang, W. S. Ho, C.-F. Huang, S. T. Chang, C. W. Liu, *Appl. Phys. Lett.* 91 (2007) 102103

[16] M. B. Prince, *Phys. Rev.* 92 (1953) 681

[17] F. J. Morin, J. P. Maita, *Phys. Rev.* 96 (1954) 28

[18] G. Kästner, U. Gösele, *Philos. Mag.* 84 (2004) 3803

[19] M. S. Dresselhaus, Y. M. Lin, S. B. Cronin, O. Rabin, M. R. Black, G. Dresselhaus, T. Koga, *Semicond. Semimetals* 71 (2001) 1

[20] D. Li, Y. Wu, R. Fan, P. Yang, A. Majumdar, *Appl. Phys. Lett.* 83 (2003) 15

[21] A. I. Hochbaum, R. Chen, R. D. Delgado, W. Liang, E. C. Garnett, M. Najarian, A. Majumdar, P. Yang, *Nature* 451 (2008) 163

[22] L. D. Hicks, M. S. Dresselhaus, *Physical Review B* 47 (1993) 16631

[23] A. Boukai, Y. Bunimovich, J. Tahir-Kheli, J.-K. Yu, W. A. Goddard, J. Heath, *Nature* 452 (2008) 168

[24] W. Capinski, H. J. Maris, *Physica B* 219 (1996) 699

[25] S.-M. Lee, D. G. Cahill, R. Venkatasubramanian, *Appl. Phys. Lett.* 70 (1997) 2957

[26] R. Venkatasubramanian, E. Silvola, T. Colpitts, B. O'Quinn, *Nature* 413 (2001) 597

[27] T. Borca-Tasciuc, W. Liu, J. Liu, T. Zeng, D. Song, C. Moore, G. Chen, K. Wang, T. Radetic, R. Gronsky, T. Koga, M. S. Dresselhaus, *Superlattices Microstruct.* 28 (2000) 199

[28] S. T. Huxtable, A. R. Abramson, C.-L. Tien, A. Majumdar, C. Labounty, X. Fan, G. Zeng, J. Bowers, A. Shakouri, E. Croke, *Appl. Phys. Lett.* 80 (2002) 1737

[29] D. Li, Y. Wu, P. Kim, L. Shi, P. Yang, A. Majumdar, *Appl. Phys. Lett.* 83 (2003) 2934

[30] Y. Cui, C. M. Lieber, *Science* 291 (2001) 851

[31] J. Xiang, W. Lu, Y. Hu, Y. Wu, H. Yan, C. M. Lieber, *Nature* 441 (2006) 489

[32] Y. Huang, X. Duan, Y. Cui, L. J. Lauhon, K.-H. Kim, C. M. Lieber, *Science* 294 (2001) 1313

[33] J.-Y. Yu, S.-W. Chung, J. R. Heath, *J. Phys. Chem. B* 104 (2000) 11864

[34] R. S. Wagner, W. C. Ellis, K. Jackson, S. M. Arnold, *J. Appl. Phys.* 35 (1964) 2993

[35] R. S. Wagner, W. C. Ellis, *Appl. Phys. Lett.* 4 (1964) 89

[36] R. S. Wagner, W. C. Ellis, *Transaction of the Metallurgical Society of AIME* 233 (1965) 1053

[37] E. I. Givargizov, *J. Cryst. Growth* 31 (1975) 20

[38] E. I. Givargizov, *Higly Anisotropic Crystals*, D. Reidel, 1987

[39] H. Jagannathan, M. Deal, Y. Nishi, J. Woodruff, C. Chidsey, P. C. McIntyre, *J. Appl. Phys.* 100 (2006) 024318

[40] J. W. Dailey, J. Taraci, T. Clement, D. S. Smith, J. Drucker, S. T. Picraux, *J. Appl. Phys.* 96 (2004) 7556

[41] E. Tutuc, J. Appenzeller, M. C. Reuter, S. Guha, *Nano Lett.* 6 (2006) 2070

[42] J. H. Woodruff, J. B. Ratchford, I. A. Goldthorpe, P. C. McIntyre, C. E. D. Chidsey, *Nano Lett.* 7 (2007) 1637

[43] K. Kang, D. A. Kim, H.-S. Lee, C.-J. Kim, J.-E. Yang, M.-H. Jo, *Adv. Mater.* 20 (2008) 1

[44] H.Y. Tuan, D. C. Lee, T. Hanrath, B. A. Korgel, *Chem. Mater.* 17 (2005) 5705

[45] S. Hofmann, C. Sharma, R. Wirth, F. Cervantes-Sod, C. Ducati, T. Kasama, R. E. Dunin-Borokowski, J. Druckers, P. Bennett, J. Robertson, *Nat. Mater.* 7 (2008) 372

[46] S. Kodambaka, J. Tersoff, M. C. Reuter, F. M. Ross, *Science* 316 (2007) 729

[47] Y. Wang, V. Schmidt, S. Senz, U. Gösele, *Nat. Nanotechnol.* 1 (2006) 186

[48] J. Arbiol, B. Kalache, P. R. I. Cabarrocas, J. R. Morante, A. F. I. Morral, *Nanotechnology* 18 (2007) 305606

[49] Y. Yao, S. Fan, *Mater. Lett.* 61 (2007) 177

[50] G. A. Bootsma, H. J. Gassen, *J. Cryst. Growth* 10 (1971) 223

[51] E. C. Garnett, W. Liang, P. Yang, *Adv. Mater.* 19 (2007) 2946

[52] T. I. Kamins, R. Stanley Williams, D. P. Basile, T. Hesjedal, J. S. Harris, *J. Appl. Phys.* 89 (2001) 1008

[53] T. I. Kamins, R. Stanley Williams, T. Hesjedal, J. S. Harris, *Physica E* 13 (2002) 995

[54] Y.-H. Yang, S.-J. Wu, H.-S. Chiu, P.-I. Lin, Y.-T. Chen, *J. Phys. Chem. B* 108 (2004) 846

[55] L. Schubert, P. Werner, N. D. Zakharov, G. Gerth, F. Kolb, L. Long, U. Gösele, T. Y. Tan, *Appl. Phys. Lett.* 84 (2004) 4968

[56] H. D. Park, T. P. Hogan, *J. Vac. Soc. Technol. B* 22 (2004) 237

[57] P. Werner, N. D. Zakharov, G. Gerth, L. Schubert, U. Gösele, *Int. J. Mat. Res. (formerly Z. Metallkd.)* 97 (2006) 7

[58] N. D. Zakharov, P. Werner, G. Gerth, L. Schubert, L. Sokolov, U. Gösele, *J. Cryst. Growth* 290 (2006) 6

[59] R. Dujardin, V. Poydenot, T. Devillers, V. Favre-Nicolin, P. Gentile, A. Barski, *Appl. Phys. Lett.* 89 (2006) 153129

[60] L. Schubert, Doctoral Thesis, Martin Luther University Halle-Wittenberg, 2006 (in German)

[61] C. Mouchet, L. Latu-Romain, C. Cayron, E. Rouviere, C. Celle, J.-P. Simonato, *Nanotechnology* 19 (2008) 335603

[62] J. M. Redwing, K.-K. Lew, T. Bogart, L. Pan, E. C. DickeyA. H. Carim, Y. Wang, M. Cabassi, T. S. Mayer, *Proc. SPIE-Int. Soc. Opt. Eng.* 52 (2004) 5361

[63] T. E. Clark, P. Nimmatoori, K.-K. Lew, L. Pan, J. M. Redwing, E. C. Dickey, *Nano Lett.* 8 (2008) 1246

[64] Y. Wu, R. Fan, P. Yang, *Nano Lett.* 2 (2002) 83

[65] K. Peng, Z. Huang, J. Zhu, *Adv. Mater.* 16 (2004) 73

[66] J. C. Hulteen, D. A. Treichel, M. T. Smith, M. L. Duval, T. R. Jensen, R. P. Van Duyne, *J. Phys. Chem. B* 103 (1999) 3854

[67] C. L. Cheung, R. J. Nikolić, C. E. Reinhardt, T. F. Wang, *Nanotechnology* 17 (2006) 1339

[68] K. Peng, M. Zhang, A. Lu, N. Wong, R. Zhang, S. Lee, *Appl. Phys. Lett.* 90 (2007) 163123

[69] Z. P. Huang, H. Fang, J. Zhu, *Adv. Mater.* 19 (2007) 744

[70] X. Li, P. W. Bohn, *Appl. Phys. Lett.* 77 (2000) 2572

[71] R. Douani, K. Si-Larbi, T. Hadjersi, N. Megouda, A. Manseri, *Phys. Status Solidi A* 205 (2007) 225

[72] C. Chartier, S. Bastide, C. Lévy-Clément, *Electrochimica Acta* 53 (2008) 5509

[73] A. Wolfsteller, N. Geyer, T.-K. Nguyen-Duc, P. Das Kanungo, N. D. Zakharov, M. Reiche, W. Erfurth, H. Blumtritt, S. Kalem, P. Werner, U. Gösele, *Thin Solid Films* 518 (2010) 2555

[74] X. Wang, K. L. Pey, W. K. Choi, C. K. F. Ho, E. Fitzgerald, D. Antoniadis, *Electrochem. Solid-State Lett.* 12 (2009) K37

[75] A. Y. Cho, *J. Cryst. Growth* 201/202 (1999) 1

[76] J. R. Arthur, *Surf. Sci.* 500 (2002) 189

[77] W. Braun: *Applied RHEED. Reflection High-Energy Electron Diffraction During Crystal Growth*, Springer-Verlag, Berlin, 1999

[78] A. Ishizaka, Y. Shiraki, *J. Electrochem. Soc.* 133 (1986) 666

[79] W. Kern, *RCA Eng.* 28 (1983) 99

[80] W. C. Chen, Y. R. Kin, Y. J. Guo, S. T. Wu, *Jpn. J. Appl. Phys.* 42 (2003) 208

[81] V. Talyansky, S. Choopun, M. J. Downes, R. P. Sharma, T. Venkatesan, Y. X. Li, L. G. Salamanca-Riba, M. C. Wood, R. T. Lareau, K. A. Jones, *J. Mater. Res.* 14 (1999) 3298

[82] L. Hultman, B.O. Johansson, J.-E. Sundgren, L. C. Markert, J. E. Greene, *Appl. Phys. Lett.* 53 (1988) 1175

[83] N. Biunno, J. Narayan, A. R. Srivatsa, O. W. Holland, *Appl. Phys. Lett.* 55 (1989) 405

[84] F. C. Frank, J. H. van der Merwe, *Proc. R. Soc. London A* 198 (1949) 205 and 216

[85] J. H. van der Merwe, *J. Appl. Phys.* 34 (1963) 123

[86] J. W. Matthews, A. E. Blakeslee, *J. Cryst. Growth* 27 (1974) 118

[87] J. W. Matthews, A. E. Blakeslee, *J. Cryst. Growth* 29 (1975) 273

[88] J. W. Matthews, A. E. Blakeslee, *J. Cryst. Growth* 32 (1976) 265

[89] E. Kasper, A. Schuh, G. Bauer, B. Holländer, H. Kibbel, *J. Cryst. Growth* 157 (1995) 68

[90] D. J. Paul, *Semicond. Sci. Technol.* 19 (2004) R75

[91] J. W. Matthews, *J. Vac. Sci. Technol.* 12 (1975) 126

[92] J. C. Bean, L. C. Feldmann, A. T. Fiory, S. Nakahara, I. K. Robinson, *J. Vac. Sci. Technol.* A2 (1984) 436

[93] C. H. Chern, K. L. Wang, G. Bai, M.-A. Nicolet, *Mater. Res. Soc. Proc. (Silicon Mol. Beam Epi.)* 220 (1991) 135

[94] R. People, J. C. Bean, *Appl. Phys. Lett.* 47 (1985) 322

[95] B. W. Dodson, J. Y. Tsao, *Appl. Phys. Lett.* 51 (1987) 1325

[96] J. Y. Tsao, B. W. Dodson, S. T. Picraux, D. M. Cornelison, *Phys. Rev. Lett.* 59 (1987) 2455

[97] D. C. Houghton, *J. Appl. Phys.* 70 (1991) 2136

[98] http://www.sp.phy.cam.ac.uk/~SiGe/Strain%20in%20Silicon%20Germanium%20%28SiGe%29.html

[99] J. P. Hirth, J. Lothe, *Theory of Dislocations*, 2nd Edition, John Wiley & Sons, 1982

[100] A. A. Stekolnikov, J. Furthmüller, F. Bechstadt, *Phys. Rev. B* 65 (2002) 115318

[101] D. J. Godbey, M. G. Ancona, *J. Vac. Sci. Technol. B* 11 (1993) 1120

[102] G. G. Jernigan, P. E. Thompson, C. L. Silvestre, *Surf. Sci.* 380 (1997) 417

[103] D. A. Grutzmacher, T. O. Sedgwick, A. Powell, M. Tejwani, S. S. Iyer, J. Cotte, F. Cardone, *Appl. Phys. Lett.* 65 (1993) 2531

[104] E. S. Tok, N. J. Woods, J. Zhang, *J. Cryst. Growth* 209 (2000) 321

[105] S. M. Sze: *Semiconductor Devices – Physics and Technology*, John Wiley & Sons, 1985

[106] E. R. Weber: *Solubility of Au in Si*. In: *Properties of Silicon*, INSPEC, 1988

[107] W. M. Bullis, *Solid State Elec.* 9 (1966) 143

[108] O. Madelung [Ed.]: *Semiconductors Group IV Elements and III-V Compounds*. In: R. Poerschke [Ed.]: *Data in Science and Technology*, Springer-Verlag, Berlin, 1991

[109] N. A. Stolwijk, B. Schuster, J. Holzl, *Appl. Phys. A Mater. Sci. Process.* 33 (1984) 133

[110] E. Ertekin, P. A. Greaney, T. D. Sands, D. C. Chrzan, *MRS Proc*. 737 (2002) F 0.4

[111] D. B. Holt, B. G. Yacobi: *Extended Defects in Semiconductors*, Cambridge University Press, 2007

[112] L. Reimer, P. W. Hawks [Ed.]: *Scanning Electron Microscopy: Physics of Image Formation and Microanalysis*, Springer-Verlag, Berlin, 1998

[113] B. Fultz, J. M. Howe: *Transmission Electron Microscopy and Diffractometry of Materials*, Springer-Verlag, Berlin, 2007

[114] M. Henzler, W. Göpel: *Oberflächenphysik des Festkörpers*, Teubner-Verlag, Stuttgart, 1991 (in German)

[115] J. M. Ziman: *Prinzipien der Festkörpertheorie*, Verlag Harri Deutsch, Frankfurt am Main, 1992 (in German)

[116] A. Wolfsteller: *in situ-RHEED-Messungen während der ionenstrahlgestützten Deposition dünner Nitridschichten*, diploma thesis, University of Leipzig, 2006 (in German)

[117] H. Bethge, J. Heydenreich: *Elektronenmikroskopie*, VEB Deutscher Verlag der Wissenschaften, 1982 (in German)

[118] E. Fuchs, H. Oppolzer, H. Rehme: *Particle Beam Microanalysis. Fundamentals, Methods and Applications*, Wiley-VCH, Weinheim, 1998

[119] J. I. Goldstein, D. E. Newbury, P. Echlin, D. C. Joy, C. E. Lyman, E. Lifshin, L. C. Sawyer, J. R. Michael: *Scanning Electron Microscopy and X-Ray Microanalysis*, 3rd Edition, Springer Science and Business Media Inc., New York, 2003

[120] T. B. Massalski, J. L. Murray, L. H. Bennet, H. Baker [Eds.]: *Binary Alloy Phase Diagrams*, Vol. 1, American Society for Metals, Metals Park, OH, 1986

[121] B. Predel, H. Bankstahl, *J. Less-Common Metals* 43 (1975) 191

[122] B. Predel, H. Bankstahl, T. Gödecke, *J. Less-Common Metals* 44 (1976) 39

[123] D. V. Ragone, *Thermodynamics of Materials*, Vol. 2, John Wiley & Sons, 1995

[124] E. I. Givargizov, A. A. Chernov, *Sov. Phys. Crystallogr*. 18 (1973) 89

[125] V. Schmidt, S. Senz, U. Gösele, *Appl. Phys. A* 80 (2005) 445

[126] W. Ostwald, *Zeitschrift für physikalische Chemie* XXII (1897) 289 (in German)

[127] I. M. Lifshitz, V. V. Slyozov, *J. Phys. Chem. Solids* 19 (1961) 35

[128] C. Wagner, *Zeitschrift für Elektrochemie* 65 (1961) 581

[129] J. B. Hannon, S. Kodambaka, F. M. Ross, R. M. Tromp, *Nature* 440 (2006) 69

[130] W. Kossel: *Kristallwachstumstheorie*, in: *Naturwissenschaften* 18 (1930) 901 (in German)

[131] W. Kleber, H.-J. Bautsch, J. Bohm: *Einführung in die Kristallographie*, 18th Edition, Oldenbourg, 2002 (in German)

[132] V. Schmidt, S. Senz, U. Gösele, *Nano Lett.* 5 (2005) 931

[133] F. M. Ross, J. Tersoff, M. C. Reuter, *Phys. Rev. Lett.* 95 (2005) 146104

[134] V. Schmidt, U. Gösele, *Science* 316 (2007) 698

[135] J. E. Allen, E. R. Hemesath, D. E. Perea, J. L. Lensch-Falk, Z. Y. Li, F. Yin, M. H. Gass, P. Wang, A. L. Bleloch, R. E. Palmer, L. J. Lauhon, *Nature Nanotech.* 3 (2008) 168

[136] S. H. Oh, K. van Benthem, S. I. Molina, A. Y. Borisevich, W. Luo, P. Werner, N. D. Zakharov, D. Kumar, S. T. Pantelides, S. J. Pennycook, *Nano Lett.* 8 (2008) 1016

[137] M. C. Putnam, M. A. Filler, B. M. Kayes, M. D. Kelzenberg, Y. Guan, N. S. Lewis, J. M. Eiler, H. A. Atwater, *Nano Lett.* 8 (2008) 3109

[138] A. N. Broers: *Combined electron and ion beam processes for microelectronics. Electronics and Reliability*, Volume 4, p. 103, Pergamon Press, 1965

[139] Z. Cui: *Micro-Nanofabrication. Technologies and Applications*, Higher Education Press / Springer-Verlag, 2005

[140] B. Chapman: *Glow Discharge Processes: Sputtering and Plasma Etching*, John Wiley & Sons, Inc., New York, 1980

[141] B. Gorowitz, R. J. Saia: *Reactive Ion Etching*, in: N. G. Einspruch, D. M. Brown [Eds.]: *VLSI Electronics: Microstructure Science*, Vol. 8, Chapter 10, Academic Press, 1984

[142] S. Yasin, D. G. Hasko, H. Ahmed, *Appl. Phys. Lett.* 78 (2001) 2760

[143] S. C. Jain, M. Willander: *Semiconductors and Semimetals*, *Volume 74*: *Silicon-Germanium Strained Layers and Heterostructures*, 2nd Editon, Academic Press, 2003

[144] S. C. Jain, W. Hayes, *Semicond. Sci. Technol.* 6 (1991) 547

[145] R. People, *IEEE J. Quantum Electronics*, 22 (1986) 1696

[146] B. Fuhrmann, H. S. Leipner, H.-R. Höche, L. Schubert, P. Werner, U. Gösele, *Nano Lett.* 5 (2005) 2524

[147] T. Shimizu, T. Xie, J. Nishikawa, S. Shingubara, S. Senz, U. Gösele, *Adv. Mater.* 19 (2007) 917

[148] T. Shimizu, Z. Zhang, S. Shingubara, S. Senz, U. Gösele, *Nano Lett.* 9 (2009) 1523

Appendix

A List of Formula Symbols, Abbreviations and Chemical Symbols

List of Formula Symbols

$\boldsymbol{A}$	Area / surface area	$[\boldsymbol{A}] = 1\ \mathrm{m}^2 = 1 \times 10^{18}\ \mathrm{nm}^2$
$\boldsymbol{a_B}$	Exciton Bohr radius	$[\boldsymbol{a_B}] = 1\ \mathrm{m} = 1 \times 10^{9}\ \mathrm{nm}$
$\boldsymbol{a}$	Lattice parameter	$[\boldsymbol{a}] = 1\ \mathrm{m} = 1 \times 10^{9}\ \mathrm{nm}$
$\boldsymbol{\alpha}$	Linear thermal expansion coefficient	$[\boldsymbol{\alpha}] = 1\ \mathrm{K}^{-1}$
$\vec{b}$	Burgers vector	
$\boldsymbol{c_0}$	Speed of light in vacuum	$\boldsymbol{c_0} = 299{,}792{,}458\ \mathrm{m} \cdot \mathrm{s}^{-1}$
$\boldsymbol{d}$	Nanowire diameter	$[\boldsymbol{d}] = 1\ \mathrm{m} = 1 \times 10^{9}\ \mathrm{nm}$
$\boldsymbol{d_{hkl}}$	Lattice plane distance	$[\boldsymbol{d_{hkl}}] = 1\ \mathrm{m} = 1 \times 10^{9}\ \mathrm{nm}$
$\boldsymbol{\Delta E}$	Energy gap	$[\boldsymbol{E}] = 1\ \mathrm{J} \approx 1.602176 \times 10^{-19}\ \mathrm{eV}$
$\boldsymbol{E}$	Energy	$[\boldsymbol{E}] = 1\ \mathrm{J} \approx 1.602176 \times 10^{-19}\ \mathrm{eV}$
$\boldsymbol{e}$	Elementary charge	$\boldsymbol{e} \approx 1.602176 \times 10^{-19}\ \mathrm{C}$
$\boldsymbol{\varepsilon}$	Dielectric constant of the material	
$\boldsymbol{\varepsilon_0}$	Electric constant	$\boldsymbol{\varepsilon_0} = 8.854187817 \times 10^{-12}\ \mathrm{C} \cdot \mathrm{V}^{-1} \cdot \mathrm{m}^{-1}$
$\boldsymbol{f}$	Lattice mismatch	
$\boldsymbol{\varphi}$	Diffraction angle	$[\boldsymbol{\varphi}] = 1°$
$\boldsymbol{G}$	Free energy	$[\boldsymbol{G}] = 1\ \mathrm{J}$
$\boldsymbol{\Delta G_K}$	Nucleation enthalpy	$[\boldsymbol{\Delta G_K}] = 1\ \mathrm{J} \approx 1.602176 \times 10^{-19}\ \mathrm{eV}$
$\vec{g}$	Reciprocal lattice vector	
$\boldsymbol{\Gamma}$	Hopping rate (surface diffusion)	$[\boldsymbol{\Gamma}] = 1\ \mathrm{s}^{-1}$
$\boldsymbol{\gamma}$	Surface Energy	$[\boldsymbol{\gamma}] = 1\ \mathrm{J} \cdot \mathrm{m}^{-2}$
$\boldsymbol{\hbar}$	Reduced Planck constant	$\boldsymbol{\hbar} = 1.05457266 \times 10^{-34}\ \mathrm{J} \cdot \mathrm{s}$
$\boldsymbol{h, h_c}$	Germanium layer thickness, critical thickness	$[\boldsymbol{h}] = 1\ \mathrm{m} = 1 \times 10^{9}\ \mathrm{nm}$
$\boldsymbol{hkl}$	Miller indices	
$\boldsymbol{I}$	(Particle) Flux	$[\boldsymbol{I}] = 1\ \mathrm{mol} \cdot \mathrm{m}^{-2} \cdot \mathrm{s}^{-1}$
$\boldsymbol{k}$	Diffraction order	
$\vec{k}$	Wave vector	

k_B	Boltzmann constant	$k_B = 1.3806504(24) \times 10^{-23}$ J · K^{-1}
κ_{El}	Electrical conductivity	$[\kappa_{El}] = 1$ S · m^{-1}
κ_{Th}	Thermal conductivity	$[\kappa_{Th}] = 1$ W · m^{-1} · K^{-1}
l	Nanowire length	$[l] = 1$ m $= 1 \times 10^{9}$ nm
λ_e	Electron wavelength	$[\lambda_e] = 1$ m $= 1 \times 10^{9}$ nm
m_e	Electron rest mass	$m_e = 9.10938188 \times 10^{-31}$ kg
m_r	Reduced mass of the electron-hole pair	$[m_r] = 1$ kg
m_e^{eff}	Effective mass of the electron	$[\ m_e^{eff}\ ] = 1$ kg
m_h^{eff}	Effective mass of the hole	$[\ m_h^{eff}\ ] = 1$ kg
μ	Chemical potential	$[\mu] = 1$ kJ · mol^{-1}
ν	Poisson ratio	
ν_N	Nucleation frequency	$[\nu_N] = 1$ Hz $= 1$ s^{-1}
ν_S	Attempt frequency (surface diffusion)	$[\nu_S] = 1$ Hz $= 1$ s^{-1}
Ξ	Intensity	a. u.
Ω	Specific atomic volume	
p	Pressure	$[p] = 1$ bar $= 1 \times 10^{5}$ Pa
R_D	Rate of desorption	$[R_D] = 1$ s^{-1}
r, r_C	Radius, critical radius	$[r] = 1$ m $= 1 \times 10^{9}$ nm
ρ_{NW}	Nanowire density	$[\rho_{NW}] = 1$ cm^{-2}
S	Seebeck coefficient	$[S] = 1$ V · K^{-1}
Σ	Specific surface energy	$[\Sigma] = 1$ N · m^{-1}
σ	Surface tension	$[\sigma] = 1$ N · m^{-1}
T / ϑ	Temperature	$[T] = 1$ K / $[\vartheta] = 1$ °C
Θ	Glancing angle	$[\Theta] = 1°$
θ	Angle between dislocation line and Burgers vector	$[\theta] = 1°$
t	Time	$[t] = 1$ h $= 60$ min $= 3600$ s
τ_{eff}	Effective stress	$[\tau_{eff}] = 1$ MPa
U_{acc}	Acceleration voltage	$[U_{acc}] = 1$ V
V	Volume	$[V] = 1$ m^{3} $= 1 \times 10^{27}$ nm^{3}
$\mathbf{v}$	Velocity	$[\mathbf{v}] = 1$ m · s^{-1}
X	Germanium content	$(0 \leq X \leq 1)$
Z	Figure of merit	$[Z] = 1$ K^{-1}

List of Abbreviations

CVD	Chemical Vapour Deposition
EBL	Electron Beam Lithography
EDX	Energy Dispersive X-Ray Spectroscopy
FET	Field Effect Transistor
FWHM	Full Width at Half Maximum
MBE	Molecular Beam Epitaxy
NW	Nanowire
PLD	Pulsed Laser Deposition
PVD	Physical Vapour Deposition
QD	Quantum Dot
RF	Radio Frequency
RHEED	Reflection High Energy Electron Diffraction
RIE	Reactive Ion Etching
RT	Room Temperature ($\vartheta \approx$ 20-25 °C)
SEM	Scanning Electron Microscopy
TED	Transmission Electron Diffraction
TEM	Transmission Electron Microscopy
UHV	Ultra High Vacuum
VLS	Vapour-Liquid-Solid (Mechanism)
VSS	Vapour-Solid-Solid (Mechanism)

List of Chemical Symbols and Formula

a-Al_2O_3	Aluminium oxide, *sapphire*
Ag	*argentum* <lat.>: Silver
Al	Aluminium
Au	*aurum* <lat.>: Gold
B	Boron
Cu	*cuprum* <lat.>: Copper
Ga	Gallium
GaAs	Gallium arsenide
Ge	Germanium
GeH_4	Germane / Germanium tetrahydride
HF	Hydrogen fluoride
H_2O	Water (Dihydrogen monoxide)
H_2O_2	Dihydrogen peroxide
I_2	Iodide
InGaAs	Indium gallium arsenide
KI	(*kalium* <lat.>: Potassium) Potassium iodide
MgO	Magnesium oxide
Ni	Nickel
O_2	Oxygen
P	Phosphorus
Pd	Palladium
Pt	Platinum
Sb	*stibium* <lat.>: Antimony
SF_6	Sulfur hexafluoride
Si	*silicium* <lat.>: Silicon
$SiCl_4$	Silicon tetrachloride
SiH_4	Silane / Silicon tetrahydride
SiO	Silicon oxide
SiO_2	Silicon dioxide
Ti	Titanium
TiN	Titanium nitride

B List of Selected Experiments

Bottom-Up Approach

All NWs were grown on 5” (111)-oriented P doped Si wafers on a 200 nm thick Si buffer layer deposited at a substrate temperature $\vartheta = 550$ °C.

Experiment-#	Au Deposition	NW Growth	Growth Rate
Si NW growth			
070607	2.0 nm at $\vartheta = 525$ °C	270 nm Si at $\vartheta = 525$ °C	Si: 0.05 nm/s
Growth of Si NW with Ge layers			
070801	2.0 nm at $\vartheta = 525$ °C	230 nm Si at $\vartheta = 525$ °C 2.5 nm Ge at $\vartheta = 360$ °C 40 nm Si at $\vartheta = 525$ °C	Si: 0.05 nm/s Ge: 0.02 nm/s
070814a	2.0 nm at $\vartheta = 525$ °C	230 nm Si at $\vartheta = 525$ °C 2.5 nm Ge at $\vartheta = 525$ °C 40 nm Si at $\vartheta = 525$ °C	Si: 0.05 nm/s Ge: 0.02 nm/s
070921	2.0 nm at $\vartheta = 525$ °C	230 nm Si at $\vartheta = 525$ °C 2.5 nm Ge at $\vartheta = 525$ °C 40 nm Si at $\vartheta = 525$ °C	Si: 0.05 nm/s Ge: 0.02 nm/s
070928	2.0 nm at $\vartheta = 525$ °C	220 nm Si at $\vartheta = 525$ °C 2.5 nm Ge at $\vartheta = 360$ °C 30 nm Si at $\vartheta = 525$ °C 2.5 nm Ge at $\vartheta = 360$ °C 20 nm Si at $\vartheta = 525$ °C	Si: 0.05 nm/s Ge: 0.02 nm/s
071017b	2.0 nm at $\vartheta = 525$ °C	230 nm Si at $\vartheta = 525$ °C 5.0 nm Ge at $\vartheta = 360$ °C 40 nm Si at $\vartheta = 525$ °C	Si: 0.05 nm/s Ge: 0.02 nm/s
090102	1.5 nm at $\vartheta = 525$ °C	230 nm Si at $\vartheta = 525$ °C 2.5 nm Ge at $\vartheta = 525$ °C 40 nm Si at $\vartheta = 525$ °C	Si: 0.05 nm/s Ge: 0.01 nm/s
Continued growth of Ge on Si NW			
090105	1.5 nm at $\vartheta = 525$ °C	270 nm Si at $\vartheta = 525$ °C 20 nm Ge at $\vartheta = 325$ °C	Si: 0.05 nm/s Ge: 0.01 nm/s
090106a	1.5 nm at $\vartheta = 525$ °C	270 nm Si at $\vartheta = 525$ °C 20 nm Ge at $\vartheta = 300$ °C	Si: 0.05 nm/s Ge: 0.01 nm/s

Table 11: Bottom-Up Approach: List of Selected Experiments

Top-Down Approach

Molecular Beam Epitaxy

Experiment-#	Wafer	Buffer	Superlattice	Growth Rate
080819a	Si (111) P doped	200 nm Si at $\vartheta = 550$ °C	8 ML Si at $\vartheta = 525$ °C 2 ML Ge at $\vartheta = 525$ °C (40 periods) 20 nm Si at $\vartheta = 525$ °C	Si: 0.05 nm/s Ge: 0.02 nm/s
081020	Si (100) P doped	200 nm Si at $\vartheta = 650$ °C	10 ML Si at $\vartheta = 550$ °C 4 ML Ge at $\vartheta = 550$ °C (30 periods) 20 nm Si at $\vartheta = 550$ °C	Si: 0.05 nm/s Ge: 0.01 nm/s

Table 12: Top-Down Approach: MBE SL Parameters

Electron Beam Lithography and Reactive Ion Etching

Experiment-#	MBE-#	EBL			RIE			
					$\vartheta = -110$ °C / $p = 3.5$ mTorr $\approx 5 \cdot 10^{-3}$ mbar			
		Structure Size	**Distance**	**Dose**	**Plasma**	**RF**	**Bias**	**t**
L1300	080819a	40 x 40 nm^2	200 nm	1500 µC/cm^2	50 sccm SF_6 2 sccm O_2	40 W	92	80 s
L1302 (D)	081020	40 x 40 nm^2	500 nm	1650 µC/cm^2	50 sccm SF_6 2 sccm O_2	50 W	109	70 s
L1308	081020	40 x 40 nm^2	500 nm	1300 µC/cm^2	50 sccm SF_6 8 sccm O_2	40 W	107	70 s
L1323	081020	40 x 40 nm^2	500 nm	1300 µC/cm^2	50 sccm SF_6 12 sccm O_2	40 W	107	100 s
L1329	081020	40 x 40 nm^2	500 nm	1300 µC/cm^2	50 sccm SF_6 12 sccm O_2	40 W	107	70 s

Table 13: Top-Down Approach: EBL and RIE parameters

C Curriculum Vitae

Contact Information

Name:	Andreas Wolfsteller
Address:	Grassistr. 19 04107 Leipzig Germany

Education

Martin-Luther-University Halle-Wittenberg, Halle (Saale), Germany

04/2008 – 03/2010	Postgraduate student, *Physics*

Leibniz Institute of Surface Modification, Leipzig, Germany

02/2005 – 03/2006	Diploma student, *Physics*

University of Leipzig, Germany

10/2000 – 03/2006	Degree: Dipl.-Phys., *Physics*

Employment History

Max Planck Institute of Microstructure Physics, Halle (Saale), Germany

Experimental Department II – Prof. Ulrich Gösele

01/2009 – 06/2009	Postgraduate scholarship
07/2006 – 12/2008	Research scientist

Leibniz Institute of Surface Modification, Leipzig, Germany

Department for Ion Beam Technologies – Prof. Bernd Rauschenbach

02/2005 – 03/2006	Student assistant

Andreas Wolfsteller

D List of Publications

Publications in Refereed Journals

2010 A. Wolfsteller, N. Geyer, T.-K. Nguyen-Duc, P. Das Kanungo, N. D. Zakharov, M. Reiche, W. Erfurth, H. Blumtritt, S. Kalem, P. Werner, and U. Gösele
Comparison of the top-down and bottom-up approach to fabricate nanowire-based Si/Ge heterostructures
Thin Solid Films 518 (2010) 2555

2009 P. Das Kanungo, A. Wolfsteller, N. D. Zakharov, P. Werner, and U. Gösele
Enhanced electrical properties of nominally undoped Si/SiGe heterostructure nanowires grown by molecular beam epitaxy
Microelectronics Journal 40 (2009) 452

Contributions to Conferences

European Materials Research Society (E-MRS) Spring Meeting, Strasbourg, France

2009 A. Wolfsteller, N. Geyer, T.-K. Nguyen-Duc, N. D. Zakharov, M. Reiche, W. Erfurth, U. Doß, H. Blumtritt, P. Werner*, and U. Gösele *(Invited Talk)*
Comparison of the top-down and bottom-up approach to synthesise nanowire-based Si/Ge heterostructures

Materials Research Society (MRS) Spring Meeting, San Francisco, USA

2008 A. Wolfsteller*, P. Das Kanungo, T.-K. Nguyen-Duc, O. Breitenstein, N. D. Zakharov, V. V. Talalaev, P. Werner, and U. Gösele *(Poster)*
Growth and characterization of axial Si/SiGe nanowire heterostructures

DPG Spring Meeting, Solid States Physics Section, Germany

2009 A. Wolfsteller*, N. Geyer, T.-K. Nguyen-Duc, N. D. Zakharov, M. Reiche, W. Erfurth, U. Doß, H. Blumtritt, P. Werner, and U. Gösele *(Talk)*
Comparison of the top-down and bottom-up approach to synthesise nanowire-based Si/Ge heterostructures

2008 A. Wolfsteller*, P. Das Kanungo, T.-K. Nguyen-Duc, J. Bauer, O. Breitenstein, G. Gerth, N. D. Zakharov, P. Werner and U. Gösele *(Poster)*
MBE-growth and analysis of Si and Ge nanowires and corresponding heterostructures

Workshop on Recent Advances in Low-Dimensional Structures and Devices, Nottingham, UK

2008 P. Das Kanungo*, A. Wolfsteller, T.-K. Nguyen-Duc, O. Breitenstein, N. D. Zakharov, V. V. Talalaev, P. Werner, and U. Gösele *(Poster)*
Enhanced electrical conductivity of Si/SiGe axial heterostructure nanowires grown by molecular beam epitaxy

* Presenting author

E Acknowledgements

I would like to express my gratitude to these people:

- First of all I would like to thank Prof. Ulrich Gösele for the possibility to work at the Max Planck Institute of Microstructure Physics on this interesting topic, his critical comments, suggestions and fruitful discussions which often went on for several hours.
- These profitable discussions also happened between me and Peter Werner, my supervisor. His optimism and continuous support helped a lot during even the hardest times.
- Prof. Anna Fontcuberta i Morral for her willingness to act as the second referee for my thesis.
- My colleagues Trung-Kien Nguyen-Duc, Nadine Geyer, Pratyush Das Kanungo, Nikolai D. Zakharov, Vadim V. Talalaev, Aleksander Tonkikh, Gerhard Gerth, Andreas Frommfeld and Andreas Kipke who made my stay very enjoyable. Their cooperation was also a textbook example of good teamwork.
- Once again Nikolai D. Zakharov and Peter Werner for numerous TEM investigations.
- Once again Andreas Frommfeld and Gerhard Gerth for several miracles during repairs and the maintenance of the MBE machine.
- Manfred Reiche, Wilfried Erfurth, Horst Blumtritt, and Ursel Doß for their kind cooperation and technical support in almost everything related to the top-down approach. This includes EBL, RIE, and FIB preparation.
- Sigrid Hopfe and Claudia Münx for the preparation of many TEM samples.
- All colleagues at the Max Planck Institute of Microstructure Physics whom I forgot to mention above, but who nevertheless contributed to the success of my research.
- And last but not least I must thank my parents and my brother for their continuous support and encouragement during the past three years.

My research on the bottom-up approach was partly funded by the Deutsche Forschungsgemeinschaft (DFG) as part of the DFG Schwerpunktprogramm (SPP) 1165 “Nanodrähte und Nanoröhren: Von kontrollierter Synthese zur Funktion”.

<u>Nachtrag</u>

Nach dem völlig unerwarteten und viel zu frühen Ableben von Prof. Gösele danke ich an dieser Stelle recht herzlich PD Dr. Hartmut S. Leipner für die Übernahme der Betreuung in der Zeit zwischen Abgabe der Dissertation und der Verteidigung.

F Eidesstattliche Erklärung

Hiermit versichere ich, die vorliegende Arbeit selbständig und ohne Benutzung anderer als der im beigefügten Literaturverzeichnis angegebenen Hilfsmittel angefertigt zu haben. Alle Stellen, die wörtlich oder sinngemäß aus Veröffentlichungen entnommen wurden, sind als solche kenntlich gemacht.

Die Arbeit wurde bisher in gleicher oder ähnlicher Form keiner anderen Prüfungsbehörde vorgelegt und auch nicht veröffentlicht.

Halle (Saale), 22. Oktober 2009

Andreas Wolfsteller

Erklärung

Ich versichere hiermit, dass ich mich an keiner wissenschaftlichen Hochschule im Geltungsbereich des deutschen Grundgesetzes bereits früher um den Doktorgrad beworben habe.

Halle (Saale), 22. Oktober 2009

Andreas Wolfsteller